THESIS

TRANSIENT EXPERIMENTATION AND MODELING OF A MULTI- MICROCHANNEL
EVAPORATOR

Submitted by

Joshua Johnhenry Richey

Department of Mechanical Engineering

In partial fulfillment of the requirements

For the Degree of Master of Science

Colorado State University

Fort Collins, Colorado

Spring 2020

Master's Committee:

    Advisor: Todd Bandhauer

    Steve Simske
    Peter Young

ABSTRACT

TRANSIENT EXPERIMENTATION AND MODELING OF A MULTI-MICROCHANNEL
EVAPORATOR

Laser diodes are semiconductor devices that convert electrical energy into light. Often, diodes are arrayed closely together to produce high optical output. Commercially available diode arrays show electro-optical efficiencies of ~50%, resulting in high heat fluxes from these compact devices. Active thermal management is warranted to prevent decreases in performance or damage to the device. Two-phase cooling in microchannels has shown great promise in steady-state studies, dissipating heat fluxes over 1.1 kW cm^{-2}. The very high latent heat and buoyancy-driven effects associated with two-phase cooling produce large heat transfer coefficients, minimizing undesirable temperature gradients across the diode. Previous research has primarily focused on steady-state operation. Although promising steady-state results were documented, little is known on the effects of transient heat loads on microchannel flow boiling. Laser diodes can rapidly change their optical output, inducing extreme transient heat loads. Furthermore, cold start up, where the diode is stepped up directly to maximum optical output, produce transient heat loads which are especially concerning. These transient challenges need to be fully understood to usefully implement two-phase cooling of laser diode arrays.

The current study investigates the effects of transient heat loads on a multi-microchannel evaporator. A silicon multi-microchannel heat exchanger with small hydraulic diameters (52 µm) and a surrogate laser diode heater, developed by Lawrence Livermore National Laboratory, is integrated into a two-phase pumped loop to perform transient experiments with pulsed and ramped

heat loads. When exposed to pulsed loads, infrared temperature measurements and flow visualization showed extreme superheat temperatures (~50°C) before the onset of boiling. After the onset of boiling, unexpected flow instabilities were seen, followed by a delay in steady-state two-phase boiling that could not be explained by thermal mass of the test section. Transients in the flow conditions were also documented, and ramping heat loads showed promise in mitigating the peak temperature and flow instabilities.

Furthermore, a transient thermal suite (ATTMO) developed by P C Krause and Associates (PCKA), is utilized to model the microchannel evaporator. The thermal suite is augmented to model the dynamics seen under a pulsed heat load. A reduced-order, non-computationally demanding method using a logistic function to describe the transient heat transfer coefficient is implemented into ATTMO. The transient modeling results showed a good correlation (average error of (±2.04°C) with the experimental data collected. A direct relationship between onset of boiling temperature and growth rate is shown. The results from this study show potentially dangerous peak temperatures for laser diodes. Mitigation strategies should be investigated and implemented to avoid the extreme superheat temperatures. The non-computationally demanding model developed in this research can be used in future studies to rapidly investigate the effects of heat loads and different operational parameters.

Gilvey; for your positive attitude and sense of humor; Sam Colosimo, for always down to have a great time and taking big pow shots.

Thank you to my family: Mom, Dad, Ashley, and Sam. Your love and support have made me into the person I am today. And most importantly, thank you, Jamie, for supporting me in all aspects of life, and for thinking it was a good idea to leave a job and move across the country with me, love you.

TABLE OF CONTENTS

LIST OF TABLES

LIST OF FIGURES

NOMENCLATURE

Symbol	Description	Units
A	Area	m^2
ATTMO	AFRL transient thermal management optimization	-
Bo	Boiling number	-
beta	Aspect ratio	-
CHF	Critical heat flux	W m^{-2}
Co	Confinement number	-
D_h	Hydraulic diameter	m
d	Diameter	m
DRIE	Deep reactive ion etching	-
F_g	Gravitational force	N
F_I	Inertia force	N
F_m	Momentum force	N
F_S	Surface tension force	N
Fo	Fourier number	-
f	Friction factor	-
G	Mass flux	kg m^{-2}
g	Gravity	m s^{-2}
GUI	Graphic user interface	-
h_{fg}	Enthalpy of vaporization	kJ kg^{-1}
h	Enthalpy	kJ kg^{-1}
ht	Heat transfer coefficient	kW m^{-2} K^{-1}
IR	Infrared	-
k	Conductivity	kW m^{-1} K^{-1}
L	Length	M

M	Molecular weight	kg kmol^{-1}
$\dot{m}$	Mass flow rate	kg s^{-1}
Nu	Nusselt number	-
ONB	Onset of nucleate boiling	-
P	Pressure	kPa
Pr	Prandtl number	-
q	Heat load	kW
Q	Heat load	kW
Re	Reynolds number	-
R$_P$	Surface roughness parameter	-
t	Time	S
T	Temperature	°C
U	Overall heat transfer coefficient	kW m^{-2} K^{-1}
v	Velocity	m s^{-1}
V	Volume	m^3
x	Fluid vapor quality	-
Greek Symbols		
ρ	Density	kg m^{-3}
σ_t	Surface tension	N m^{-2}
σ	Stefan-Boltzmann constant	W m^{-2}K^{-4}
μ	Dynamic viscosity	kg m^{-1}s^{-1}
β	Aspect ratio	-
α	Thermal diffusivity	m^{2}s^{-1}
Subscripts		
c	Characteristic	-
Conv	Convection	
f	Fin	-
fl	Fluid	-
fric	Friction	-

l	Liquid	-
g	Gas	-
Laminar	Laminar	-
major	Major losses	-
min	Minor losses	-
NB	Nucleate boiling	-
n	Node number	-
s	Surface	-
tp	Two-phase	-
trans	Transitional	-
turb	Turbulent	-
v	vapor	-
w	Wall	-

CHAPTER 1 INTRODUCTION

1.1 Background

Laser diodes are semiconductors lasers which generate light (photons) using electrical energy (electrons). The wavelength produced from these devices can be tuned from infra-red to the UV spectrum, making laser diodes useful in a wide range of applications. Some examples of applications where laser diodes have been implemented are fiber optic communications, barcode readers, laser printing, laser scanning, the medical field, direct energy weapons, and laser pumping [1]. In applications such as laser pumping, a narrow emission spectrum is desired. Laser pumping uses a lasing gain media to amplify a solid-state laser beam by absorbing light from an external source such as a laser diode or flashlamp [2]. Therefore, to increase efficiencies a narrow bandwidth is wanted from the pumping source to closely match the absorption lines of the media. Laser diodes have a very narrow emission bandwidth which make them highly sought after.

Because some applications require a narrow emission spectrum, the physics of light emission should be discussed. For light to be generated a semiconductor material is doped to form two types of materials, a p-type (rich in positive charge carriers called 'holes,' lacking electrons) and an n-type (excess electrons). These two materials are joined to form a p-n junction, such as that seen in Figure 1-1 [3]. When a forward bias is applied, electrons flow across the junction and combine with the holes, releasing a photon and dropping in energy level. The released photons interact with other excited electrons and cause the electrons to decay to a lower energy level, fostering more photons at the same wavelength and phase; this process is known as stimulated emission. Stimulated emission is amplified with optical resonators in the p-n junction. The photons are continuously reflected and interact with electrons creating more photons. Once the photon flux

1

reaches the threshold amplification photons emanate from the p-n junction in the form of a coherent beam [4].
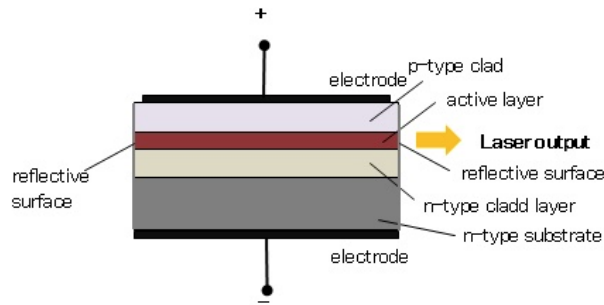
Figure 1-1. Schematic of a semiconductor laser diode [3]

Figure 1-1 shows a single emitter laser diode. The output power of a single emitter is less than 15 W [4]. To increase optical output power, or brightness, single emitters are placed in laser bars, and bars are further placed into arrays (Figure 1-2).
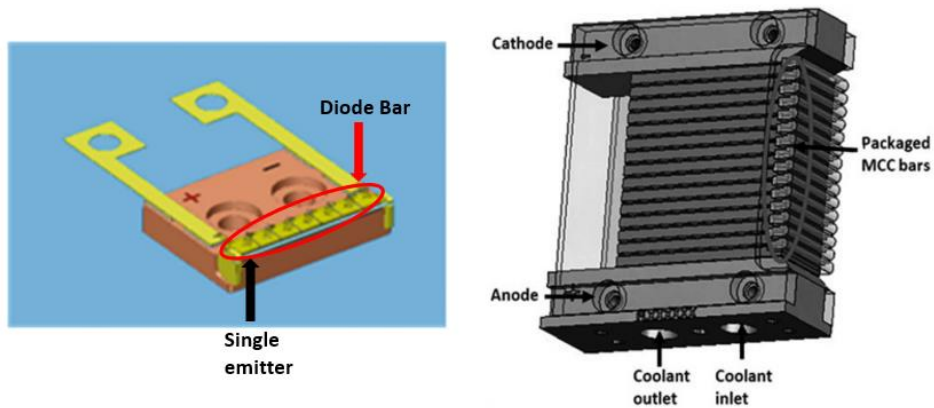
Figure 1-2. Diode bar (left) and diode bar array (right) [5]

To achieve higher brightness, the pitch between diode bars is decreased. Diode bar pitch for high powered laser diodes can reach dimensions less than 2 mm [5]. In addition to high power outputs, diodes have high conversion efficiencies, commercially available products are 50%, while

laboratory studies have reached as high as 75-80% [6]. Although high optical output power and efficiencies can be reached, thermal management is the limiting factor to diode performance. Elevated diode temperatures can cause undesirable wavelength drifts, decreases in light intensity, and decreases in efficiency [4].

The thermal challenges associated with diodes warrant different cooling strategies. Single emitter diodes often employ simple conduction strategies, where the diode is mounted on a substrate with a high thermal conductivity. The high conductivity allows heat to easily dissipate from the diode and spread throughout the substrate. However, when diodes are placed in arrays, the heat cannot be dissipated via conductive cooling, and an active cooling system is necessary. Single-phase cooling has been the traditional approach for these high power loads. In single-phase cooling, a fluid flows through a heat exchanger on the substrate beneath the diode and absorbs the heat from the diode. As heat loads increase, the temperature of the working fluid increases as it moves across the diode array. This can lead to temperature gradients across the array, causing diodes to emit at different wavelengths. To circumvent this, the flow rate is increased at the cost of high pressure drop, more pumping power, and a larger fluid inventory. Although single-phase cooling provides an easy thermal management solution, as diode pitch is decreased further at increased power output, the practical limits for single-phase cooling are being reached.

One promising method addressing the high heat demand of laser diodes is implementing two-phase cooling. The latent heat and buoyancy-driven flow effects of flow boiling allow for large heat transfer rates compared to single phase cooling [7]. The high heat transfer rates associated with flow boiling allow for lower mass flow rates, resulting in less pressure drop for the same heat removal. Furthermore, latent heat cooling exploits the near isothermal fluidic phase change, minimizing temperature gradients across the diode. Although two-phase cooling can

3

dissipate large heat loads at relatively low flow rates and pumping power, size constraints due to decreasing pitch remain challenging. Supporting efforts to decrease diode pitch, researchers have investigated using microchannel heat exchangers in conjunction with flow boiling. By decreasing the hydraulic diameter of the channels, heat transfer performance can be increased due to low thermal resistance, improved surface-area-to-volume ratio , and minimal coolant use [8]. Research has shown steady state heat load dissipation greater than 1.1 kW cm^{-2} [9].

When considering the implementation of microchannel flow boiling in real-world applications, it is important to consider the different operational modes. Laser diodes primarily operate in two modes, a continuous wave operation (continuous operation) or with short current pulses (pulsed operation). In continuous operation, the laser emits light with no interruption, while in pulsed operation, the power source is switched on/off at specified time intervals [10]. Applications that use continuous operation need a constant output power over a duration of time. For example, metal work like laser cutting or welding requires long and powerful outputs due to the reflective nature of metal [11]. Where these long continuous outputs are not needed a pulse operation can be implemented. In some medical procedures, like laser acupuncture or therapy, a short powerful pulse is required to penetrate the skin without damaging the cells [12]. Nonetheless, both modes of operation are widely used and need to be taken into consideration. The majority of diode cooling research has been conducted using steady-state assumptions in which the heat loads are slowly increased and data is recorded when the system load has stabilized. In practical applications, heat load demand may be extremely dynamic. If the laser is operating in pulse mode, the heat load will rise and fall dramatically. Moreover, in continuous mode, the laser will have some transients during cold startup or during load shifts. Very few experiments have been conducted considering dynamic heat loads for flow boiling in microchannels. In addition to the

4

lack of experimental data, to the author's knowledge, no current modeling method exists for the dynamic temperature change seen in the literature. The current work investigates the effects of dynamic heat loads on a microchannel evaporator. Experimental data is used to develop a new modeling scheme for the dynamic temperature change.

1.2   Research Objectives

Currently, a limited inventory of experimental data exists for transient heat loads on a microchannel evaporator. Without adequate data, it is unclear if two-phase cooling strategies in microchannels will cause device failure or damage. In applications with high frequency and power pulses, extreme transient heat loads need to be rejected. Applications that require a continuous output will inevitably have a cold start up and a startup transient heat load will occur.   Therefore, experiments are needed to investigate the effects of dynamic heat loads on flow boiling. Additionally, no modeling method exists for transient temperature change during the onset of nucleate boiling. Modeling efforts and a comprehensive data set are necessary to guide the development and implementation of flow boiling in microchannels for laser diode applications.

The current work uses a multi-microchannel evaporator connected to a two-phase pump loop to collect data using transient heat loads. Two types of heat loads are investigated: pulsed and ramped. Pulsed heat loads resemble the cold start up to maximum power seen in pulsing a laser. The effects of a ramped heat load are important to study to investigate any positive or negative impacts, or potential mitigation strategies. If the effects of a ramped heat load mitigate any transients compared to a pulsed heat load, the ramped heat load could be implemented in continuous operation when a sharp increase in light is not necessary. In addition to collecting experimental data, this work proposes a transient thermal modeling method for microchannel evaporators under pulsed heat loads. In collaboration with PC Krause and Associates (PCKA), a

transient thermal model is used and augmented. Modeling efforts will help to guide future development to rapidly investigate operational parameters and heat sink geometries for laser diodes.

1.3   Thesis Organization

This document includes five additional chapters: Chapter 1 Literature Review, Chapter 2 Experimental Setup, Chapter 3 Data Reduction, Chapter 4 Results and Discussion, Chapter 5 Conclusions and Recommendations and an Appendix. Literature Review includes a detailed review of previous work on steady-state flow boiling studies, transient flow boiling studies, flow boiling instabilities, and onset of nucleate boiling. In Experimental Setup, a detailed overview of the microchannel evaporator, test facility, and test matrix is provided. Data Reduction describes the transient model and assumptions used in this study. Results and Discussion examines the results of the experiments and proposes a novel modeling method. Conclusions and Recommendations elaborates on the experimental and modeling efforts and provides future recommendations. Finally, the Appendix provides details on the facility used, calibration of the infrared camera, and hand calculations performed.

CHAPTER 2 LITERATURE REVIEW

To increase brightness of laser diodes, pitch has been decreased and power loads increased. Increasing heat fluxes, in some cases exceeding 1 kW cm^{-2} [9], and decreased package sizes have led researchers to explore novel cooling approaches to increase diode optical power. Significant efforts have been made investigating single-phase cooling [13]. However, with single-phase cooling, the temperature of the fluid increases across the diode causing undesirable temperature gradients. In addition, to increase the heat transfer, high flow rates are required with single-phase cooling, which limits the coolant to flow to the back of the diode array, due to high pressure drop if the coolant flows in-between individual diode bars. Two-phase flow boiling provides a solution because of the large heat transfer rates as compared to single-phase cooling. Two-phase microchannel cooling is the most promising because the cooling fluid is located close to the diode surface, limiting the thermal resistance between the diode and coolant. In addition, decreasing the hydraulic diameter increases heat transfer area while minimizing total package volume. Smaller cooling packages are an extremely attractive feature because the pitch between diode bars decreases. Furthermore, the small flow rates associated with two-phase boiling in microchannels decrease pressure drop, pumping power, and overall fluid inventory.

This chapter will describe literature which has been conducted to understand physical phenomena that occur during flow boiling in microchannel heat exchangers. Additionally, this chapter will discuss relevant research on dynamic flow boiling in microchannels. By presenting the current research, this chapter aims to understand current research gaps. Finally, the specific aims which seek to fill those gaps will be presented.

2.1 Physical Phenomena of Flow Boiling in Microchannels

The definition of microchannels has been debated by engineers and scientists, but no clear consensus has been reached. Some researchers define the change to microscale purely based on the hydraulic diameter. Mehendale et al. suggested microscale is for hydraulic diameters from 1 – 100 µm, mesoscale 100 µm – 1 mm, compact scale 1 – 6 mm, and conventional greater than 6 mm [14]. Kandlikar recommended microscale 50 – 600 µm, mini channels 600 µm – 3 mm and conventional greater than 3 mm [15]. Although this is a straightforward way to classify channel sizes, it leaves out factors that change the fluid dynamics within the channels. For example, flow patterns in microchannels are dominated by the surface tension of the working fluid [16]. Therefore, researchers have developed methods that include fluid and flow characteristics to define a microchannel. Harirchian et al. developed a comprehensive flow regime map to define the transition to microchannel quantitatively [11]. The criterion they developed incorporates the effects of mass flux, channel cross-sectional area, and fluid properties. They deemed the criterion the convection confinement number, which is the square root of the Bond number (Bo) multiplied by the liquid Reynolds number (Re). The Bond number is the ratio of gravitational forces to surface tension forces and the Reynolds number is the inertial forces to the viscous forces. The authors used the flow regimes in the channels to determine if the flow was confined. The authors noted that confined flow is the transition when bubbly flow is non-existent in the channels. They concluded microchannels exist at convective confinement numbers less than 160. Li and Wu used a non-dimensional number ($Bo*Re^{0.5}$) to characterize the transition to the micro-scale region [17]. They considered the change to microchannels when the relationship between the non-dimensional number and Nusselt number did not have strong relationship with each other, the authors determined this when the data was more dispersed. The authors quantitatively described

8

microchannels at non-dimensional numbers less than 200. Cornwell and Kew presented the transition using the confinement number [18], equation (2.1):

$$Co = \frac{\left[\dfrac{\sigma_t}{\left(g\left(\rho_l - \rho_g\right)\right)}\right]^{\frac{1}{2}}}{d} \qquad (2.1)$$

The confinement number (Co) is the ratio of surface tension to buoyancy forces, which tells us how confined a bubble is in the channel as it grows. They designated the transition to microchannel region being confinement numbers greater than 0.5. Although not all researchers agree on a defined transition from micro to macro scale, there are differences in physical phenomena that occur between the scales. Therefore, the sections in this chapter mainly focus on research that has been conducted at the microscale. The following sections focus on four major areas of flow boiling in microchannels: flow boiling regimes, the onset of nucleate boiling, flow boiling instabilities, and heat transfer mechanisms.

2.1.1   Microchannel Flow Boiling Regimes

Flow boiling in microchannels has different flow boiling characteristics as compared to typical macrochannel flow boiling because surface tension effects dominate over gravitational effects [19]. Figure 2-1 [20] shows several flow regimes typically seen in macrochannel horizontal boiling flow. Most of the regimes, including bubbly, plug, stratified, and slug flow all show the effects of gravity pulling the less buoyant liquid to the bottom of the tube. Only in annular flow (very high mass flows) do the effects of gravity decrease enough to have a more even distribution. As the hydraulic diameter decreases, however, the effects of gravity become negligible even at low flow rates. This phenomenon is explained by examining the forces, Equations (2.2) – (2.5),

exerted on a vapor bubble: momentum force, inertial forces, surface tension forces, and gravitational forces, respectively [21].
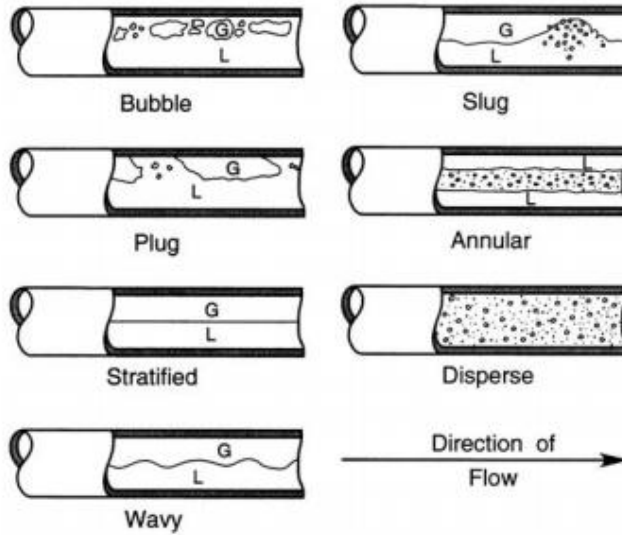
Figure 2-1. Flow regimes – horizontal flow [20]

Equation (2.5) shows the characteristic diameter squared; thus diminishing the gravitational effects at small hydraulic diameters.

$$F_m = \left(\frac{q}{h_{fg}} \right)^2 \frac{D_h}{\rho G} \qquad (2.2)$$

$$F_I = \frac{G^2 D_h}{\rho_L} \qquad (2.3)$$

$$F_S = \sigma \cos \theta \qquad (2.4)$$

$$F_g = \left(\rho_l - \rho_g \right) g D_h^2 \qquad (2.5)$$

Cornwell and Kew visualized the microchannel boiling regimes experimentally through flow visualization and heat transfer measurement [22]. They classified three types of flow boiling

10

regimes for microchannels: isolated bubble (bubbly flow), confined bubble and annular/slug flow. Mirmanto et al. performed experiments on a single microchannel and found four different boiling regimes: bubbly, slug/confined, churn and annular [23]. Churn flow is the disruption of slug flow, meaning bubbles become unstable at the tail ends of the slug. Thome and Revellin developed a diabatic flow pattern map [24]. Their map classified the flow into three flow regimes: isolated bubble (bubbly and slug), coalescing (bubble coalescence rate is larger than bubble generation), and annular regime. The map they created could be used to determine operating ranges in microchannels.

2.1.2 The Onset of Nucleate Boiling

One important aspect of boiling is the onset of nucleate boiling (ONB). This marks the transition from single-phase forced convection to combined nucleate and convection boiling. The onset marks a time where heat transfer mechanisms are changing; thus, it is of the utmost importance to understand the phenomenon during dynamic load transitions. Figure 2-2 depicts the ONB curve with heat flux on the y-axis and wall superheat on the x-axis [20]. During the period
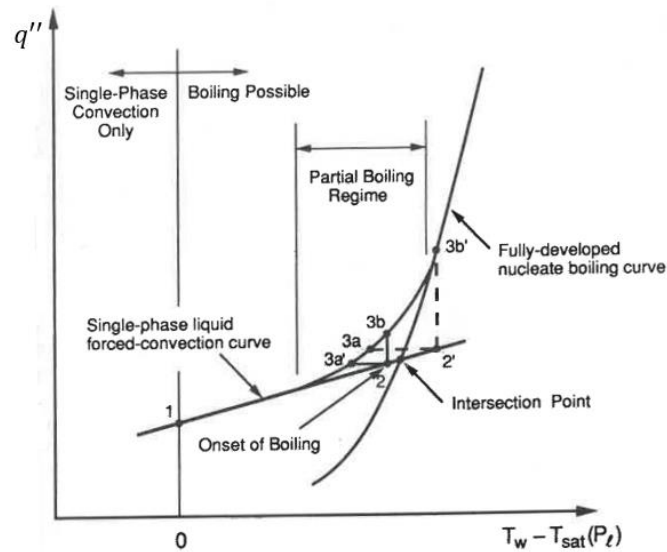
Figure 2-2 Onset of boiling curve [21]

11

of single-phase forced convection, boiling is possible, but it often does not occur until a certain amount of wall superheat is reached. The amount of superheat changes depending on fluid properties, wall cavity size distribution, and imposed flow conditions [20]. For constant heat flux conditions, if boiling commences a drop in test section temperature occurs (point 2 to 3a´). For isothermal conditions boiling coincides with an increase in heat flux (point 2 to 3b). However, the location where this occurs is unknown. Researchers have focused on determining the onset point and different correlations have been developed. One important factor when determining the ONB is the presence of wall imperfections (also called cavities) where bubble nucleation occurs [25]. Hsu analyzed the relationship between cavity size and surface temperature, the causes of boiling incipience, and the maximum and minimum sizes of an active nucleation site [26]. Hsu's model shows the onset of nucleate boiling is dependent on thermophysical properties, boundary layer thickness, degree of subcooling, and wall superheat. Because Hsu's equations can predict the onset of boiling using the four properties mentioned above, and assuming boundary layer thickness temperature change is linear, the heat flux at the wall can be calculated using Fourier's Law. His work allowed future researchers to use fluid properties, wall superheat, and heat flux to predict the onset of nucleate boiling.

Following Hsu's work, researchers began developing different correlations to predict the onset of nucleate boiling, focusing on heat flux and wall superheat requirements. Bergles et al. developed a method to predicted the onset using a graphical technique solving for the governing equations [27]. Bergles stated the inception of boiling was successfully predicted at high system pressures when comparing to experimental results. The author recommends the model only be used for commercially finished surfaces, due to the wide range of active cavity sizes expected with these surfaces. Sato and Matsumura took an analytical approach to predict the ONB [28]. Their

relationship was compared with the experimental data they collected and from previous researchers. The data gathered by the authors at atmospheric pressure showed an excellent relationship with their model. Comparing to higher pressure data from previous researches (7 atm, 35 atm, and 140 atm) the model coincided with the data agreeably. However, when subcooling was large, there was a deviation from the analytical and experimental results. The authors attributed the deviation to unreliable observations, the assumption of the temperature profile and the shape of the critical bubble. Davis and Anderson developed a model as an extension of Bergles and Rohsenow's work [27,29]. Their model was validated using Bergles's and Rohsenow's model predictions and experimental data, data from Sato and Matsumura's, Mantzouranis, and Backhurst's studies [28,29]. Their model predicted the ONB well comparing to data from Bergles and Rohsenow, and Mantzouranis and Backhurst. However, using the data from Sato and Matsumura, the equations under predicted the incipient boiling. The author notes that this could be an error in how Sato and Matsumura measured the ONB. Bergles and Rohsenow concluded their model appears to be satisfactory for determining an upper limit to the wall superheat required to initiate nucleate boiling. However, all the models mentioned here were not developed using microchannels and did not investigate rapidly applied heat loads.

From the studies above investigating the ONB criteria, all correlations require a certain amount of wall superheat to initiate boiling. Additionally, all the correlations showed an increasing heat flux increased the wall superheat temperature required to initiate boiling. As heat fluxes are continuously rising, this can lead to dangerous operating temperatures preceding the ONB. Therefore, some researchers explored mitigating the required wall superheat needed to initiate boiling. Deng et al. reduced the required wall superheat using porous reentrant microchannels to 0.5-2.1°C, which was significantly lower than other copper and silicon microchannels (5-20°C)

[30]. The porous channels provided many active nucleation sites, which lowers the energy needed for ONB. Kuo and Peles demonstrated the use of structured reentrant cavities in microchannels to reduce the required wall superheat roughly 15°C lower than the plain wall test sections [31]. The authors noted the decrease in wall superheat was due to more active cavity sizes. The microfabrication technique used for plain walls severely restricts the range of active cavity sizes. Therefore, the authors used a technique that increases active cavities which lowers the energy requirement for ONB. Ammerman and You used a microporous surface coating in small channels to enhance boiling nucleation [32]. Ammerman and You were able to reduce the wall superheat at ONB by 75%. They theorized the mechanism for the reduction is due to an increase in nucleation sites, due to the coating. Wang and Peterson using a brazed wire mesh in parallel microchannels and stated they were able to significantly reduce wall superheat at ONB [33]. They also stated the decrease in temperature was brought on by the increase in nucleation sites. Although these researchers provided ways to decrease wall superheat, none of these studies used a rapidly applied heat load. It is unknown if these techniques can be used to mitigate transient wall superheat. Basu et al. and Huang et al. both showed extreme transient wall superheats before the inception of boiling but did not provide any mitigation techniques [34,35]. These high temperatures can be detrimental to cooling equipment, and more thorough research needs to be completed to understand this phenomenon.

2.1.3   *Flow Boiling Instabilities*

Two-phase flow systems are inherently subjected to small scale fluctuations in flow due to turbulence or nucleation. If a fluctuation occurs and the system returns to its steady-state operation point the system is considered stable [20]. However, if the system experiences unsteady changes such as temperature or flow excursions, the system may be experiencing a flow instability. Flow

boiling instabilities are undesirable in two-phase systems because they affect heat transfer and fluid flow characteristics that could potentially lead to failure or damage to the cooling device. Knowledge of two-phase instabilities is critical for designers and operators to ensure components are not damaged during operation. Moreover, boiling instabilities are exacerbated in microchannel boiling due to confined bubble growth [36]. As a confined bubble grows in a microchannel, the bubble can grow larger than the height or width of the channel, which causes the bubble to elongate up and downstream. As the bubble grows parallel to the channel flow, this induces flow instabilities. Different types of instabilities can arise in a two-phase system, but they are generally categorized as static or dynamic [20].

An instability is static if the source of the instability is intrinsic to the steady-state operating characteristics of the system [20]. The two most common static instabilities encountered are the Ledinegg and the critical heat flux transition instability. The Ledinegg instability occurs due to non-monotonic channel characteristics. Figure 2-3 shows a non-monotonic system pressure drop
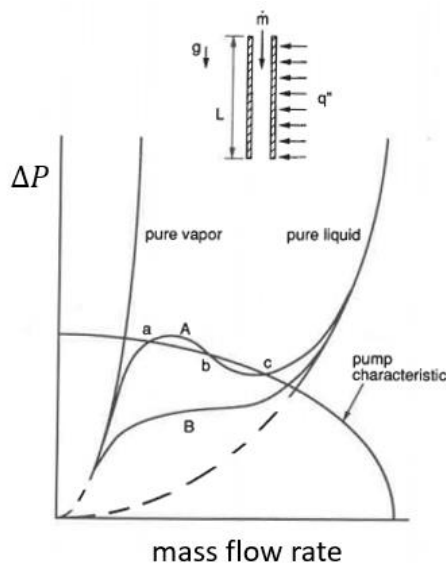
Figure 2-3. Representative pump curve and two-phase system curve [20]

15

curve in which a system can follow along curve A or curve B [20]. If the curve has a negative region (curve A) it can intersect at three different points of the pump curve. At point b of curve A, the flow curve is more negative than the pump curve and the operating point is considered unstable. For example, if the operating point is point b, and the mass flow is increased, the system ΔP is will decrease until reaching the pump curve at point c. Conversely, at operating point b, if the mass flow increases, the system ΔP will increase until the system operating point intersects at point a. Zhang et al. investigated the Ledinegg instability in microchannels, experimentally and numerically [37]. The study found that higher system pressures, reducing the number of parallel channels and channel length, larger channel diameters, and implementing an inlet restriction can mitigate the Ledinegg instability. Boure et al. suggested two remedies to combat the Ledinegg instability: inlet restriction, and an increase in steepness of the pump head versus flow curve [38]. The Ledinegg instability has been studied in-depth during steady-state operation and certain precautionary measures can be taken to ensure safe operation. However, these studies have not investigated dynamic heat loads and it is unclear if these measures can be extended and used.

Critical heat flux (CHF) describes the heat flux when the heat transfer coefficient decreases significantly provoking a rise in wall superheat. The decrease in the heat transfer coefficient is precipitated by the change from nucleate boiling to film boiling. Nucleate boiling can be described as the growth and departure of vapor bubbles from the surface, followed by cooler bulk fluid replenishing the surface. Generally, nucleate boiling is associated with very high heat transfer rates. In film boiling, a vapor blanket coats the wall and the thermal conductivity decreases which causes a sharp reduction in the heat transfer coefficient. The heat transfer coefficient is a measure of heat transfer between a fluid and surface. When the heat transfer is high, heat can easily be removed from the surface, lowering the temperature. Conversely, if the heat transfer coefficient is

low, heat is not easily removed, resulting in a higher wall temperature. The increased wall temperature can potentially damage the cooling device; thus, a strong understanding of the mechanisms behind the CHF is of paramount importance. Qu et al. performed experiments in a microchannel heat sink to characterize the CHF [39]. Their study found the CHF is independent of fluid inlet temperature, but the CHF increases with increasing mass velocity. Additionally, as the heat flux approached the CHF, vapor flowed back into the inlet plenum. The vapor mixes with the inlet liquid, diminishing the effects of subcooling, increasing the exit quality, and inducing a lower CHF threshold. Bergles and Kandlikar performed experiments in microchannels to deduce the source of the CHF [40]. They determined conjugated heat transfer effects could potentially be important where the CHF would occur near the heater. Additionally, the conditions where the CHF would arise were due to upstream compressible volume instabilities or the Ledinegg instability. Furthermore, the authors suggested an inlet restriction to avoid the CHF. Thome and Revellin proposed a model to predict CHF [41]. The theoretical model is based on the two-phase conservation equations and compared to a CHF database, including three different refrigerants and various geometries from two different laboratories. 96% of the data were predicted within a ±20% error band. Overall, CHF is associated with a dramatic decrease in the heat transfer coefficient, causing a rapid increase in the temperature of the test section. The temperature effects can damage the device; therefore, CHF must be taken into consideration during testing.

Dynamic instabilities occur when thermal or hydrodynamic inertia effects cause the instability [20]. Dynamic flow instabilities include density wave oscillations, acoustic oscillations, thermal oscillations, coupling instabilities, and pressure drop instabilities [42]. Oscillations in a system are undesirable, because they can cause mechanical vibrations, problems with controls, and disruptions in heat transfer characteristics which can initiate CHF [43]. Understanding the factors

which can cause dynamic flow instabilities is critical to avoid operational disruptions. Brutin et al. investigated dynamic instabilities with optical measurement in microchannels [44]. The study found that a stable region and unstable region corresponded with heat flux and mass flow rate. Figure 2-4 shows the stability diagram generated from the study. In the unstable region, a
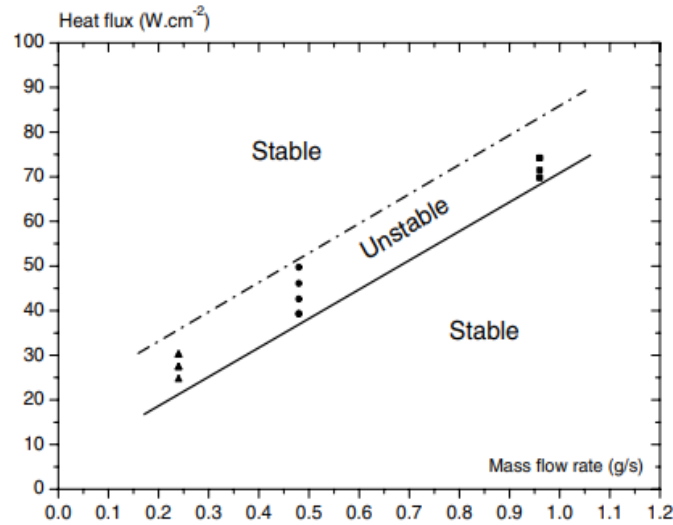
Figure 2-4. Stability diagram (channel: $0.5 \times 4 \times 50$ mm^3) [44]

fluctuation in the inlet and outlet pressures at a given frequency engenders vapor backflow into the inlet plenum. Xu et al. measured the onset of dynamic flow instabilities using a parallel microchannel heat sink [45]. The researchers demonstrated by lowering the mass flow rate at a given heat flux, they could induce oscillations. They observed three types of oscillations: large-amplitude, small amplitude, and thermal. Large amplitude oscillations occurred at lower inlet liquid temperatures, small amplitude at higher inlet temperatures, and thermal oscillations occurred in each case. Wang et al. experimented with both parallel microchannels and a single microchannel [46]. They found unstable flow boiling existed for 0.96 kJ kg^{-1} < q/G < 2.14 kJ kg^{-1} in parallel channels and 0.09 kJ kg^{-1} < q/G < 0.32 kJ kg^{-1} for a single channel. The instability was inspected visually and was associated with backflow of bubbles into the inlet plenum. Additionally, the

temperature of the test section would oscillate during times of unstable flow, in both the single and parallel channel heat sink.

Flow oscillations can be potentially dangerous for the device and researchers have developed ways to mitigate or eliminate instabilities all together. Kosar et al. investigated mitigating flow oscillations in parallel microchannels using inlet restrictions [47]. The inlet restrictor successfully suppressed oscillations and increased the heat flux at which unsteady boiling emerged (~35 to 340 W cm^{-2}). They characterized the inlet restrictor with a dimensionless parameter, M. The researchers found heat fluxes corresponding to the onset of unstable flow increase asymptotically with M. Wang et al. also investigated applying inlet restrictions to suppress oscillations. They used three different configurations, inlet and outlet restrictions (type A), no restrictions (type B), and inlet restriction only (type C) [48], and showed successful damping in all cases. Also playing an important role in suppressing instabilities are fluid conditions and channel geometry. Kuo and Peles examined fluid pressure effects on oscillations in parallel microchannels [49]. They found higher system pressure can significantly delay instabilities. Kuo and Peles performed an experimental study to suppress flow oscillations using reentrant cavities [50]. They investigated three types of microchannels devices: with reentrant cavities, with interconnected reentrant cavities, and plain wall microchannel. They found reentrant cavities can assist in mitigating flow boiling instabilities. The reentrant cavities delayed and moderated flow oscillations and increased the CHF.

Flow boiling instabilities can cause detrimental effects on a device. In addition, flow boiling instabilities are exacerbated in microchannels due to confined growth. Although significant research has been completed toward instability mitigation, these studies did not investigate the

effects of dynamic heat loads. It is unknown if the techniques here apply during a rapid heat load change.

2.1.4 Heat Transfer

One critical parameter in determining two-phase microchannel boiling performance is the heat transfer coefficient. Two types of heat transfer are associated with flow boiling: nucleate and convective boiling [51]. Nucleate boiling is when heat transferred into the fluid causes vapor bubbles to form. The bubbles depart from the surface, cooler bulk fluid replaces it, and the process is repeated. Convective boiling is defined as heat transfer due to bulk fluid motion through the channel. Figure 2-5 shows the heat transfer mode as a function of the flow regime in microchannels [51]. Nucleate boiling dominates heat transfer in microchannels, and convective effects contribute
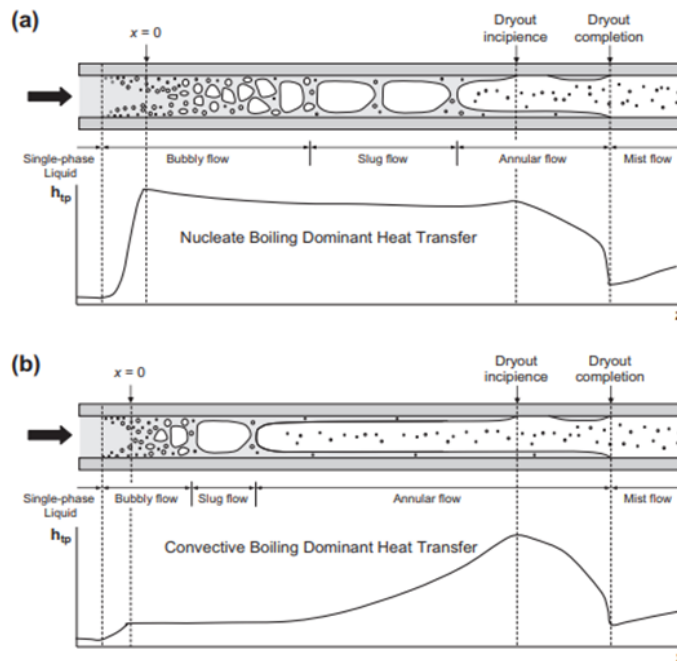
Figure 2-5. Dominate heat transfer for flow boiling in microchannels [51]

to a very small portion of the overall heat transfer at low vapor qualities (bubble and slug flow). Convective effects increase with increasing quality; however, the effects of convective heat transfer do not play a significant role until dryout incipience. Following dryout both nucleate and

convective heat transfer drop significantly. Although nucleate boiling is dominant, researchers have described the heat transfer coefficient as a function of both nucleate and convective boiling [52–54]. Some correlations ignored the convective heat transfer term and only focused on the nucleate boiling term [55–57]. These models all focused on single-channel studies, where this might not apply to the multichannel system. Warrier et al. and Agostini and Bontemps focused their works on multichannel heat sinks using FC-18 and R134a as the cooling fluid, respectively [58,59]. Although correlations have been developed, no one correlation has been universally adopted by researchers. Furthermore, no correlations have been developed for transient operation.

2.2   Current Research on Transient Boiling in Microchannels

The previous sections discussed the relevant physical phenomena that occur in microchannel flow boiling. However, most of these studies were conducted at steady-state or by slowly increasing the heat load to the system while maintaining the flow conditions. The current study investigates the effects of transient heat loads. Few studies have been done investigating rapidly applied, transient heat loads. Nevertheless, some transient studies have been conducted which primarily focus on the test section temperature.

Basu et al. recorded heater wall temperature when performing experiments for transient boiling using HFE-7000 in a single channel with a hydraulic diameter of 0.34 mm [34]. Their results described the ONB and heater temperature as a function of heat flux (step response and frequency response) and mass flux. The experiments showed a heater temperature drop coinciding with the onset of boiling. Furthermore, high heat fluxes showed higher heater temperatures, but quicker times for the onset of boiling. Basu et al. experiments only considered one channel and did not examine the effects heat flux has on mass flow rate and pressure. Chen and Cheng studied the effect that pulsed heat load and mass flux have on nucleate and film boiling in a single silicon

microchannel [60]. The silicon microchannel was fabricated having a trapezoidal cross-section: 567 µm top width and 132 µm depth. Three mass fluxes were examined with a range of heat flux amplitude with pulses of 2 ms. Figure 2-6 shows the results on nucleate and film boiling as a function of heat load and mass flux. The figure shows with increasing mass flux, high heat fluxes
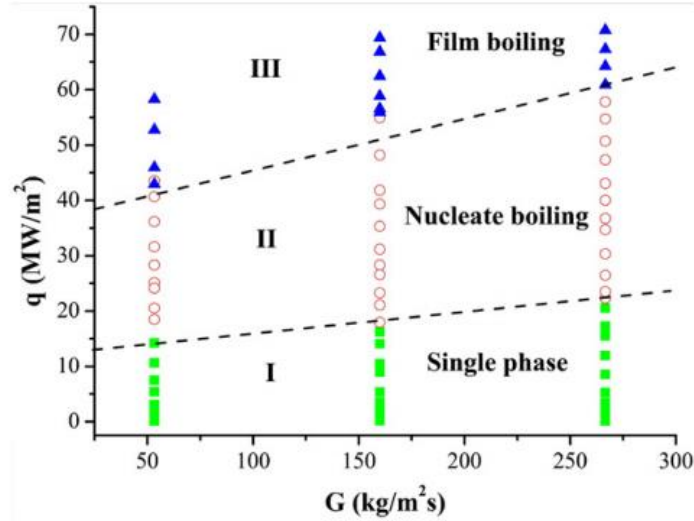
Figure 2-6. Flow boiling map under pulse heat load [59]

are needed to facilitate nucleate and film boiling. The authors measured the heater temperature during the pulsed loads. Heater temperature rose rapidly until the ONB but then had an oscillating profile instead of decreasing. The oscillating temperature was presumably due to flow instabilities, which the researchers did not mitigate with an inlet orifice. It was also peculiar that the temperature did not decrease at the ONB. The lack of decreases is likely caused by the short time frame the authors investigated, (2 ms). During this time vapor bubbles filled the channel, and for longer time periods, cooler bulk fluid would enter the channel and cool the heater before vaporizing.

Another study, by Huang et al., investigated the transient thermal response of a multi-microchannel evaporator (67 channels, height 100 µm, width 100 µm, and fin width 50 µm) with an inlet orifice using two refrigerants (R236fa and R245fa) [35]. They tested two types of heat loads: cold startup (0 to q_{max}) and periodic variations (from q_{min} to q_{max} with different pulse

periods). During the cold startup, the authors noted eight moments from the test section

temperature, seen in Figure 2-7 below. The heat load is applied at point A, where a rise in test
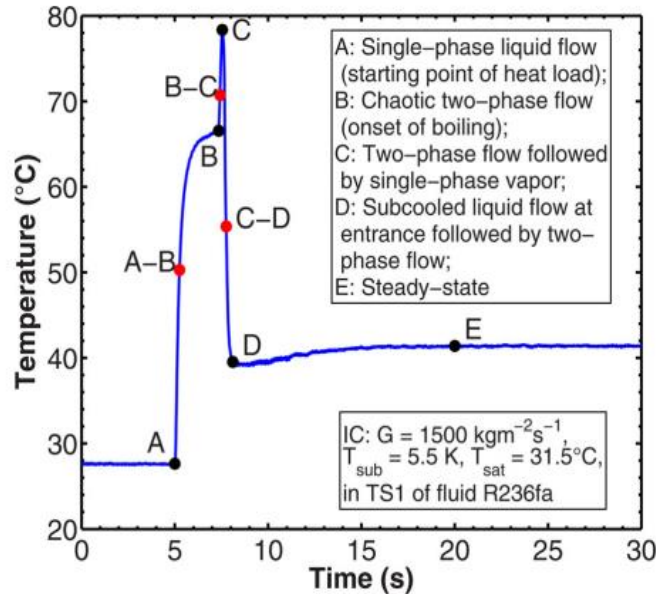
Figure 2-7. Experiment temperature results from Huang et al.
[35]

section temperature is seen until point B which marks the ONB. From point B to C vapor expands

the length of the channel, pushing away liquid to the inlet and outlet of the heat exchanger. At

point C the inlet pressure reaches a high enough value to push liquid refrigerant into the channels

resulting in a decrease in test section temperature and steady state boiling. The authors eliminated

the temperature rise (point B to C, Figure 2-7) from vapor filling the channels by adding a smaller

inlet orifice. In addition, the study demonstrated the maximum temperature can be lowered by

decreasing inlet orifice width, lowering heat flux magnitude (large enough to initiate boiling), and

lowering inlet subcooling and outlet saturation temperature. The time to initiate boiling increased

with increasing inlet orifice width, mass flux, inlet subcooling, outlet saturation temperature, and

fluid surface tension, but decreased with increasing heat flux. Overall, experimental data for

transient boiling in microchannels is still very limited and there is a need to better understand

transient boiling.

23

Robust and non-computationally demanding modeling of microchannel evaporators is highly sought due to the ease and quickness results can be generated. Jin et al. dynamically modeled a vapor compression cycle with an integrated microchannel evaporator [8]. Their model used a combination of lumped dynamic and static models to predict time-dependent pressure and temperature oscillations. Although they demonstrated the ability to model and optimize the vapor compression cycle, their model did not look at the instantaneous effects that a sudden heat load has on the cycle. Lamaison et al. developed a system-level model of a two-phase mini-thermosyphon with a microchannel evaporator [61]. Their model connected temporal and spatial differential equations to solve for mass and energy balances within the microchannel evaporator, condenser, and piping (downcomer and riser). The steady-state temperature of the micro-evaporator was over-predicted with a mean absolute error of 2.9%. Additionally, they modeled a dynamic heat load where they reached steady-state, and then reduced the heat load on the evaporator. Their model over predicted the decrease in the evaporator temperature. Although the model predicted steady-state and a transient decrease in heat load accurately, the model did not consider a rapid increase in heat load. Hodson et al. modeled a rapid increase in heat load to a microchannel cold plate[62]. Their dynamic model, built-in Simulink, uses a finite volume method to solve time-dependent mass, momentum and energy balances. The model uses empirical correlations found in the literature to solve for pressure drop and heat transfer in the two-phase fluid. The steady-state temperature of the cold plate was predicted reasonably well, in the worst case ~4% absolute error. The authors modeled a pulsed heat load and were unable to predict the temperature overshoot before ONB seen in their hardware and literature. They attributed the overshoot to sensible heating of the fluid, but did not have sufficient data to explore this.

Experimental studies on pulsed heat load showed large wall superheat temperatures before the ONB. After the ONB, the temperature of the test section decreased to a new steady-state value. There have been few efforts which model dynamic heat load on micro-evaporators. Hodson et al. made the most progress modeling pulsed heat loads. However, they were unable to model the overshoot in the temperature before the ONB.

2.3 Research Gaps in Transient Boiling

From the literature, transient heat loads on the performance of two-phase microchannel evaporators are poorly understood. Table 2-1 outlines the experimental literature on dynamic heat loads on two-phase microchannels. The current limitations of transient cooling systems this study aims to answer are listed below:

- Only one type of transient heat load have been examined. The effects of ramping the heat load have not been studied.

- Currently, experimental data collected is very limited and hydraulic diameters smaller than 100 µm have not been investigated.

- From the literature, there is no reduced order models that exists for transient heat loads, which are applicable to system level modeling.

Table 2-1. Current literature using dynamic heat loads

| Study | Microchannel Parameters | | | | | | | Heat Flux Parameters | | | Fluid (s) |
	Material	# Channels	Inlet Restriction	Channel Width [μm]	Channel Height [μm]	Hydraulic Diameter [μm]	Floor Thickness [μm]	Max Heat Flux [W cm^{-2}]	Pulse Load	Ramp Load	
Basu et al. [34]	Silicon	1	-	1200	200	343	0	675	x	-	HFE-7000
Chen & Cheng [60]	Silicon	1	-	567	132	214	0	7200	x	-	Water
Hodson et al. [62]	Copper	100	-	1000	1000	1000	unknown	unknown	x	-	R134a
Huang et al. [35]	Silicon	67	x	100	100	100	unknown	30	x	-	R236fa and R245fa
Current Study	Silicon	142	x	30	200	52	100	430	x	x	R134a

2.4   Focus of Current Investigation

The current study seeks to investigate transient heat loads on flow boiling in microchannels. A multi-microchannel silicon heat sink consisting of 142 channels connected to a two-phase pumped loop was used to collect experimental data. In Table 2-1 the current study can be seen compared to previous research. Current experiments have smaller hydraulic diameters, more channels, and a new method of applying transient heat loads. In addition to collecting experimental data, a simulation platform by P C Krause and Associates (PCKA) is used and altered to predict the transient temperature rise of the evaporator. It is warranted to create a tool which can reduced computational demand and to be used in system level modeling. The data collected from experiments is used to guide the modeling efforts.

CHAPTER 3 EXPERIMENTAL SETUP

The previous chapter discussed the lack of experimental data using dynamic heat loads in microchannel evaporators. The current study seeks to append to the limited inventory of current data using dynamic heat loads at hydraulic diameters smaller than previous studies. To gather data, a silicon microchannel evaporator fabricated by Lawrence Livermore National Lab was installed in a custom, in-house test facility. The following sections describe the test section development, test facility construction, and test matrix. Finally, the uncertainty of the measurements is discussed.

3.1 Test Section Description

The test sections used in the present study are fabricated from a 12 mm × 38 mm silicon wafer using a deep reactive ion etching (DRIE) process. The test section is shown in Figure 3-1.
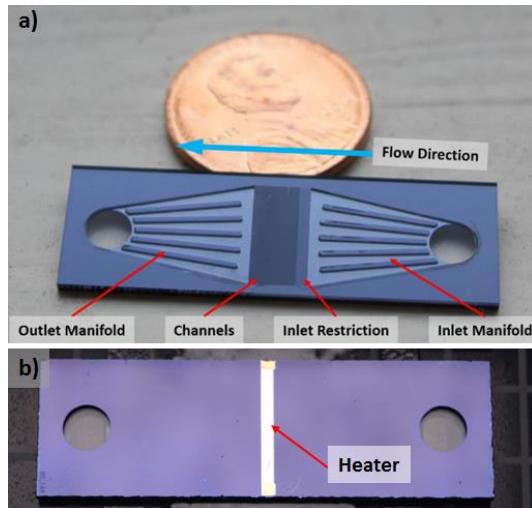
Figure 3-1. Overview of test section. (a) Channel side
of test section. (b) Back of test section with heater [65]

Fluid enters the test section and is evenly distributed using silicon ribs. Stated in chapter 2, flow instabilities are common in boiling in microchannels and have the potential to provoke CHF, damaging the device. To combat flow instabilities, an inlet restriction is etched into the silicon at

the channel inlet. Exiting the inlet restriction, the fluid enters the rectangular, 2mm long

microchannels. The fluid exits the channels into the outlet manifold, where supporting silicon ribs

guide the fluid to the outlet port. To provide a hermetic seal a 500 µm thick piece of borosilicate

glass is anodically bonded to the top of the test section. To simulate a laser diode bar, a thin film

platinum heater is deposited on the back of the channels. The platinum heater has the same

dimensions as a typical laser diode bar: 1 mm × 10 mm and is centered in the middle of the 2 mm

channels. The heater is placed in the middle of the channels, which causes a non-uniform heat load
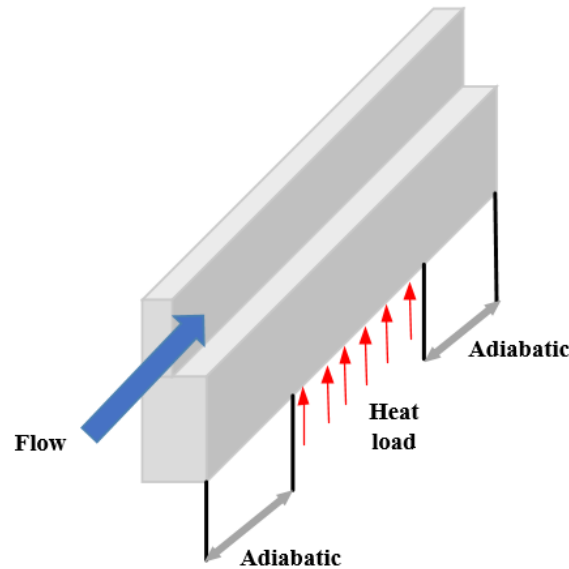
Figure 3-2. Non-uniform heat loading of channel

to occur. In Figure 3-2, the heat load is illustrated over a single channel. The fluid enters the 2 mm

channel subcooled, and the flow is considered adiabatic for the first 0.5 mm of the channel. After

0.5 mm, the heater is below the channels for 1 mm, the localized hot spot. Before exiting the

channel, the fluid flows through an additional 0.5 mm length of non-heat loaded channel. The on-

uniform heat loading occurs in all the channels that span the 10 mm width of the test section. Two

contact pads are placed on the heater to make an electrical connection where an induced current

produces Joule heating in the platinum. The heat transfers through the test section and heats the

28

fluid within the microchannels. The fluid is partially vaporized, exits the channels, and is guided to the outlet of the test section. The dimensions of the test section used in the current study are given in Table 3-1 below. One interesting aspect of this test section is the extremely small floor thickness. This feature brings the coolant close to the diode, decreasing the thermal resistance

Table 3-1. Test section geometry

Test Section Description	
Floor Thickness [µm]	100
Channel Width [µm]	30
Channel Height [µm]	200
Channel Length [µm]	2000
Fin Thickness [µm]	40
Inlet Orifice Width [µm]	15
Inlet Orifice Length [µm]	150

between the diode and working fluid.

The fabrication technique used to manufacture this test section is a deep reactive ion etching process. DRIE is a highly anisotropic etch process that is used to create channels with high aspect ratios. There are two main technologies for the DRIE process: cryogenic and Bosch [63]. The Bosch process was used in the present study. Figure 3-3 depicts the Bosch process in which a silicon wafer is constructed on a substrate and then modified [64]. In step 1 of the process, the wafer is covered with a photoresist material to cover the area which should not be etched. The silicon is then bombarded with plasma containing ions that vertically attack the exposed silicon (step 2). Next, an inert passivation layer, typically Octafluorocyclobutane, covers the wafer (step 3). The wafer is attacked with the plasma; however, the directional ions only attack the bottom of the trench causing the etch to become deeper, leaving the side walls nearly unscathed (step 4). The

attack and deposit of the passivation layer are repeated until the trench reaches the desired depth. One interesting aspect of the etching process is the scalloping produced on the channel walls.
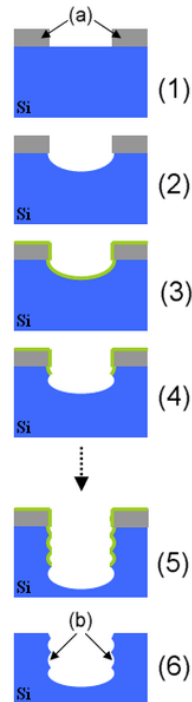
Figure 3-3. Bosch DRIE etching process [64]

Although the ion etch is applied vertically, the wall is still etched, which results in peaks and valleys along the channel wall, as shown in Figure 3-3. The peaks and valleys slightly increase the wall area, but in the current study, the wall is assumed to be flat.

3.2 Test Facility

The test facility used for this research was repurposed from a steady state facility constructed by Bevis [9] and several components were modified for compatibility with transient experiments. For example, the pyrometer used for steady state temperature measurement collected a single data point when the operator initiated the reading. This method was not practical for a transient study, where the temperature rapidly changes. Therefore, the facility was augmented with new hardware and software changes for transient operation. An IR camera was implemented to perform high

frame rate (120 Hz) temperature measurement, a programmable variable power supply was added to the system, the flow meter and gear pump were both moved closer to the test section inlet, and the data acquisition sampling rate was increased. These hardware and software changes are described in Sections 3.2.2 and 3.2.3 below.

The test facility used to conduct experiments is shown in Figure 3-4 below. Figure 3-5

Figure 3-4. Overview of test facility

shows a simplified schematic diagram of the facility and the major components. It can be used as a reference throughout this chapter. A detailed schematic and parts list is shown in Appendix A.
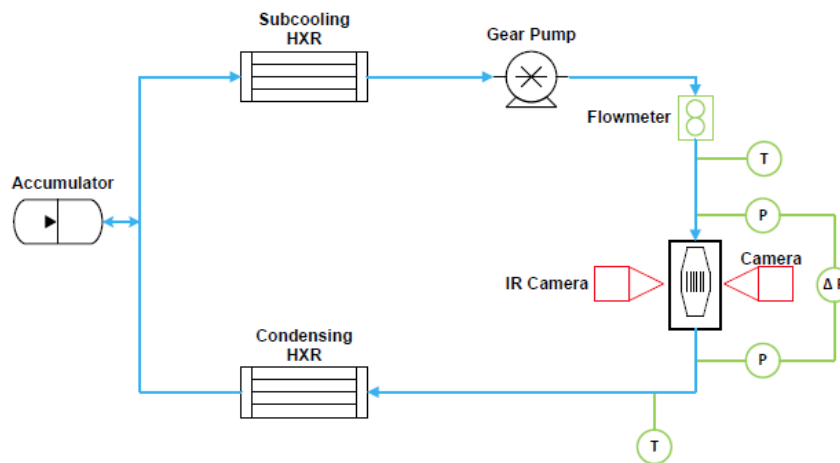
Figure 3-5. Schematic diagram of facility

The test facility is a two-phase pumped loop with a variety of mechanical, fluidic, pneumatic, and electrical systems. The total size of the experimental loop is 7 ft × 3 ft × 2.5 ft (length, width, height) and is in the Interdisciplinary Thermal Science Laboratory at the Powerhouse Energy Campus. The facility was designed for the working fluid Tetrafluoroethane (R134a), however, different fluids can be utilized. The fluid is circulated through the loop where is it partially vaporized in a microchannel evaporator. Two heat exchangers are used to condense the fluid and set the inlet test section temperature. The facility has bypass lines for maintenance and numerous sensors to record the fluid conditions throughout the loop. A computer is connected to a data acquisition system which records instrument measurements. The proceeding sections guide the reader through the loop, describing in detail the various components.

3.2.1 Test Section Interface with Facility Description

One of the most critical interfaces is between the test section and the test facility. Figure 3-6 shows the test section installed in its manifold and connected to the facility. The front of the test
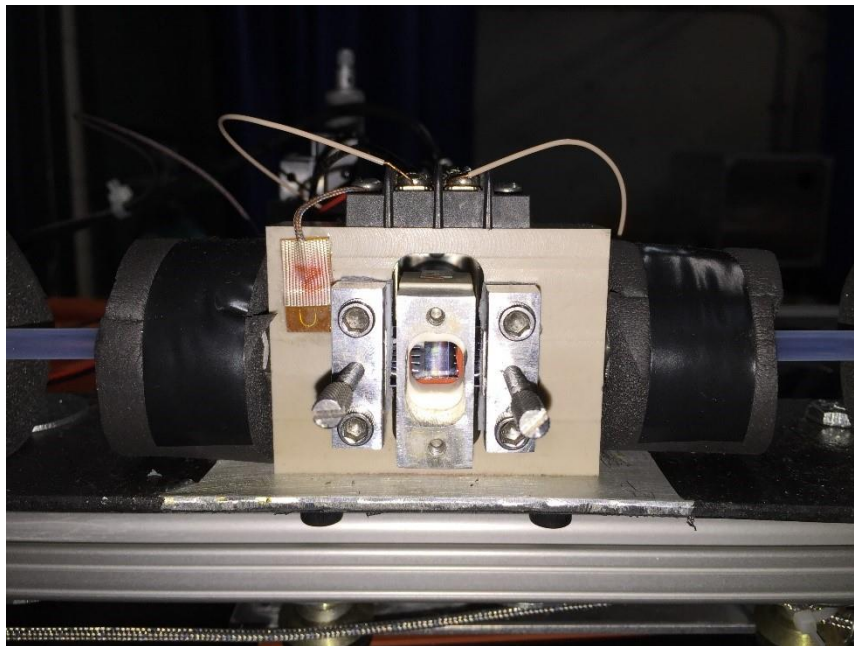
Figure 3-6. Test section installed in its manifold connected to the facility [9]

section is covered in clear borosilicate glass to optically capture the fluid movement in the channels. The back of the test section is exposed to allow the operator to take temperature measurements on the heater or the channels. Additionally, the backside of the test section is where electrical contact is made to the platinum heater. Figure 3-7 shows an exploded view of the test section installed in its manifold. A piece of polyether ether ketone (PEEK) was machined to create
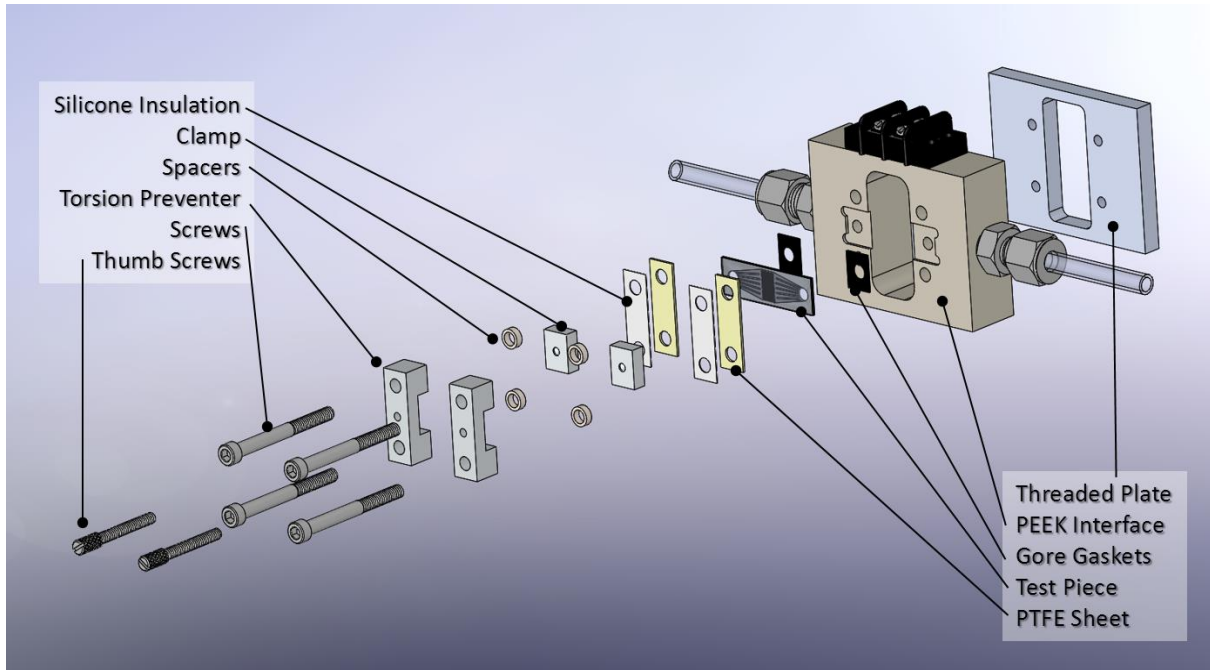
Figure 3-7. Manifold assembly to connect test section to facility [9]

a fluidic seal between the test section and test facility. PEEK was chosen due to its relatively low thermal conductivity (0.25 W m^{-1}K^{-1}), robust chemical compatibility, and high melting point. A thermocouple was placed on the PEEK block to monitor the temperature and ensure there was no heat loss through the PEEK to the environment during experiments. Two gore gaskets are placed between the test section and PEEK block. These create a seal and mitigate imperfections in the machining process that could damage the test section. Moving further to the left in Figure 3-7, two pieces of polytetrafluoroethylene (PTFE) and silicone are placed between the clamp and test section. The clamp, PTFE, and silicone apply pressure on the test section, creating a fluidic seal

without fracturing the extremely brittle silicon test section. Screws, thumb screws, and a threaded plate are used to hold everything together.

Figure 3-8 depicts how electrical contact is made to the test section. Two 24-gauge copper pins make contact to the contact pads on the test section. A wire is then soldered to the copper pins and connected to a power supply. A silicone gasket provides a gentle cushion for the test section, which is pressed between two pieces of ceramic. Thumbscrews and an aluminum plate hold the electrical contact manifold together.
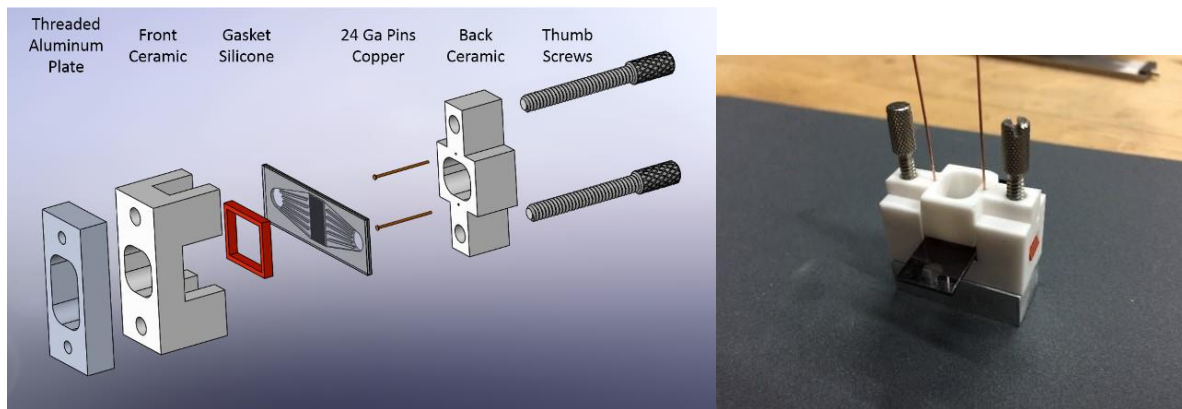
Figure 3-8. Left solid model of electrical connection to test piece; Right: Assembled test piece in electrical harness [9]

3.2.2 Test Section Measurements

Key measurements were taken from the hardware to evaluate the performance of the micro-evaporator. These measurements include the dynamic temperature change of the test section, the power dissipated at the test section, and the flow is the test section. In the steady state studies performed by Bevis, a pyrometer (Figure 3-9) took single temperature measurements (1 mm) and manually scanned the test section. Using the pyrometer is an insufficient method for the current study, due to the rapid temperature change after an applied heat load. Therefore, an infrared (IR) camera was employed (Micro-Epsilon, TIM 160), seen in Figure 3-10. The IR camera has a frequency of 120 Hz, gathering temperature readings on the test section every 8 ms. The camera

is placed approximately 4 inches from the test section, prompting a 0.3 mm pixel size. The camera
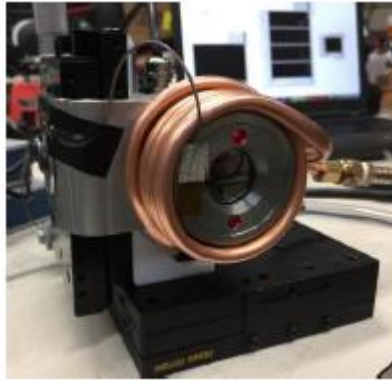
Figure 3-9. Pyrometer used in Bevis steady-state study [9]

data is collected via a USB connection to a computer. A data processor created by Micro-Epsilon

is employed to perform data analysis. IR cameras are extremely sensitive to the emissivity of an

object and highly reflective surfaces will lead to inaccurate readings. Therefore, high emissivity

paint is coated on the backside of the test section to increase the measurement accuracy.
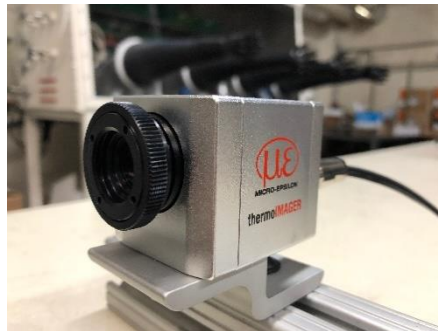
Figure 3-10. Infrared camera used in current study

The temperature change of the test section is a result of Joule heating from a current running

through the resistive heater on the test section. To apply a voltage, a power supply is utilized. In

the Bevis study, a non-programmable power supply was used, and the user manually set the power.

The current study investigated rapid pulse and ramped heat load; therefore, the power supply was

modified. Figure 3-11 shows the power supply used by Bevis and the programmable power supply

used in this study. The programmable power supply (Agilent N8735A) is used in conjunction with

Benchvue software (Keysight Technologies). The software allows the user to input a wide range of time-dependent, dynamic voltages. To accurately calculate the power dissipated at the test section, the voltage at the test section is measured, and a highly accurate ($<0.01\%$) shunt resistor (Omega PX409-100DWUI) is used to calculate the current based on the voltage drop.
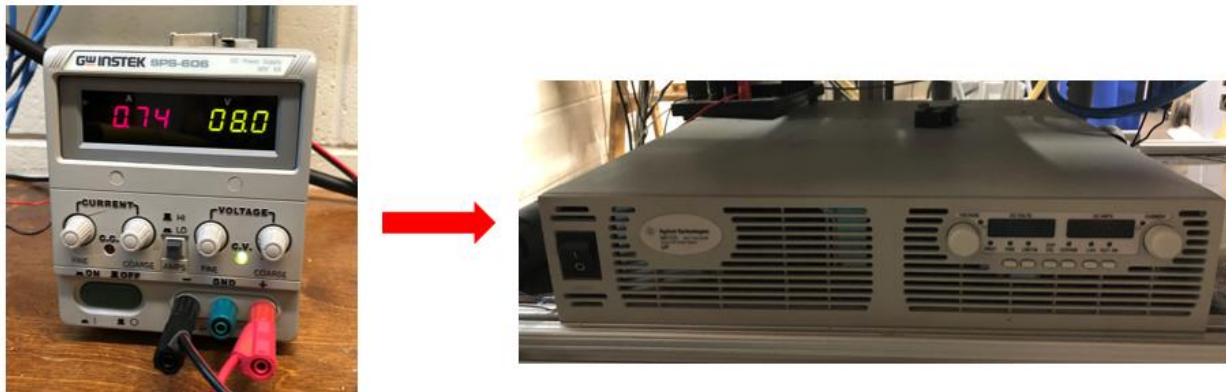
Figure 3-11. Power supply used in Bevis study (left). Programmable power supply used in current study (right)

After the heat load is applied, the fluid dynamics occurring within the test section was investigated. To view the fluid during experiments, a microscope camera (DinoLite 2.0) is placed in front of the test section. Figure 3-12 shows the microscope camera in its position during testing.
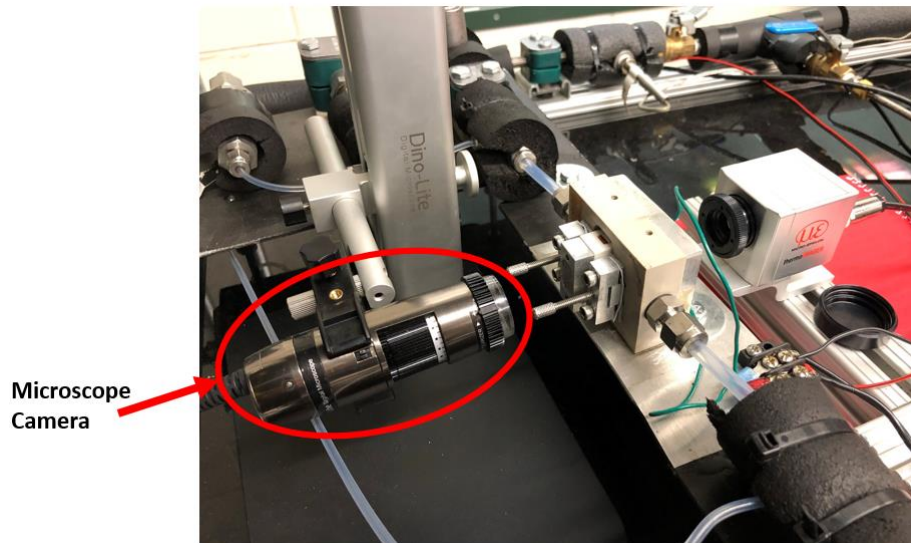
Figure 3-12. Microscopic Camera

The frame rate was set at twenty frames per second (fps). The camera connects to the computer, and the imaging software created by Dino-Lite is used to record data.

3.2.3   Fluid Control and Measurement

Two plate heat exchangers (Koolance HXP-193), located upstream and downstream of the test section, are used to control the fluid temperature in the fluid loop. The heat exchanger downstream of the test section condenses the two-phase fluid, while the upstream heat exchanger adjusts the inlet temperature of the fluid before entering the test section. The heat exchangers are connected to a secondary ethylene-glycol loop which is cooled by a chiller (Thermofisher M150LR-CP55). The ethylene-glycol flow rate is controlled with a manual needle valve placed between the chiller and heat exchangers. The temperatures are monitored and controlled via four type-K thermocouples (Omega TC-K-NPT-UG-72): at the inlet of the test section, the exit of the test section, after the condenser heat exchanger, and before the subcooling heat exchanger.

A positive displacement gear pump (Cole-Parmer GA-T32) is used to circulate the R134a fluid through the system. The gear pump is magnetically coupled to a gear pump drive (Cole-Parmer wu-75211-10). The operator can adjust the speed of the pump by manually turning the potentiometer on the drive. The gear pump was moved from before the condenser in the Bevis study to after the subcooling heat exchanger in the current study. The change in location was completed to reduce the pressure drop between the test section and the pump outlet. To monitor the flow rate, a highly accurate (0.50 %) Coriolis flowmeter (Rheonik RHM015) is placed at the inlet of the test section. Additionally, the flow meter was moved from before the subcooler (Bevis study) to just upstream of the test section. The flow meter was moved closer to the test section to ensure there was no lag in flow rate measurement during dynamic testing.

A bladder accumulator (Accumulators Inc. A1QT3100) placed between the heat exchangers adjusts the system pressure. The accumulator works by pressurizing the non-fluid side of the bladder with compressed gas to add or remove R134a from the system. The operator controls the bladder pressure manually using a ball valve between the accumulator and compressed gas line. Absolute fluid pressure transducers (Omega PX409-100DWUI) are placed upstream and downstream of the test section and after the condenser to monitor the system pressure. An additional analog absolute pressure sensor is placed on the compressed gas side of the accumulator. In addition, a differential pressure transducer (Omega MMA100C1P2CF0T4A6) is connected across the test section.

3.3   Test Matrix

The purpose of this study is to gather flow boiling data using dynamic heat loads on the microchannel heat sink. The nominal inlet conditions used in this study were held constant throughout all tests: flow rate 50 g min^{-1}, inlet pressure of 83 psi (saturation temperature of 20 ^{o}C), and 5°C subcooled. Once the properties of the system reached steady-state, a heat load was applied. Data was collected prior, during, and after heat was applied. Two types of heat loads were used: pulsed and ramped. In pulsed tests, heat was applied using a single step function (zero to max). In the ramped test, the power is rapidly or gradually increased using a small step function at a set time interval. Initial testing showed critical heat flux occurring at approximately 60 Watts, for a flow rate of 50 g min^{-1}. Additionally, extremely high dynamic superheats were seen at high heat loads. To avoid damaging the test section, the heat loads were limited to 50 Watts. Table 3-2 outlines the tests completed in this study. The pulsed heat load tests were performed to simulate a rapid optical output of a laser diode. The ramped tests were used to investigate the effects of slowly

increasing the optical output and to determine if ramping has better thermal management of peak

temperatures compared to pulse.

Table 3-2. Experiments performed

Type of Heat Load	Max Power [W]	Ramp Rates [W s⁻¹]
Pulsed Heat Loads [W]	15, 20, 30, 35, 38, & 43	-
Ramping Heat Loads [W]	38	4-50

3.4   Uncertainty

An uncertainty analysis was performed to evaluate the accuracy of the test data. The

uncertainty is typically composed of two main sources of error: bias error and precision error. Bias

error is inherent to the device and typically determined by the manufacturer. Precision error, or

random error, is error caused by unknown and unpredictable changes during an experiment. By

combination of bias and precision error one can determine the overall error of the device using

equation (3.1) below:

$$U = \sqrt{B^2 + P^2} \qquad (3.1)$$

Where B is the bias error, and P is the precision error. The precision error can be found using

equation (3.2), where k is the student T coverage factor, S_x is the standard deviation of the data,

and N is the number of data points taken.

$$P = k \frac{S_x}{\sqrt{N}} \qquad (3.2)$$

Since the current study is using transient data, a collection of data points for a particular transient

heat load cannot be collected. Therefore, steady-state data collected prior to an imposed heat load

was used for the uncertainty analysis. Table 3-3 shows an example of an uncertainty analysis performed for the main measurements on the system: inlet pressure transducer, inlet thermocouple, differential pressure transducer, and mass flow meter. It is clear that the bias error dominates the total uncertainty. Due to the nature of infrared camera imaging, adjacent reflective materials and ambient temperature can affect the measurements. To reduce the amount of error, a calibration was performed, and details of the calibration process can be found in Appendix A.2. The accuracy of the infrared camera was improved from ±2°C to ±0.2°C.

Table 3-3. Uncertainty analysis example for inlet conditions

Instrument	Bias Error	Precision Error	Total Uncertainty	Unit
Flow Meter	0.5	0.0189	0.5	g min^{-1}
Inlet Pressure Transducer	0.08	0.0045	0.08	psi
Differential Pressure Transducer	0.04	0.0066	0.0405	psi
Inlet Thermocouple	0.36	0.0036	0.36	°C

CHAPTER 4 DATA REDUCTION

The previous chapter discussed the facility used to record data for dynamic experiments. Another specific goal of the present work is to develop non-computationally demanding, robust modeling methods. The current chapter explains the modeling method used to compare to experimental data collected. The model was built on previous software from PCKA, named AFRL Transient Thermal Management Optimization (ATTMO). The model was augmented to most accurately represent the current test section and the dynamic responses to transient heat loads. In this chapter the microchannel evaporator fundamental methods are explained, followed by the inputs used to model the microchannel evaporator accurately.

4.1   Microchannel Evaporator

The transient microchannel model is a variation of an ATTMO toolset that was developed to simulate dynamic modeling of vapor compression cycles. ATTMO is implemented within the commercially available software MATLAB/Simulink. The toolset is comprised of various system components such as heat exchangers, pumps, piping, flow generators, accumulators, etc. Each component is modeled by a Simulink module that predicts the performance based on user inputs and/or inputs from downstream and upstream component modules in the system. In the thermal suite is a microchannel heat exchanger model which is referenced to a two-phase cold plate. The cold plate simulates the transient heat transfer and flow dynamics occurring from an imposed heat load. The cold plate can perform single-phase and two-phase simulations and has four different flow configurations: Serpentine, Split, Offset Fin, and Microchannel flow. The user can add additional material layers that vary in properties below the channels. The platform has a graphical user interface (GUI) for a microchannel flow configuration. The GUI has the following user inputs:

the channel geometry and material; cold plate dimensions, and temperature; bottom layer material(s) and thickness; and the total mass of the cold plate in kilograms. The user enters the initial flow conditions which include the fluid type, fluid temperature, fluid pressure, fluid flow rate, and quality (if two-phase). The GUI also allows the user to toggle two-phase pressure drops
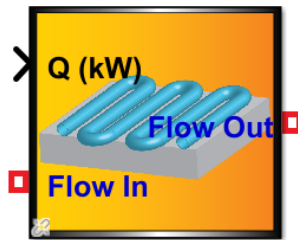
Figure 4-1. Cold plate Simulink module block

calculations, which is useful for quick calculations. Figure 4-1 shows the module for the cold plate. The module in Figure 4-1, allows connection of other components or data from hardware to be fed into the cold plate. Three main connections are made into the cold plate module: heat load ("Q (kW)"), Flow in, and Flow out. Generic Simulink blocks and ATTMO generated blocks can be connected to the cold plate to replicate the user's model. The ATTMO toolset allows the user to setup a nodal network to perform the dynamic calculations internally throughout the cold plate. Calculations are performed at each node and time-step, and computational time is dependent on how fine the nodal network is configured. The model subdivides the cold plate to perform calculations independent of each other. Figure 4-2 details how the model breaks down the cold plate. Three main divisions can be seen: fluid, heat transfer, and bottom layer. The fluid flow solves the mass, momentum, and energy balances within the fluid. The heat transfer calculation the two-phase heat transfer into the fluid by assuming a uniform heat transfer coefficient in the y direction at each node. In the bottom layer, the transient enthalpy within the substrate is calculated. Furthermore, the model performs each calculation at each node. A representative nodal network

42

can be seen in Figure 4-2. The nodal network is created by the user and level of accuracy depends on quality of the mesh. The following sections discuss the equations used within ATTMO.
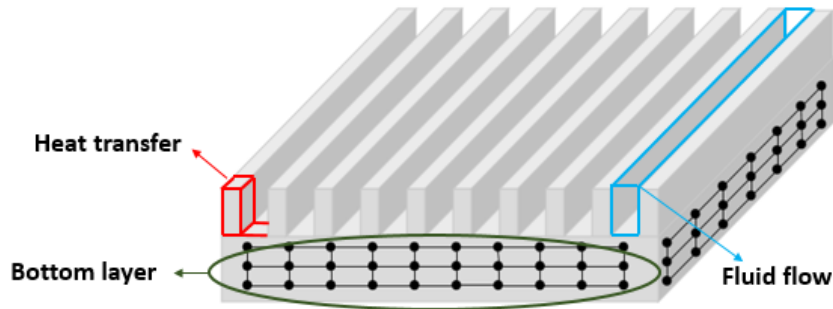
Figure 4-2. Cold plate subdivided

4.1.1 Dynamic Fluid Calculations

To perform dynamic fluid calculation between the nodes of the cold plate, ATTMO employs a finite volume approach to solve time-dependent mass, momentum, and energy balances (Figure 4-3). To increase computation speed of the model pressure drop is ignored. To validate
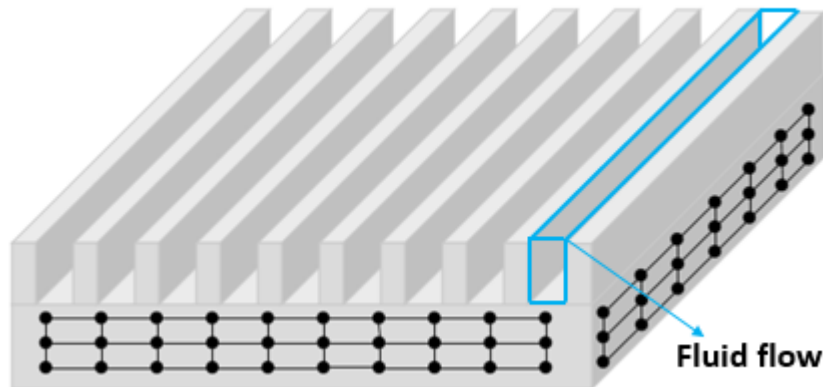
Figure 4-3. Dynamic fluid flow calculations

this assumption the model is ran at the highest pressure (inlet pressure, 573.71 kPa) and the lowest pressure (outlet pressure, 562.62 kPa) seen in the experiments. Using the outlet and inlet pressure readings with include all minor losses seen upstream and downstream of the channels. By

43

including the minor losses, this will exacerbate the temperature difference, as the pressure drop in the channels is much lower than the readings. A temperature difference of 0.69°C was found, the temperature difference is not significant; therefore, the assumption is used. If the pressure drop calculations are ignored, the following mass (4.1) and energy (4.2) balance equations are used:

$$V_{\text{n}} \left[\frac{\partial \rho_{\text{n}}}{\partial P} \frac{dP}{dt} + \frac{\partial \rho}{\partial h} \frac{dh_{\text{n}}}{dt} \right] = \dot{m}_{\text{n-1}} - \dot{m}_{\text{n}} \tag{4.1}$$

$$V_{\text{n}} \left[\left(h_{\text{n}} \frac{\partial \rho_{\text{n}}}{\partial P} - 1 \right) \frac{dP}{dt} + \left(h_{\text{n}} \frac{\partial \rho_{\text{n}}}{\partial h} + \rho_{\text{n}} \right) \frac{dh_{\text{n}}}{dt} \right] = \left(\dot{m}h \right)_{\text{n-1}} - \left(\dot{m}h \right)_{\text{n}} - Q_{\text{fl\_n}} \tag{4.2}$$

The heat rate into the fluid is calculated using equation (4.3) below:

$$Q_{\text{fl\_n}} = U A_{\text{s}} (T_{\text{fl\_n}} - T_{\text{w\_n}}) \tag{4.3}$$

where A_{s} is the surface area, $T_{\text{fl\_n}}$ is the temperature of the fluid, $T_{\text{w\_n}}$ is the wall temperature, and U is the overall heat transfer coefficient. The overall heat transfer coefficient is the thermal resistance of the fins and thermal resistance of the fluid. Equation (4.4) shows the equation for the overall heat transfer coefficient.

$$\frac{1}{U} = \frac{1}{ht_{\text{tp}}} + \frac{A_{\text{s}}}{\eta_{\text{f}} ht_{\text{tp}} A_{\text{f}}} \tag{4.4}$$

Where ht_{tp} is the heat transfer coefficient (HTC), η_{f} is the fin efficiency, and A_{f} is the fin area. The heat transfer coefficient is found using empirically developed correlations. Many correlations exist for various geometries and flow conditions; therefore, the correct correlation must be applied to the user situation. ATTMO has prescribed correlations built into the program, depending on the type of cold plate the user chooses. Currently, ATTMO employs a correlation developed by Kim and Mudawar [51] for two-phase flow in rectangular channels. However, Burk's computational study on heat transfer correlations using the test sections in the current study, resulted in Kim and

Mudawar correlation over predicting the HTC [65]. The difference in HTC is likely due to smaller hydraulic diameters and working fluid used in this setup. Based on Burk's findings, this study added two additional HTC correlations, Agostini and Bontemps, and Bertsch et al., into ATTMO [53,59].

4.1.2   Heat Transfer Calculations

The previous section described the governing energy equation to calculate the heat transfer into the fluid. However, the HTC in equation (4.8) is unknown. ATTMO calculates the HTC separately to find the heat load into the fluid and feeds the heat load back into the fluid flow calculations. The calculation is completed at each node and implements a fin efficiency to find the total heat load into the node. The modeling approach assumes a constant HTC at each node along the channel. Where/how the heat transfer coefficient calculations are perform is shown in Figure 4-4.
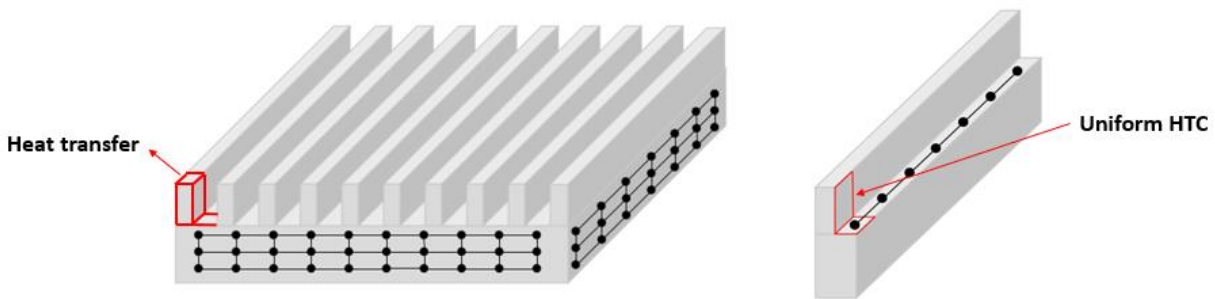
Figure 4-4. Heat transfer calculations into the fluid

The HTC is derived from empirical data gathered by researchers. This section details the correlations used in this study. One two-phase heat transfer coefficient correlation used in this study was developed by Agostini and Bontemps [59]. This correlation was chosen due to previous studies showing good agreement with this fluid and channel geometry [9,65]. Agostini and Bontemps developed their model using 11 parallel rectangular channels with a hydraulic diameter

45

of 2.01 mm. The working fluid was R134a, the same fluid used in the current study. They tested a range of max fluxes (90 to 295 kg m^{-2}s^{-1}) and a range of heat fluxes (6 to 31.6 kW m^{-2}). The correlations developed by the authors are found in equations (4.5) and (4.6):

$$ht_{tp} = 28q''^{\frac{2}{3}} \dot{m}^{-0.26} x^{-0.1} \qquad \text{if } x < 0.43 \qquad (4.5)$$

$$ht_{tp} = 28q''^{\frac{2}{3}} \dot{m}^{-0.64} x^{-2.08} \qquad \text{if } x > 0.43 \qquad (4.6)$$

A composite correlation for flow boiling in microchannels developed by Bertsch et al. was explored in addition to the Agostini correlation [53]. The correlation accounts for nucleate and convection boiling while considering the confinement of bubble growth in small channels. Using 3899 data points from 14 studies the correlation accounted for hydraulic diameters from 0.16 to 2.92 mm, confinement numbers of 0.3 to 0.4, mass fluxes from 20 to 3000 kg m^{-2} s^{-1}, and heat fluxes from 0.4 to 115 W cm^{-2}. The authors concluded they could achieve a mean absolute error of less than 30% with this correlation. The correlation developed by Bertsch et al. can be seen in the equations (4.7) - (4.13) below:

$$ht_{tp} = ht_{NB} S + ht_{conv,tp} F \qquad (4.7)$$

$$ht_{NB} = 55 P_r^{0.12-0.2\log_{10} R_P} (-\log_{10} P_r)^{-0.55} M^{-0.5} (q'')^{0.67} \qquad (4.8)$$

$$ht_{conv,tp} = ht_{conv,l} (1-x) + ht_{conv,v} x \qquad (4.9)$$

Where,

$$ht_{conv,l} = \left(3.66 + \frac{0.668 \dfrac{D_h}{L} \mathrm{Re}_l \mathrm{Pr}}{1 + 0.04 \left[\dfrac{D_h}{L} \mathrm{Re}_l \mathrm{Pr} \right]^{\frac{2}{3}}} \right) \frac{k_l}{D_h} \qquad (4.10)$$

$$ht_{conv,v} = (3.66 + \frac{0.668\frac{D_h}{L}\text{Re}_v\,\text{Pr}}{1+0.04\left[\frac{D_h}{L}\text{Re}_v\,\text{Pr}\right]^{\frac{2}{3}}})\frac{k_l}{D_h}$$ (4.11)

$$F = 1 + 80(x^2 - x^6)e^{-0.6Co}$$ (4.12)

$$S = (1 - x)$$ (4.13)

From the correlations above, the HTC is a heat flux dependent boundary condition. However, the heat flux is dependent upon the HTC. Therefore, an iterative method must be used to solve for the HTC. ATTMO uses a boiling number convergence method to iteratively solve for heat transfer
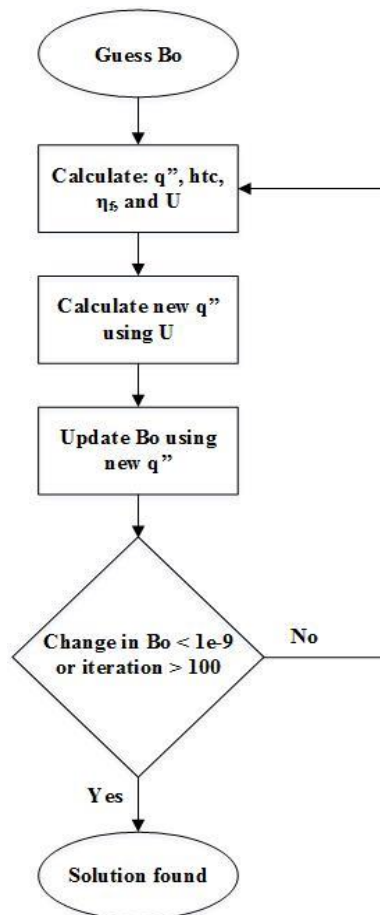
Figure 4-5. Heat Transfer Coefficient Iteration Procedure

47

coefficient as is shown in Figure 4-5. The boiling number, which represents the ratio of the mass of vapor generated per unit area of heat transfer to the mass flow rate per unit flow, is shown in equation (4.14):

$$Bo = \frac{q''}{\dot{m}h_{fg}} \tag{4.14}$$

The boiling number is a function of the heat flux; therefore, it is used as the initial guess to solve for the heat flux. Once the heat flux into the fluid is calculated, the HTC from the correlation can be found. From the geometry and properties of the cold plate and HTC, the fin efficiency of the cold plate is found using equations (4.15) and (4.16) below:

$$m = \sqrt{\frac{ht_{tp}}{k_f t_f}} \tag{4.15}$$

$$\eta_f = \frac{\tanh(mL_c)}{mL_c} \tag{4.16}$$

Now that the heat transfer coefficient and fin efficiency is known, the overall HTC can be calculated from equation (4.4). Finally, updated heat flux and boiling numbers are found using the equations (4.3) and (4.14). If the change in the boiling number is less than 1×10^{-9} or the number of iterations reaches 100, the solution is found.

Above the two-phase HTC and fin efficiency equations were described. However, the fluid enters the channels subcooled. Therefore, single-phase HTC calculations are perform. The Reynolds number described how turbulent the flow is and has an impact of the single-phase HTC. To be exact, the Reynolds number represents the ratio of inertial forces to viscous forces within a fluid as shown in equation (4.17):

$$Re = \frac{\rho V L_c}{\mu} \tag{4.17}$$

The single-phase HTC used in this study was the ATTMO default. The correlation is determined from the Reynolds number, where the flow can be laminar, transitional, or turbulent. If the Reynolds number is less than 2500 the flow is laminar. For laminar flow the Nusselt number (Nu) is a function of the aspect ratio ($beta=width/height$) of the channels. The Nusselt number is a dimensionless number that is the ratio of convective to conductive heat transfer in the fluid. Using the Nusselt number, hydraulic diameter, and thermal conductivity of the fluid, the single-phase HTC for laminar flow can be found from equations (4.18) and (4.19), assuming fully developed flow:

$$Nu = 8.235(1 - 1.833beta + 3.767beta^2 - 5.815beta^3 + 5.361beta^4 - 2beta^5) \qquad (4.18)$$

$$ht_{sp,laminar} = \frac{Nu*k}{D_h} \qquad (4.19)$$

If the Reynolds number is greater than 3500 the flow is turbulent and the HTC is a function of the Reynolds number, fluid properties, and hydraulic diameter, seen in equation (4.20):

$$ht_{sp,turb} = 0.023 \, \mathrm{Re}^{0.8} \, \mathrm{Pr}^{0.4} \frac{k}{D_h} \qquad (4.20)$$

For a Reynolds number between 2500 and 3500 the flow is transitional, meaning the fluid is a mixture of laminar and turbulent flow. The heat transfer is found using a relationship between the laminar and turbulent heat transfer correlations, as is shown in equation (4.21):

$$ht_{sp,trans} = \frac{ht_{sp,laminar}(3500 - \mathrm{Re})}{1000} + \frac{ht_{sp,turb}(2500 - \mathrm{Re})}{1000} \qquad (4.21)$$

4.1.3   Bottom Layer Calculations

One of the key inputs to the ATTMO model is the layers of material below the channels which are designed as a nodal network (Figure 4-6). The internal nodes within the bottom layer are calculated separately from the fluid flow and HTC and the program iterates between the bottom

layer module and other two modules to converge on a cold plate temperature. To calculate the temperature of the cold plate, the transient enthalpy change within the internal nodes is, equation (4.22):

$$\rho_n V_n \frac{dh_n}{dt} = \sum_{i=1}^{int} \frac{k_i A_i}{dx_i}(T_{n-1} - T_n)$$
(4.22)

Where ρ is the density, V is the volume of the node, h is the time-dependent enthalpy, k is the thermal conductivity, T is the temperature, and A is the area. The volume and area are calculated
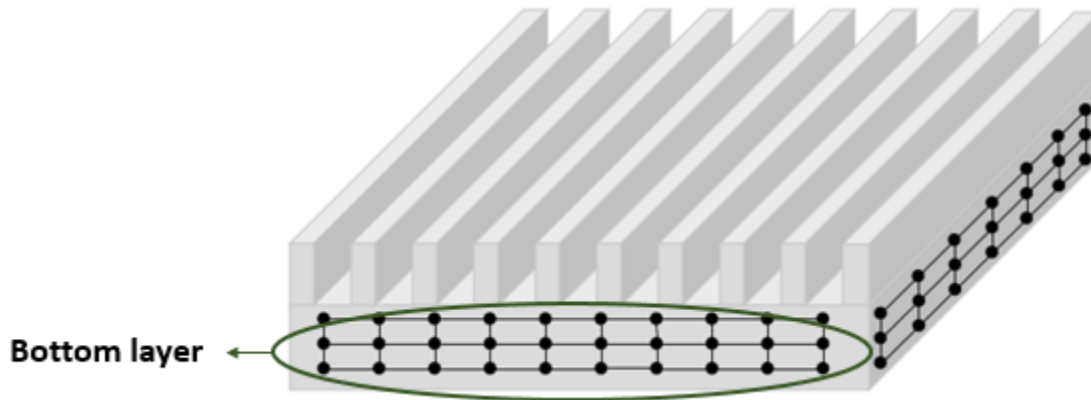
Figure 4-6. Bottom layer calculations

from the nodal network and size of cold plate created by the user. The material properties are stored in a mat file that is called when needed. The program has a variety of metals, composites, and phase change materials that the user can choose from. The GUI has an additional option for a user-defined material. In the current study, silicon was added as a user defined material by entering density, thermal conductivity, and specific heat. The material properties in this study were assumed constant at 20°C and taken from Engineering Equation Solver: Density 2328 kg m^{-3}, conductivity 0.168 kW m^{-1} K^{-1}, and specific heat 0.6857 kJ kg^{-1} K^{-1}.

4.2   Model Inputs

The proceeding sections expounded on the modeling methods and correlations used by ATTMO. To evaluate the accuracy of the two-phase evaporator model, data from experiments was directly input into the model. ATTMO has graphical user interfaces that allow the user to generate a model that is representative of their situation. In addition, Simulink has blocks which allow the user to input external data from various file types. All Simulink blocks are compatible with the ATTMO library, thus making hardware inputs into the cold plate simple. The succeeding sections delineate and justify the model inputs and assumptions used in the current study.

4.2.1   Cold Plate Configuration and Assumptions

To configure the cold plate, all dimensions are input into the GUI. The dimensions used in the current study are shown in Figure 4-7. As stated in Chapter 3, the cold plate has a 100 µm thick silicon layer below the 200 µm tall channels, which is sealed with borosilicate glass. It is assumed

Figure 4-7. Cold plate GUI with user inputs

that the glass above the channels is insulated; therefore, an adiabatic assumption is used. To validate this assumption, a calculation can be performed to find the heat loss through the glass to

the ambient. Figure 4-8 shows the thermal resistance network from the fluid to the atmosphere. The heat loss through the glass can be calculated using equation (4.23):

$$Q = \frac{T_{fluid} - T_{air}}{R_{total}}$$

(4.23)

Where the total equivalent thermal resistance is seen in equation (4.24):

$$R_{total} = R_{cond,glass} + \frac{R_{conv,air} R_{rad,air}}{R_{conv,air} + R_{rad,air}}$$

(4.24)

The thermal resistances in equation (4.24) can be calculated using equations (4.25) - (4.29):

$$R_{cond,glass} = \frac{L_{glass}}{K_{glass} A_s}$$

(4.25)

$$R_{conv,air} = \frac{1}{h_{air} A_s}$$

(4.26)

$$R_{rad,air} = \frac{1}{h_{rad,air} A_s}$$

(4.27)
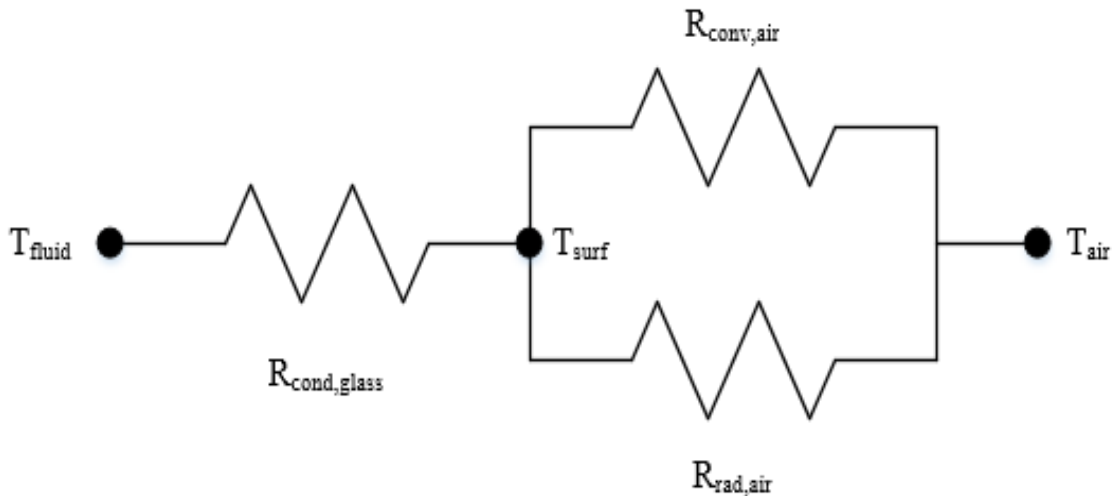
Figure 4-8. Thermal resistance network through borosilicate glass to atmosphere

Where,

$$A_s = L_{\text{channel}} * N_{channel}(W_{\text{channel}} + W_{fin})$$ (4.28)

$$h_{\text{rad,air}} = \sigma\varepsilon\left(T_{\text{surf}} + T_{\text{air}}\right)\left(T_{\text{surf}}^2 + T_{\text{air}}^2\right)$$ (4.29)

Table 4-1 details the properties used to find the heat transfer across the glass. A conservative estimate of the air side heat transfer coefficient of 20 W m^{-2} K^{-1} was used. The radiation heat transfer coefficient (equation (4.29)) is found by multiplying the Stefan-Boltzmann constant (σ) by the emissivity (ε) and the temperature difference to the fourth power. A blackbody assumption was made and the emissivity was set to one. The surface temperature was unknown and was assumed to be the same temperature as the ambient air. This assumption will lead to an over approximation of the radiation HTC because in reality the temperature of the surface will be lower than the air temperature. The increase in surface temperature assumption increases the HTC, lowering the total thermal resistance. The thermal resistance of the fluid was neglected, and the temperature of the glass was assumed to be the subcooled temperature of the fluid (288.2°K). Based on the assumptions listed above, the heat gain from the ambient air was calculated as 3 ×

Table 4-1. Values used for adiabatic through glass assumption

Constant	Value	Units
T_{fluid}	288.2	[K]
T_{air}	294.3	[K]
T_{surface}	294.3	[K]
K_{glass}	1.14	[W m^{-1}K^{-1}]
L_{glass}	5E-04	[m]
L_{channel}	2E-03	[m]
W_{channel}	1E-02	[m]
σ	5.67E-08	[W m^{-2}K^{-4}]
ε	1	-

53

10^{-3} W. With heat loads on the order of 50 Watts, the heat gain is negligible and an adiabatic assumption can be assumed.

The user also can set an adiabatic or non-adiabatic condition on the bottom of the cold plate where the heater is located. The current study assumes an adiabatic assumption and a similar procedure was performed to calculate the heat loss to ambient. The thermal resistance network for the heater to the ambient is seen in Figure 4-9. The total equivalent resistance was found using equation (4.30) below:

$$R_{total} = \frac{R_{conv,air} R_{rad,air}}{R_{conv,air} + R_{rad,air}}$$

(4.30)

The temperature of the heater is the steady-state value for a 43 Watt heat load ($T_{heater} = 36°C$). The area is assumed to be the area of the heater (1×10^{-5} m^2). The same assumptions for air (294.3°K)
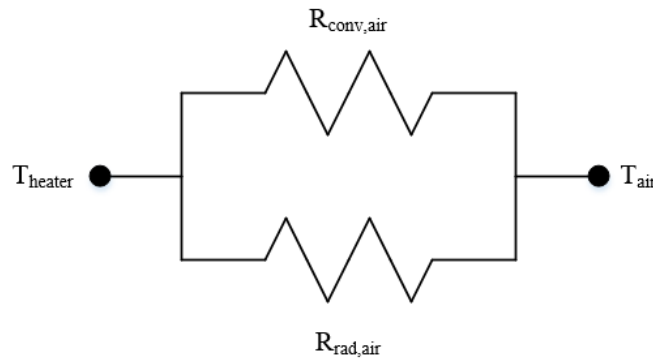
Figure 4-9. Thermal resistance network from the heater to the ambient

and emissivity (1) used previously are used in this case. The heat loss to the environment is found to be 3.9×10^{-3} W. Again, this is a negligible amount, and the adiabatic assumption on the heater is validated.

To configure the cold plate in ATTMO, a nodal network must be created. The nodal network quality is created using three direction: Nx, Nz, and Ny, seen in Figure 4-10. The number of nodes in these section (Ny) was set a minimal of one, to increase computational speed. It was

found the number of nodes in this direction had little effect on the temperature. The channel height is set to the same value as the height of the cold plate. If this is not done, ATTMO will assume the
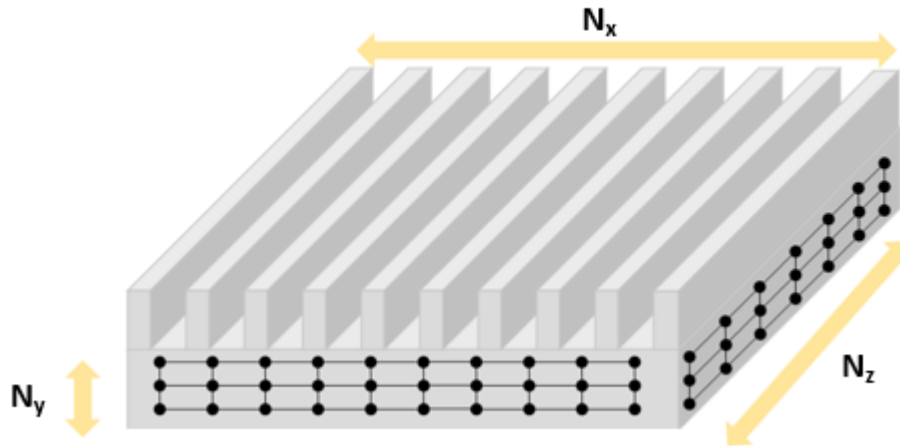
Figure 4-10. Nodal network layout for the cold plate

channels are in the middle of the cold plate which will add additional material between the fluid and the heat load, and an additional layer above the channels. The number of nodes chosen perpendicular to the flow direction (Nx) was 1 in this study. Increasing the number of nodes in the Nx direction had little effect on the temperature distribution and greatly increased the computational time. The number of nodes set in the flow direction (Nz) is 20. To justify the nodal network used in this study, a sensitivity analysis was completed. Table 4-2 shows the changes in average heater temperature using different nodal networks. If computational time was greater than 2 hours the simulation was cancelled and no temperature was recorded, this occurred when Nx was 5 and Nz was 28. Increasing the number of nodes had little impact on the average heater and also increased computational time dramatically. Therefore, the simplest nodal network was used. The initial fluid conditions and wall temperature were set to the initial conditions from the experimental data. For this study, a non-computationally demanding method was warranted; therefore, to reduce the time for simulations, the two-phase pressure drop was ignored.

Table 4-2. Nodal geometry study

Number of Nodes		Average Temperature [ºC]	Time [s]
Nx	1	29.225	699.91
Nz	20		
Nx	3	29.102	1461.58
Nz	20		
Nx	5	29.703	1319.69
Nz	20		
Nx	5	29.203	2994.77
Nz	24		
Nx	1	28.793	1633.44
Nz	28		
Nx	5	-	> 7200
Nz	28		

4.2.2 Heat Load Input

One key modeling assumption was that the heat load is applied non-uniformly on the bottom of the cold plate. The ATTMO default is a uniform heat load that is achieved by creating a matrix that applies a heat load to each node on the bottom of the cold plate. In the current study, the heat load is localized to 1 mm in the center of the channels. Therefore, alterations to ATTMO's underlying code need to be completed to set the correct heat load boundary condition. For example, in this case 20 nodes were selected in the flow direction and one node perpendicular to the flow. For the current study, the heat exchanger has a localized heat load applied to the middle 1 mm of the 2 mm channel; therefore, nodes 6-15 in the flow direction have a heat load applied to them and nodes 1-5 and 16-20 are adiabatic. The nodal geometry is seen in Figure 4-11. Using "Overwrite
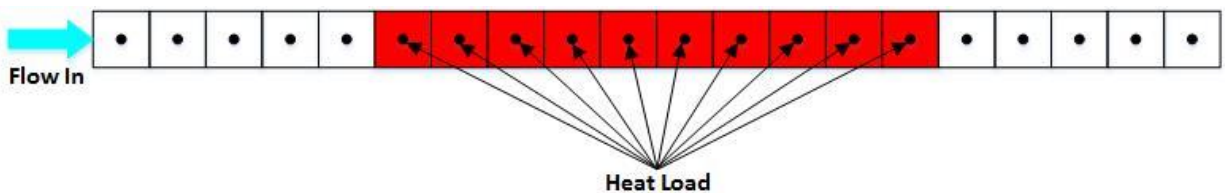
Figure 4-11. Heat load input to nodal geometry

Value" Simulink blocks, the script can be altered to apply the correct heat load, seen in Figure 4-12. Once the cold plate is configured to represent the current test section a time-dependent heat load is applied using Simulink blocks connected to the "Q (kW)" port (Figure 4-1).
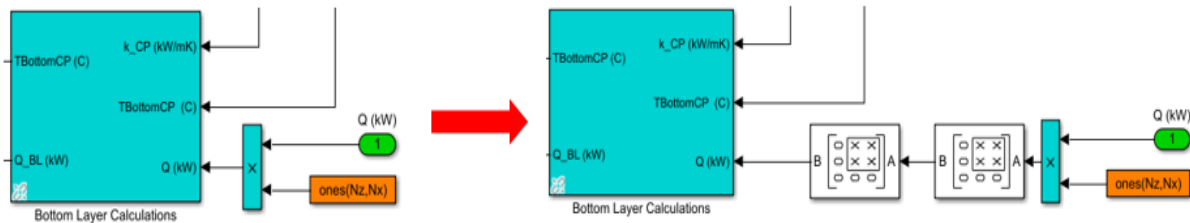
Figure 4-12. ATTMO with uniform heat load (left), ATTMO with non-uniform heat load (right)

4.2.3 Inlet and Outlet Fluid Conditions

To apply flow to the cold plate, two ATTMO generated blocks are used: Flow Generator and Flow Sink. The two blocks directly connect to the "Flow In" and "Flow Out" port on the cold plate, seen in Figure 4-13 below. The flow generator sets the inlet mass flow rate and temperature,
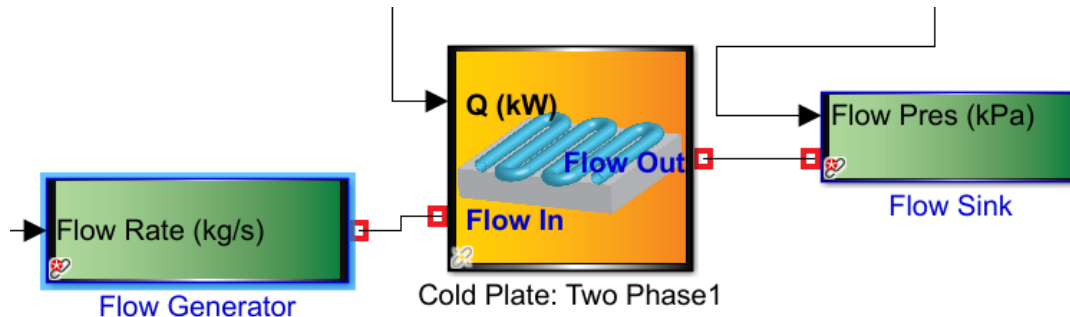
Figure 4-13. Inlet and outlet flow modules

and the flow sink sets the inlet pressure. Since pressure drop is ignored, the pressure sink at the outlet sets the fluid pressure for the entire cold plate. The GUI and input parameters for the Flow Generator block are shown in Figure 4-14. The fluid type is set to the working fluid used in the current study, R134a. The Flow Rate Time-Varying box is checked, which allows an additional input into the Flow Generator module to set a time-dependent user-defined flow rate. The flow rate data gathered from the experiments is imported into MATLAB as a mat file, which is then fed

into the Flow Generator block. The inlet temperature set in the GUI is taken from the upstream thermocouple. Previous studies have shown the heat loss from the upstream thermocouple to the inlet of the test section was negligible [9,65] and the temperature was set to the average temperature during the experiments.

The Flow Sink GUI sets the inlet time dependent pressure. The pressure values are entered into the Flow Sink using a mat file based on data from the inlet pressure transducer located upstream of the test section. The location upstream results in significant pressure drop as the fluid moves through the inlet restriction and into the channels. Considering this, the pressure from the hardware cannot be directly admitted into the model and the pressure drop must be calculated for
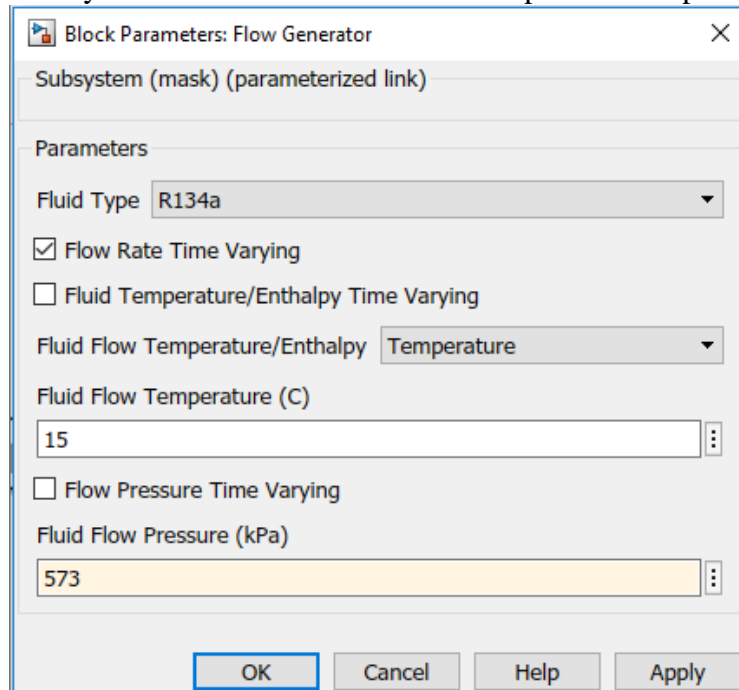
Figure 4-14. Flow generator GUI and parameters

inlet into the model. Figure 4-15 shows the major and minor loss that contribute to the pressure drop between the inlet and outlet pressure sensors. Point 19 marks the inlet pressure into the channels. To calculate the pressure at point 19, the pressure at the inlet and outlet were measured and then the calculated pressure losses were subtracted. The pressure losses were calculated by
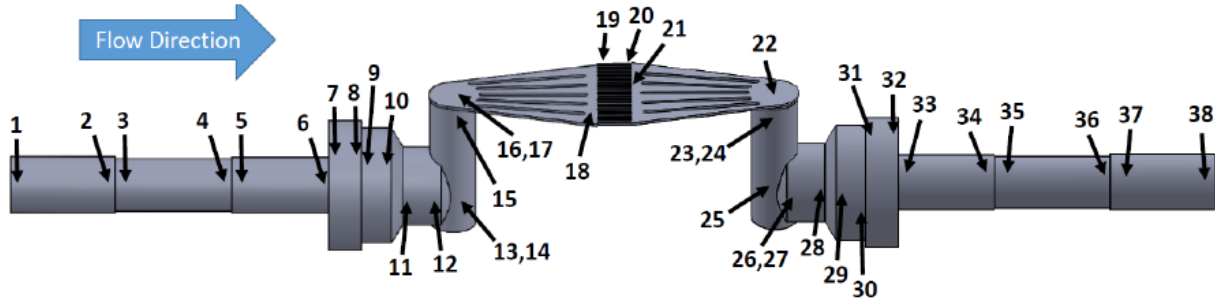
Figure 4-15. Flow path between inlet and outlet pressure transducers [65]

summing the major frictional losses and minor losses in each segment. Major pressure losses are

calculated using equation (4.31):

$$\Delta P_{major} = \frac{1}{2}\rho u^2 f \frac{L}{D_h} \qquad (4.31)$$

Where the friction factor can be found using equation (4.32), a correlation developed by Shah and

London for single-phase laminar flow [66].

$$f = \frac{96}{Re_l}(1-1.3553beta+1.9567beta^2-1.7012beta^3+0.9564beta^4-0.2537beta^5) \qquad (4.32)$$

Minor losses are calculated using equation (4.33):

$$\Delta P_{min} = \frac{1}{2}\rho u^2 K_{min} \qquad (4.33)$$

To overcome the unknown dimensions of the inlet restriction, the pressure drop from 1-18 and 19-

38 are calculated and subtracted from the overall pressure drop from hardware (equation (4.34)).

$$\Delta P_{orifice} = \Delta P_{1,38} - \Delta P_{1,18} - \Delta P_{19,38} \qquad (4.34)$$

Using the calculated pressure drop in the orifice, the inlet pressure to the channels was determined

with equation (4.35):

$$P_{channel,inlet} = P_{1,sensor} - \Delta P_{orifice} - \Delta P_{1,18} \qquad (4.35)$$

The pressure drop of the orifice calculated from single phase calculation was used to find the inlet pressure for the two-phase test.

4.2.4 Simulink Solver

Configuring the Simulink solver is imperative to arrive at a correct solution because slow solver steps can fail to capture dynamic changes and high steps will lead to undesired computation times. Amplifying these difficulties, the complex nature of ATTMO modules can cause Simulink to fail to converge if the correct model configuration parameters are not selected. For the current study, all model parameters were held constant independent of the case at hand. Figure 4-16 shows the GUI for the model configuration with the dedicated input. Under "Solver Options" two-mode
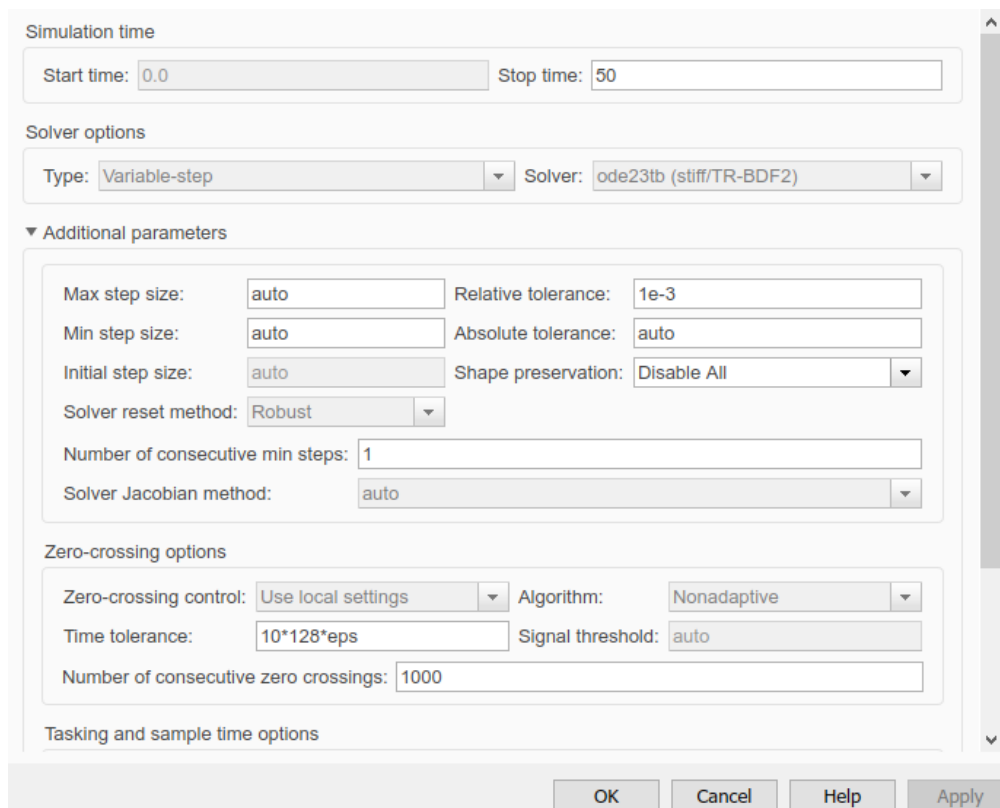
Figure 4-16. Model configuration settings

inputs are needed: "Type" and "Solver". "Type" is set to Variable-step which can dynamically adjust the time-step, decreasing the time-step during a discontinuity or increasing when steady-state is approaching or reached. This setting allows Simulink to arrive at a solution during a

60

dynamic change in heat load, while simultaneously decreasing computation time during steady-state conditions. For "Solver", ODE23tb (stiff/TR-BDF2) is chosen. ODE23tb is a variable-step continuous implicit solver, which is based on the trapezoid rule and second-order backward difference formula. When choosing a solver, MATLAB recommends the use of ODE 15 or 23 when using a variable-step stiff model [67]. The current study imposes sudden, dynamic, and large power loads where time constants will change rapidly, indicating a stiff model. From the various stiff solvers, PCKA recommends using ODE23tb. In "Additional parameters", all default settings are used except Solver reset method, which is changed from Fast to Robust. Solver reset method determines how the solver responds to a zero crossing or discontinuity. A robust setting specifies the solver to recompute the Jacobian matrix needed by the integration step at every solver reset [68]. The robust setting takes more computational time; however, in some cases using the fast solver reset method caused the simulation to fail to converge. To avoid any discrepancies between different simulations, the robust option was used for all simulations.

CHAPTER 5 RESULTS AND DISCUSSION

The preceding two chapters outlined the test facility and modeling approach. This chapter will present the experimental findings and augmented modeling approach for the transient temperature change when a pulsed heat load is applied. First, the pulsed heat load tests are presented. Since the temperature of the heater represents the diode temperature, it is imperative to understand the transient temperature fluctuations for efficient diode operation. The transient changes in flow conditions are discussed following the temperature measurements. Next, flow visualization under pulsed heat loads is shown. Flow visualization is used to understand the transients during a change in heat load. The temperature change to ramped heat loads is presented, and the results are compared to pulse heat loads. Finally, a novel modeling approach is suggested for the transient temperature change. The modeling approach is compared to experimental data.

5.1   Pulsed Heat Load

Pulse heat load tests were conducted to represent a cold start up on an electronic device. The average time-dependent temperature of the heater exposed to a pulsed heat load is shown in Figure 5-1. The heat is applied as a step function at time 0.5s to a maximum value of 43 Watts. The three trials show in Figure 5-1 were completed consecutively, once fluid conditions stabilized to initial nominal values. The heater temperature rises rapidly as the heat load is applied and reaches a maximum of ~70°C before dropping to steady-state conditions of 35°C. Similar results were documented in Huang et al study [35]. Their study documented a rise in wall temperature (maximum of ~ 80°C for 30 W cm^{-2}) until the ONB, which was followed by a drop in temperature to steady-state boiling (~40°C for 30 W cm^{-2}). The current study heat flux is ~14 times higher (380 W cm^{-2} vs 30 W cm^{-2}) than Huang et al. study and the peak temperature is 10°C lower. The lower

peak temperature is due to the increase in channels, lower hydraulic diameters, differences in fluid conditions, and a thicker floor used in this study. The extreme peak temperature seen before the ONB is thought to be attributed the high wettability of the fluid (R134a) and floor smoothness [34]. It is well known that boiling occurs in the pits and cavities on a surface, a fluid is highly wetting it fill the pits and cavities requiring higher temperatures for boiling incipience [7,20].
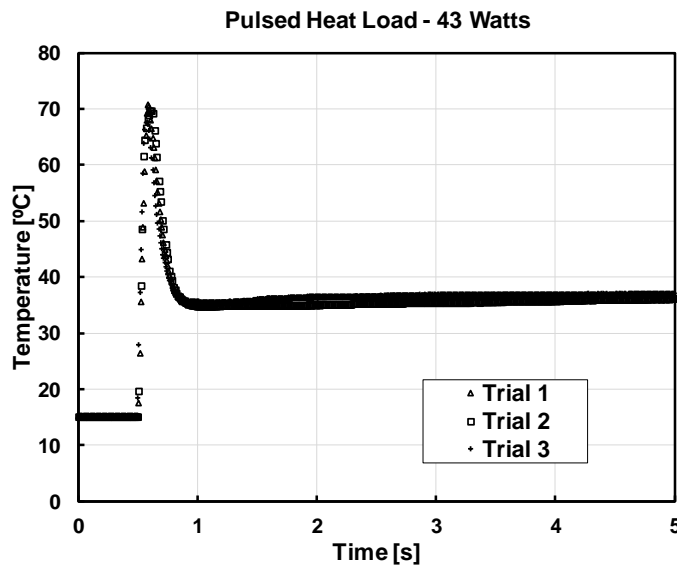
Figure 5-1. Average heater temperature for a pulsed heat load of 43 Watts

Similarly, if the surface is smooth and has little roughness higher temperature will be seen before ONB. Basu et al. study used HFE 7000 and attributed the wettability of the fluid to the high wall superheats to initiate boiling [34]. The wettability of R134a is likely filling the cavities, requiring higher wall superheats. Furthermore, Huang et al. performed experiment with a silicon channel that was manufactured with a deep reactive ion etching, similarly to the evaporator used in the current study [35]. In their study, the found the evaporator to have extremely smooth floor (90 nm) and they attributed the peak temperature to smoothness of the floor. The current study, likely has a smooth floor, causing peak temperatures. However, future investigation is needed to confirm the

63

root cause of the peak temperature. For trials 1, 2, and 3, the peak temperatures were 70.6°C, 69.6°C, and 67.7°C, showing strong repeatability in the results.

Flow visualization in the channels was performed to understand the two-phase flow dynamics and was plotted in reference to the time dependent temperature (Figure 5-2). For reference, single-phase steady-state flow is shown prior to a heat load (state 1). At the ONB (state 2), the fluid vaporizes in the inlet and outlet plenum, increasing the pressure of the system. Vaporization in the inlet plenum, marked by the red line in Figure 5-2(a), was unexpected,

(a)

(b)
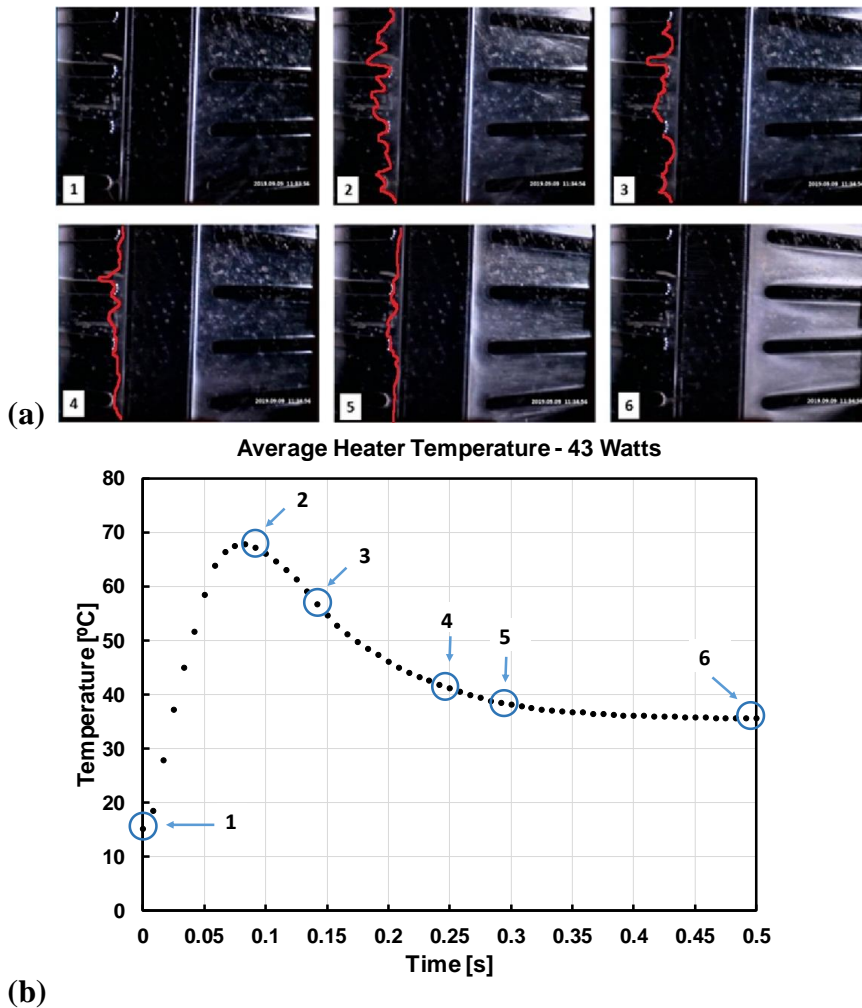
Figure 5-2. Images (a) and temperature (b) from a 43 Watt pulsed heat load. (1) Steady state single phase (2) Onset of boiling (3) 0.05 seconds after ONB (4) 0.15 seconds after ONB (5) 0.2 seconds after ONB (6) Steady State two-phase boiling

considering the inlet restriction, but can be explained by the radical increase in pressure at the ONB. This state is where the maximum temperature is plotted below in Figure 5-2(b). The large superheat temperature (~48°C) before the ONB provokes extremely rapid bubble growth at ONB, producing very high localized pressure in the channels. Kandlikar study the effects of wall superheat and rapid bubble generation in mircochannels [69]. Kandlikar showed increasing wall superheat leads to very rapid bubble generation leading to vapor backflow into the inlet. Additionally, Huang et al. also noticed vapor backflow at the ONB, with the presence of an inlet restrictor and attributed it to the rapid increase in fluid volume due to rapid bubble generation [35]. The increase in volume increases the pressure within the channel and the effects are exacerbated in the current study due to the small hydraulic diameters [69]. The localized pressure in the channels overcomes the inlet pressure, pushing vapor back through the inlet restriction. Although, the inlet restriction has been show to mitigate the effects of backflow, the extreme temperatures seen here are inducing very high localized pressure in the channel, which overcomes the inlet restrictor. The transients in vapor backflow were not reported in the studies conducted by Basu et al. and Chen and Cheng, even though higher heat fluxes and no inlet restriction was used, compared to the current study [60,70]. However, the hydraulic diameter in these studies are larger than the current study. The bubble confinement seen in the smaller channels is likely causing the bubble to elongate towards the inlet, pushing vapor past the inlet restriction.

From states 3-4 vapor is still present in the inlet plenum; however, vapor is moving back into the channels, which precipitates a gradual reduction in test section temperature, opposed to a sharp drop if no backflow occured. At state 5, the majority of vapor has left the inlet, and more two-phase flow is entering the outlet. At this point, the flow approaches steady-state boiling, and the change in temperature is decreasing. Finally, at point 6, no vapor is present at the inlet, and

65

steady-state two-phase boiling has been reached. The transient temperature due to a pulse heat load can be broken down into three different zones. The time between states 1 and 2 is sensible heating prior to nucleate boiling. States 2-6 are the evolution of two-phase boiling. In this zone, flow oscillations are occurring, partially suppressing the high heat transfer characteristics of two-phase flow and resulting in a gradual heater temperature decay. At state 6, flow oscillations are completely suppressed, and steady-state two-phase flow has been attained.

In addition to transient temperature changes, flow conditions also experience transients after the ONB. The ONB generates a pressure wave which opposes the flow and causes compressibility effects upstream of the test section. After the initial ONB pressure wave subsides, the mass flow rate increases to a new higher value (Figure 5-3(a)). Kingston et al. also documented these compressibility effects in their study on flow boiling instabilities [71]. Figure 5-3(b) details the transient inlet pressure and pressure drop measurements for this test. Following the heat load change, a steady increase in both inlet pressure and pressure drop is seen. The increase in pressure drop is due to an increase in frictional and acceleration losses that are inherent with two-phase flow. The steady increase in inlet pressure is initiated by the increased pressure drop in the test section and increased mass flow rate. The peak temperatures spikes and flow oscillations seen in pulsed heat load testing may be harmful to a device and potentially cause failure. Therefore, a potential mitigation strategy of ramping the heat load to minimize the effects of temperature overshoot and flow oscillations was investigated.
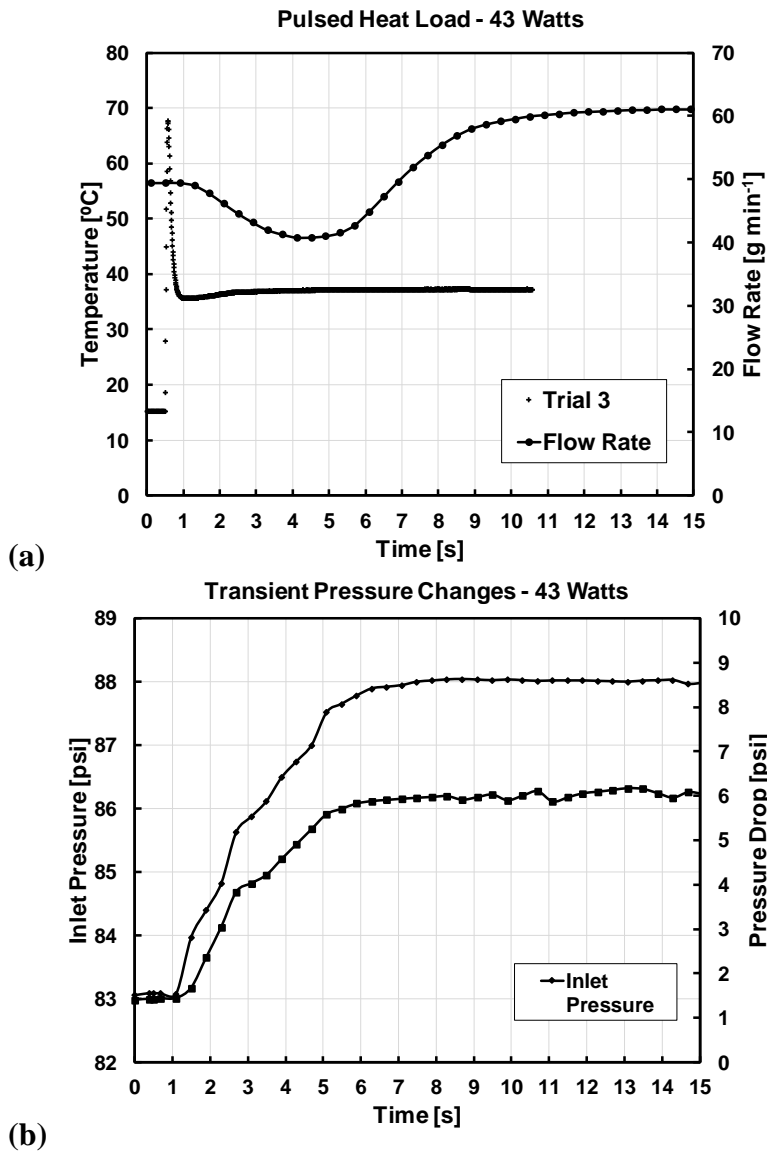
Figure 5-3. (a) Transient mass flow rate at 43 Watts pulsed heat load. (b) Transient pressure changes 43 Watts pulse heat load – trial 3

5.2   Ramping Heat Load

Ramping heat loads were tested to compare the transient effects of increasing the heat load for a given time interval against a pulse heat load (Figure 5-4 (a) and (b)). At time 0 s the heat load is initiated, either pulsed or ramped (50 W s^{-1}). The final steady-state heat load, in both cases, is 38 Watts. In the pulsed test the maximum peak temperature before the ONB was ~63ºC at time ~0.75s.

Using a ramped heat load, the maximum peak temperature can be reduced by up to 32ºC. In all cases the ONB was reached before the maximum heat load (38 Watts) was reached. In all the ramped cases the temperature of the heater increases to a maximum and is followed by a drop is temperature. The drop is temperature is associated with the ONB, similar to the results in the pulsed test. Additionally, the drop in temperature is much sharper in the ramped case compared to the pulsed heat load. Likely due to a decrease in vapor backflow, which will be discussed later on. In the ramped cases, boiling commences before the final heat load (38 Watts) is reached. The temperature drops after ONB, and rises again due to the increasing heat load. Once the heat load reaches 38 Watts the temperature stabilizes.

In Figure 5-4(b) the time and peak temperature are not consistent between the trials. The largest peak temperature seen was roughly 50°C, and the lowest temperature was 33°C. The discrepancy between trials is suspected to be a result of differences in trapped vapor in the nucleation cavities — more vapor entrapment results in lower ONB temperatures [72]. After boiling occurs in the test section vapor is likely trapped in the nucleation cavities [73]. Between the trials, subcooled liquid flows through the test section, which can cause the trapped vapor to condense or be removed [20]. As the quantity of vapor decreases the amount of superheat needed to necessitate boiling is increased. Heas et al. performed experiments studying the effects of transient heat loads in pool boiling [73]. In their study, they found the test section would need to

be "primed" before experiments were conducted to activate the nucleation cavities. If the test section was not primed, higher temperature were needed to activate boiling. In the current study, the time between runs could act to "un-prime" the test section, resulting in different ONB temperatures, due to different nucleation cavities being active.

(a)

(b)
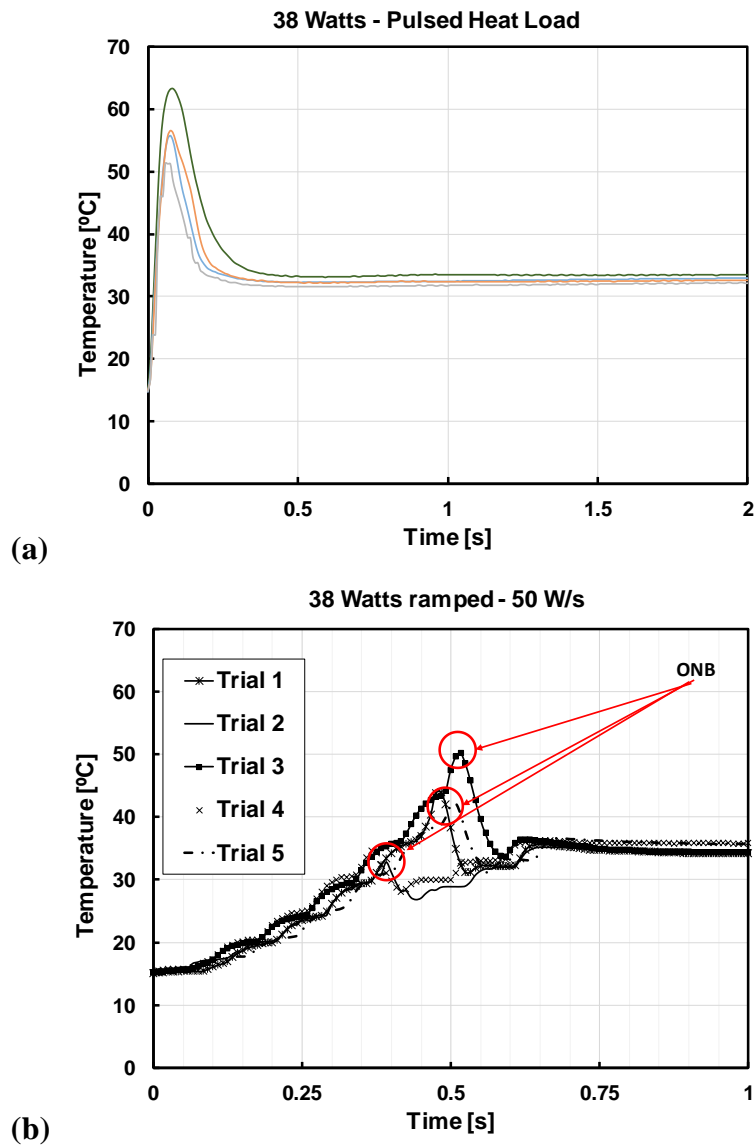
Figure 5-4. (a) Pulsed heat and ramped heat load – 38 Watts. (b) The ramped loads show stochastic ONB responses.

In addition, four different ramp rates (4, 9.5, 29, and 50 W s^{-1}) are compared to a pulsed heat load and the corresponding transient temperatures are plotted in Figure 5-5. In all cases, the heat load is initiated at time 0 s, at a specified ramp rate or pulse until a maximum heat load of 38 Watts is reached. For ramp rates 4, 9.5, and 29 W s^{-1} similar peak temperatures are reached at different times. The ONB temperature appears to have a superheat-heat flux threshold that is being met by each of these ramp rates. In the 50 W s^{-1} three different trials are plotted to show the variability as the ramp rate is increased. The variability in 50 W s^{-1} was not seen in the slower ramp rates. In
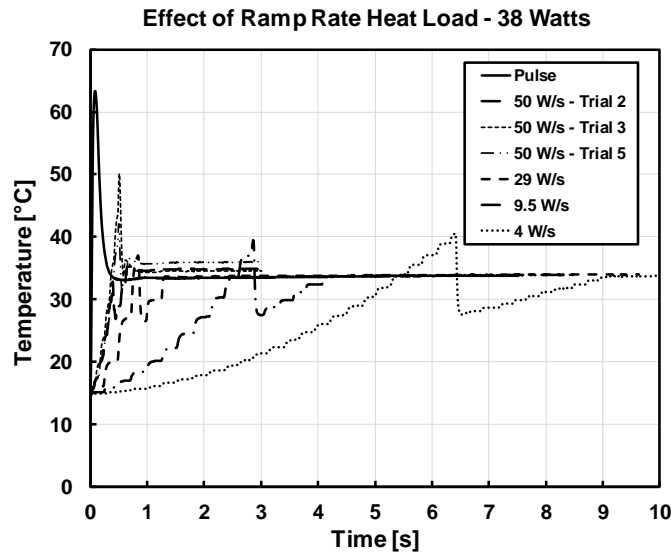
Figure 5-5. Test section temperature at a range of ramp rates and trials compared with a pulse at 38 W

Basu et al. study, they experienced a stochastic nature for ONB for at low heat fluxes [34]. The randomness was attributed to local variances in the heat temperature. Additionally, activation nucleation is inherently random due to different factors such as impurities in the fluid [20].

All the ramped cases, in Figure 5-5, were able to lower the peak temperature before the ONB compared to a pulsed heat load at the same nominal heat load. Hsu's work showed the range of active nucleation cavities is dependent on the thermal boundary layer, thermophysical properties,

bulk fluid temperature, and subcooling [26]. Hsu's work showed decreasing the thermal boundary layer would suppress ONB, necessitating high peak temperatures to trigger boiling. Given Hsu's results, the decrease in peak temperature for ramping versus pulsing is that the slower warming time allows time for a thermal boundary layer to grow allowing for lower ONB temperatures. Another possible reason for the ONB temperature decrease is the combination of temperature and heat flux needed to initiate boiling. With known boundary layer thickness and bulk fluid properties, the heat flux can be specified. Using this heat flux, correlations were developed for specific combinations of heat flux and wall temperature conditions for the onset of nucleate boiling [27–29]. These prior studies showed that ONB increases for increasing heat flux because the higher heat flux suppresses thermal boundary layer thickness, requiring higher wall superheats. Therefore, for slow ramping rates, the wall temperature-heat flux requirement is lower since the heat flux is lower. Additionally, the boundary layer has time to develop and not impede the nucleation process. However, these studies were completed by incrementally increasing the heat load, while maintaining inlet conditions. The current study does not occur at steady-state, while previous studies do. Therefore, further investigations are needed to confirm this. Figure 5-6 shows the flow visualization comparing a pulsed heat load (images 1-3) to a ramped test (4 W s^{-1}, images 4-6) for the same maximum heat load (38 Watts). Images 1 & 4 show differences in vapor backflow at ONB for the two test cases. The ramped test decreased the significance vapor backflow in the test section, likely due to lower wall superheat and less rapid bubble generation. The higher temperature in the pulsed case (63°C vs 40°C) prompts rapid vapor bubble growth in the channels at ONB, pushing large amounts of vapor into the inlet. In addition to the decreased backflow, the ramped tests allowed the system to reach steady-state two-phase boiling after ONB quicker than a pulsed heat load. In Figure 5-6, images 2 & 5 are one frame (0.05 s) after the ONB. In the ramped

71

heat test (image 2) most of the vapor has moved into the channels. In contrast, a significant amount of vapor is still present in the inlet plenum in the pulsed load test. In image 3 the ramped test reaches and steady-state two-phase boiling, while the pulsed heat test (image 6) still has some vapor in the inlet and steady-state has not been reached.
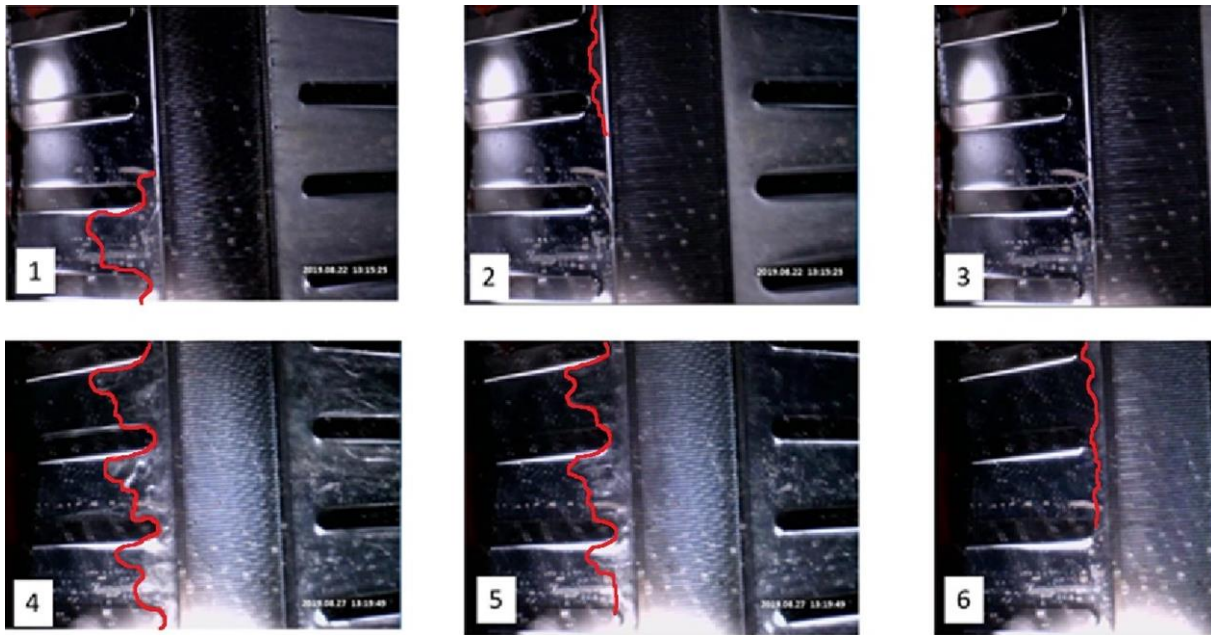
Figure 5-6. Images for ramped heat load 4 W/s (1-3) and pulsed heat load (4-6), for a maximum heat load of 38 Watts. (1) and (4) is ONB. Notice the absence of significant backflow in the ramped case.

The system level changes were investigated to help explain phenomena occurring in the channels. The pressure characteristics for the pulsed and ramped test are shown in Figure 5-7(a) and (b). In Figure 5-7, the heat pulse is activated at time of 0 s. In Figure 5-7(a), the inlet pressure spikes for 4 seconds, but is followed by a steady increase. The pressure drop immediately spikes,
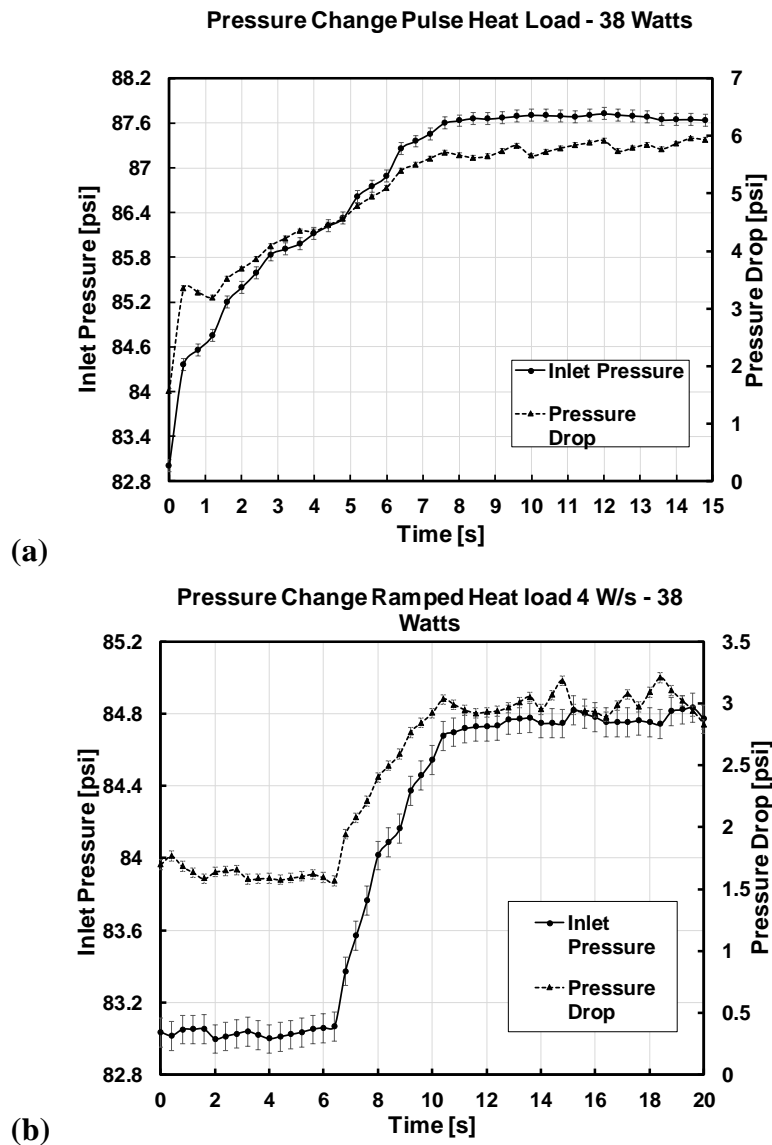
Figure 5-7. (a) Pressure change for a pulse heat load (38 Watts). (b) Pressure changes for a ramped heat load (4 W/s, 38 Watts).

which is followed by a slight decrease. This dynamic spike and drop is likely due to the vapor backflow at the ONB. Following the pressure decline, the pressure drop rises to a steady-state

73

value (6 psi). For the ramped heat test (Figure 5-7(b)), the inlet pressure and pressure drop steadily increase to a steady value after the ONB. The dynamic drop in inlet pressure after the ONB is not seen, which is likely due to decreased vapor backflow. The main difference between the two tests are the steady-state values. The steady-state value for the inlet pressure and pressure drop are higher in the pulsed test than the ramped test.

The mass flow rates, illustrated in Figure 5-8, help to explain the pressure dissimilarities. During the pulsed test, a drop in flow rate is initially seen. However, at 6 seconds the flow rate increases until a new steady-state is reached, approximately 60 g min^{-1}. For the ramped test, only a decrease is seen. After the ONB, the flow rate steadily drops until a lower steady-state is reached,

Flow Rate Pulse Heat Load & Ramped Test - 38 Watts
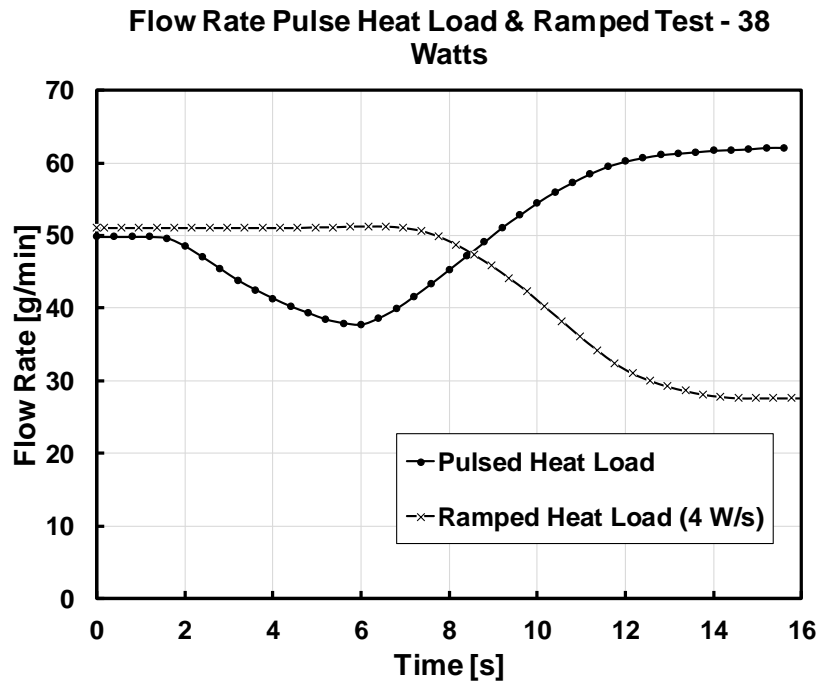
Figure 5-8. Transient flow rate for a pulsed heat load (38 Watts) and ramped heat load (4 W/s, 38 Watts)

just under 28 g min^{-1}. This trend was seen in all ramped tests. There is a delay in the flow rate drop in the ramped test due the long time before the ONB. An increase in flow rate is not seen in the

ramped case due to the decreased backflow, compared to the pulsed test. The amount of backflow in the ramped case was not large enough to cause any compressibility effects. Therefore, only a decrease in mass flow rate is seen due to an increase in pressure drop.

Ramping the heat load proved to be a viable option for decreasing the peak temperatures (up to 32°C) seen in the pulsed test. Additionally, the effects of vapor backflow and compressibility effects were damped in the ramped test. However, ramping the heat load in practice may not be a practical solution. Further work should focus on techniques to slowly reject the heat into the fluid, while also allowing the heat load to turn on quickly.

5.3 Dynamic Modeling Approach and Results

From the data collected in previous sections and in the literature, there is a need to model the transient temperature peak and drop when a pulsed heat load is applied. To the author's knowledge, no current modeling method is available. The study augments the modeling platform ATTMO. The succeeding sections outline a new correlation for the prediction of the onset of nucleate boiling for a pulsed heat load. Moreover, a method modeling the transient drop in temperature after ONB is presented. The new modeling methods are implemented into ATTMO, and the results are compared to experimental data, showing favorable comparison.

5.3.1 Onset of Nucleate Boiling

Currently, the ONB is predicted by correlations between the wall superheat temperature at a particular heat flux. Table 5-1 shows an example calculation for the current correlations for a 30 Watt heat load. Bergles and Rohsenow developed their correlation using a graphical technique using experimental data with water [27]. Sato and Matsumara model was generated between the bubble radius and thickness of thermal boundary layer [28]. In their study, data was used from previous investigators. Davis and Anderson modified and extended the work of Bergles and

Rohsenow [20,27]. Frost and Dzakowic modified Sato and Matsurmara correlation and checked with a wide variety of fluids (water, various hydrocarbons, mercury and cryogenic liquids) [20]. All the correlations were all derived from steady-state assumption, which may not extrapolate to transient experiments. Each study was conducted by slowly and incrementally increasing the heat load until boiling commenced. The correlations were not developed using microchannels, the smallest hydraulic diameter stated in the studies was 2387.6 µm, significantly larger than the channels used in this experiment (52 µm). Additionally, none of the correlations implemented an inlet restriction. Clearly, current correlations severely underpredict the ONB temperature seen in pulsed heat load experiments. In the worst case there is a 31.86°C under prediction for a 30 Watt

Table 5-1. Current ONB correlations

Correlations Investigated		Predicted T_{ONB} [°C]
Bergles & Rohsenow [27]	$q''_{ONB} = 5.30 * P^{1.156}[(T_w - T_{sat})_{ONB}]^{\frac{2.41}{P^{0.0234}}}$	20.14
Sato & Matsumura [28]	$q''_{ONB} = \dfrac{k_l h_{lv} \rho_v}{8\sigma T_{sat}}[(T_w - T_{sat})_{ONB}]^2$	25
Davis & Anderson [29]	$\begin{aligned}(T_w &- T_{sat})_{ONB} \\ &= \dfrac{\left(\dfrac{RT_{sat}^2}{h_{lv}}\right)ln(1 + \xi'')}{1 - \left(\dfrac{RT_{sat}^2}{h_{lv}}\right)ln(1 + \xi'')} \\ &+ \dfrac{q''_{ONB}y'}{k_l}\end{aligned}$	24.9
Davis & Anderson [20]	$q''_{ONB} = \dfrac{k_l h_{lv} \rho_v}{8\sigma T_{sat} C_\theta}[(T_w - T_{sat})_{ONB}]^2$	25
Frost & Dzakowic [20]	$q''_{ONB} = \dfrac{k_l h_{lv} \rho_v}{8\sigma T_{sat}}[(T_w - T_{sat})_{ONB}]^2 P_{r,l}^2$	21.6
ONB temperature from experiments: 44-52 [°C]		

pulse in the most extreme case (peak temperature 52°C), compared to the Bergles & Rohsenow correlation. Different arguments can be made to explain the discrepancy between the boiling correlations and the experimental data.

- Steady-state data was used to developed the correlations cannot be used in transient.

- Fluid properties of R134a necessitate higher temperatures for ONB.

- Roughness of channel floor is limiting nucleation cavities.

Under steady-state assumptions a fully developed thermal boundary layer is assumed, wherein the current study, the rapid application of heat does not allow a boundary layer to develop. Since the thermal boundary layer is not developed, the wall temperatures will increase before the onset of boiling [20]. Hsu study, showed experimentally, limiting the thermal boundary increases required wall superheat for ONB [26]. Fluid properties also playing a role in the high temperature seen. The fluid used in the current study (R134a) is a highly wetting fluid. In Basu et al. study that attributed the high wall temperature to the wettability of their fluid, HFE-7000 [70]. Additionally, in Huang et al. transient study, R236fa and R245fa are used, both refrigerants with high wettability [35]. In this study, high peak temperatures were seen before ONB (~40°C). However, the authors did not mention wettability as a source of the high temperature seen. The effects of floor roughness also play an important role. It is well known that nucleation occurs in the pits and cavities on the surface floor [7,20]. Therefore, if a surface is smooth, high wall superheats are needed for nucleation to occur. In the correlations developed above, no experiment uses a silicon channel, which was manufactured using a DRIE process. In Huang et al. study, a silicon channel etched with a DRIE process was used [35]. They attributed the high ONB temperature to the surface roughness of the floor (90 nm). The current study uses the same channel material and etching process; therefore, the roughness is likely contributing to the high temperatures.

It is also postulated that there is a thermal lag between the wall and fluid-wall interface, which may cause an increase in the measured temperature. To check this, the wall can be approximated as a semi-infinite solid. Using the Fourier number the thermal time constant was found, equation (5.1) below:

$$Fo = \frac{\alpha t}{L^2} \tag{5.1}$$

Where α is the thermal diffusivity, L is the length, and t is the time. The Fourier number is the ratio of conductive transport to the storage rate of the material. For a body to be considered a semi-infinite body, the Fourier number must be less than 0.2. Using the properties of silicon at 20 °C, the thickness of the wall, and a Fourier number of 0.2, the time constant was found to be 0.2 ms. The maximum temperature reached in the current study occurred at approximately 750 ms (Figure 5-1), so it is safe to neglect thermal lag in the reading. However, the exact cause of the higher temperature will require future work.
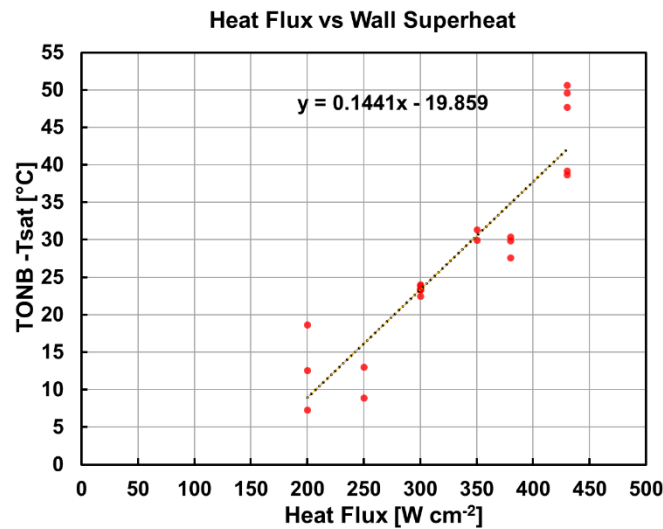
Figure 5-9. Heat flux and wall superheat requirement for ONB

A simple relationship was used to describe the heat flux and wall temperature for ONB. Figure 5-9 shows a linear relationship between the applied pulsed heat flux and the temperature

78

above the saturation temperature of the fluid before the ONB. There are several other factors which have been neglected, such as flow rate, subcooling, and wall thickness, however, the chart provides some initial information on the relationship between heat flux and ONB temperature for dynamic pulsed heat loads.

5.3.2   *Logistic Heat Transfer Coefficient Curve Fit*

As shown in section 5.1, the ONB was followed by dynamic flow instabilities, where vapor backflow occurred. These flow oscillations inhibited the high heat transfer characteristics of two-phase flow, causing a slow reduction in the test section temperature. Figure 5-10 shows the temperature profile from experiments plotted with the model where the heat transfer coefficient is switched to its two-phase value, using the Bertsch et al. correlation, after the ONB. For a 30 Watts pulsed heat load, the model shows an instantaneous decrease in the temperature if the HTC is directly switched to its two-phase value from 44°C to 29°C. However, the experimental data shows a lag in temperature, which takes approximately 0.06s from ONB to reach steady-state two-phase

Figure 5-10. Rapid switch to steady-state HTC

is boiling.   The lag is due to flow oscillations (Figure 5-2(a)), causing the HTC to gradually increase to the two-phase steady-state value. In Figure 5-2(a), vapor is pushing into the inlet likely

79

resulting in partial dryout in some channels. Partial dryout will lead to a low HTC, negating the benefits of two-phase boiling at lower qualities. Furthermore, the vapor excursion into the inlet 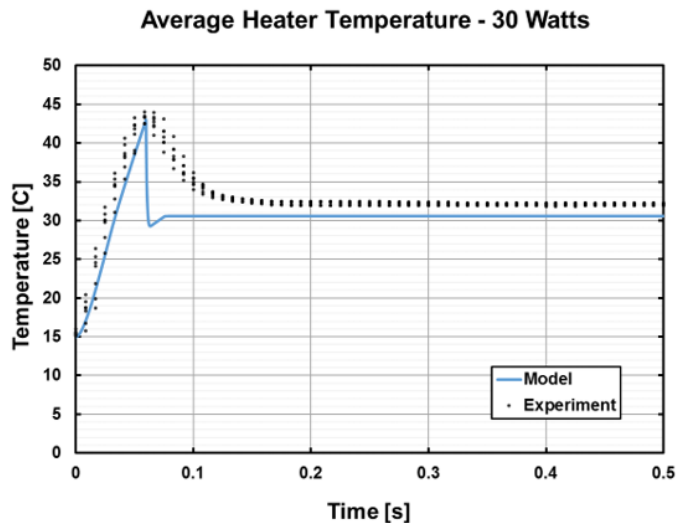plenum could be diminishing the benefits of the subcooled liquid entering the channels, causing a higher quality in the channels, resulting in a lower HTC. As the vapor is pushed back into the channels (Figure 5-2(a), images 3-5), the HTC will gradually increase. Finally, subcooled flow enters the channels (Figure 5-2(a), image 6), restoring the HTC to it steady-state value. In any case, the HTC changes after the ONB and a simple method to model these changes is warranted.

Using computationally demanding models to replicate the temperature decay, such as computational fluid dynamics, are unwarranted due to expensive processing power and long times to arrive at a solution. Furthermore, the tool should be applicable to system level studies. To provide a system level tool a logistic function is implemented into ATTMO to model the behavior. The logistic function, commonly referred to as a sigmoid curve, and is an S-shaped curve that exponentially grows or decays to a maximum or minimum value. The curve is typically used to describe the growth of a population to its capacity. This idea is used to describe an evolution of the HTC, from its steady-state single-phase value to its steady-state two-phase value. In the current study, the minimum value in the logistic function is the steady-state single-phase HTC. The function is used to exponentially grow the time-dependent HTC to its steady-state two-phase value (maximum). This is represented mathematically in equation (5.2):

$$ht(t)_{new,N} = \frac{ht(t)_{tp,N}}{1 + \dfrac{ht(t)_{tp,N} - ht(t)_{sp,N}}{ht(t)_{tp,N}} e^{-kt}} \tag{5.2}$$

Where $ht(t)_{tp,N}$ is the two-phase HTC at each time-step and node, $ht(t)_{sp,N}$ is the single-phase

HTC at each time step and node, k is the growth rate and $ht(t)_{new,N}$ is the newly calculated HTC.

The growth rate represents the rate at which the HTC is growing as flow oscillations are suppressed

within the channels. The curve fit is built into the ATTMO cold plate model. When performing

the calculations, the single-phase and two-phase HTC are separated and then placed into the

function which is used to find the heat load at each node. Figure 5-11 depicts the transient average
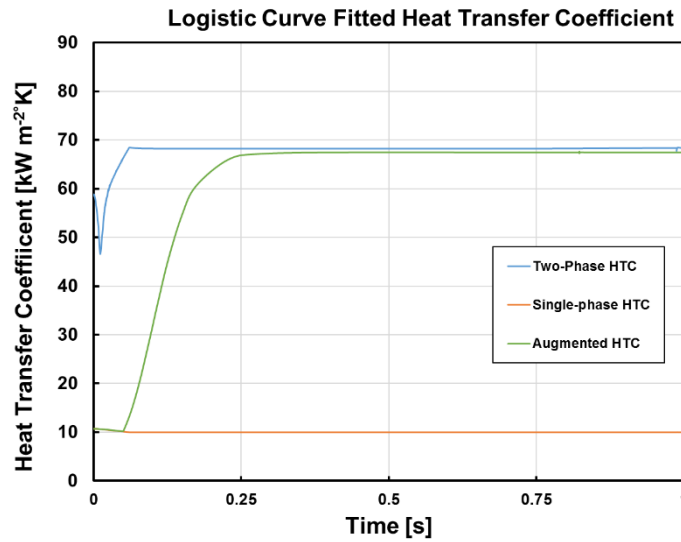
Figure 5-11. Transient single-phase, two-phase, and augmented HTC (30 Watts, growth rate 30)

HTC over the heater for single-phase, two-phase, and the augmented HTC. The two-phase HTC

initially drops due a change in heat load at the fluid wall interface. However, the two-phase HTC

is not used by the model at this time and the results are unaffected. The single-phase HTC is

roughly 10 kW m^{-2}K^{-1} and has minimal variability because the flow is laminar. The newly

incorporated HTC (Figure 5-10, augmented HTC) starts with a single-phase steady-state value.

After 0.05 seconds, the HTC exponentially approaches the steady-state two-phase value. At a time

just after 0.25 s the augmented HTC reaches its steady-state two-phase value. Figure 5-12 shows

the resulting temperature curve with the incorporated curve fit for a 30 Watt pulsed heat load. At

time 0 s the heat load is initiated in the model and experiment. The resulting model predicts the dynamic drop in temperature within an average 2.04°C before experimental data reached steady-state. The growth rate for Figure 5-12 was chosen based on trial and error to be 30. Increasing the growth rate caused the HTC to reach its two-phase value more rapidly, and conversely, decreasing the growth rate slowed the rate to reach the two-phase value. The correlation used in Figure 5-11 is from Bertsch et al. and it is clear that the HTC is being over predicted which causes a lower steady-state temperature. The temperature predicted by the model is 14% lower than the experimental data, which falls into the error bands stated by Bertsch et al. (28%). For the current study, a 14% error is considered satisfactory.
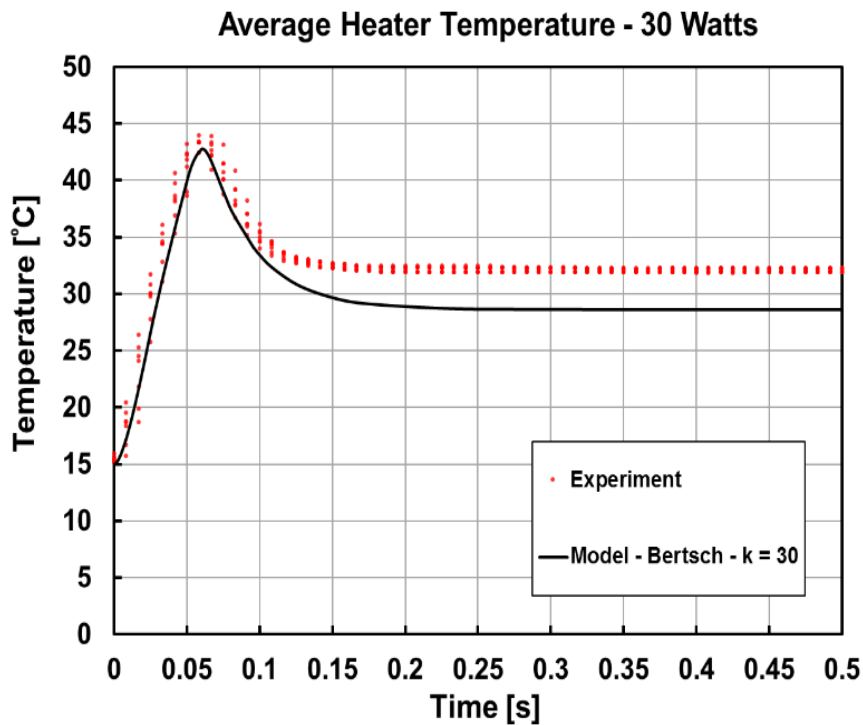
Figure 5-12. Logistic curve fit (30 Watts, growth rate 30)

Figure 5-13 shows the temperature profile for three different HTC (Agostini and Bontemps, Kim and Mudawar, and Bertsch et al.). Kim and Mudawar's correlation has similar results as Bertsch, where the HTC is over predicted. The Agostini and Bontemps correlation under predicts the HTC, which results in a higher steady-state temperature. The under predicted HTC (4.6°C lower temperature) using the Agostini and Bontemps correlation is different from Burk's study which predicted the temperature within 1.9°C [65]. The discrepancy between the two studies is likely due to the difference in channel geometries and the fundamental differences in solving method. Burk's worked focused on finite element analysis and the HTC was applied locally at each element in the channel. Burk's model had 11,803 elements, which likely increases the accuracy at the expense of computational demand. Here a simpler approach is taken, the HTC is only calculated at each of the twenty nodes and a fin efficiency is incorporated into the HTC calculation. These simplifications decrease accuracy but allow for rapid calculations.
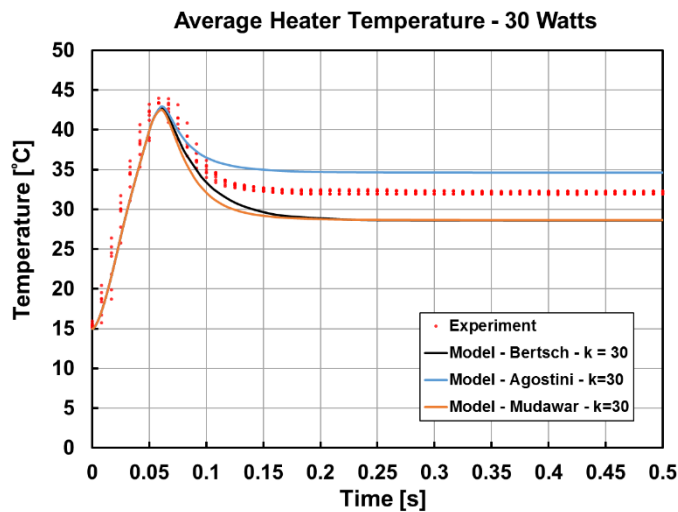
Figure 5-13. Comparison of two-phase HTC correlations

Figure 5-14 shows the relationship between the time for steady-state, growth rate constant, and the ONB temperature. In Figure 5-13, the red dots are from data collected from experiments, the blue dots is the growth rate which corresponded closely with the experimental data. Steady-
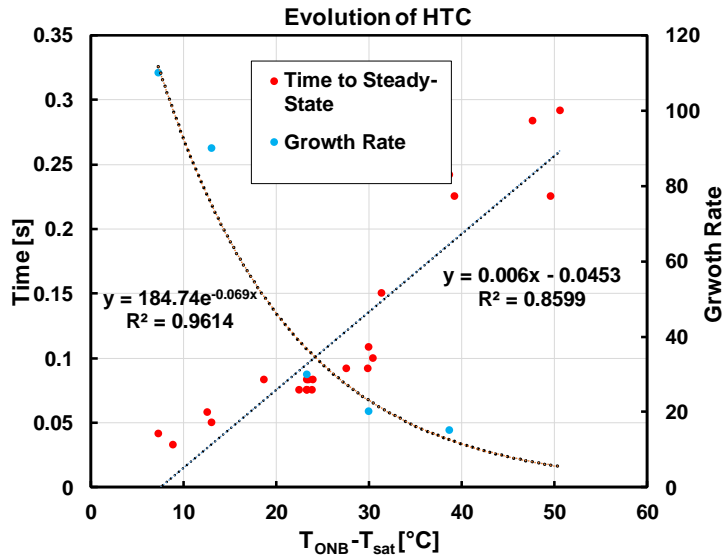
Figure 5-14. Evolution of HTC versus wall superheat. The blue dots represent the growth rate found in model, the red dots are experimental data.

state was assumed to be when the temperature change between readings was consistently less than 0.002°C. Growth rate was determined using ATTMO and fitting the model against the experimental data. A linear increase for time to steady-state and wall temperature was seen and resulted in an R-squared value of 0.8599. The trend has some stochastic nature, however, the upward trend is important where increasing heat flux will increase the amount of wall superheat. A more robust data set is needed to develop a stronger correlation. The growth rate decreased with increasing wall temperature. A lower growth rate indicates a longer time for the HTC to reach its steady-state two-phase value. This indicates that flow oscillations (i.e. HTC suppression) are exacerbated at higher wall superheat temperatures, which delays the time to reach fully developed two-phase boiling. Conversely, as the growth rate is increased, steady-state two-phase boiling is rapidly approached. For a wall superheat of ~7.5°C, the growth rate is set to 110 to accurately

84

predict the temperature decay, where a wall superheat of ~39°C results in a growth rate of 15. The growth rates recorded here are likely dependent on the current test section. A more robust data set will be needed to provide a correlation for growth rate. Future research will be needed to investigate other variables such as flow rate, inlet restriction size, and wall thickness, which may impact the results.

Additionally, the model was tested against a ramped heat load, and shown in Figure 5-15. At time 0 s the ramped heat load is initiated at 4 W s^{-1}, until a maximum power of 38 Watts is reached. A temperature threshold was set for the model to switch from a single-phase HTC to the fully developed two-phase HTC. The logistic function was not implemented in this case, due to the
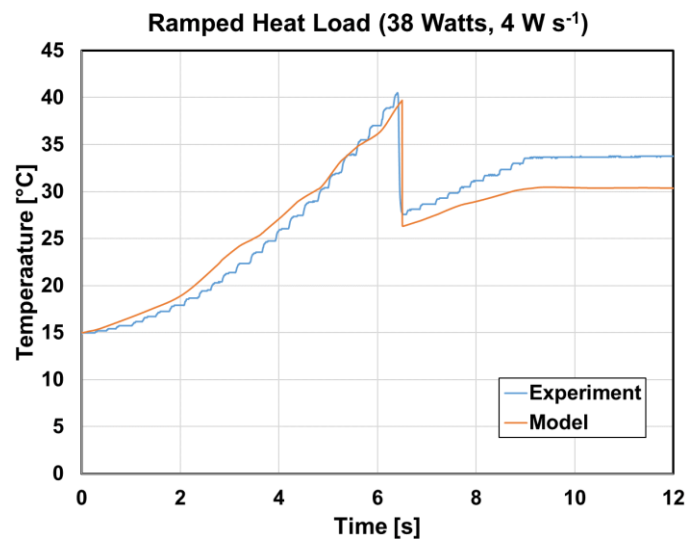
Figure 5-15. Model versus experimental data with ramped heat load. Logistic curve not implemented, hard switch to two-phase coefficient

decrease in back flow (Figure 5-6(b)) the HTC should rapidly approach its fully developed value. Unlike the pulsed case (Figure 5-6(a)), where oscillating flow suppressed the two-phase HTC. In Figure 5-14, the temperature of the model and experiment follow a similar trend until the maximum temperature ~40°C. In the experiments this marks the incipience of boiling, and a rapid reduction in temperature is seen to 27°C. With a hard switch to a fully developed two-phase HTC the

85

temperature in the model matches the experimental temperature drop. The drop is expected, due to a lower wall super heat (~7°C), which decreasing rapid bubble generation and backflow. However, the temperature drops below the experiment, this is due to the two-phase HTC (Bertsch et al.) over predicting the HTC. Both temperature steadily rise again, as the heat load has not reach 38 Watts and is still ramping. At roughly 9 s, the heat load has reached 38 Watts and both temperatures have reached a steady value.

CHAPTER 6 CONCLUSIONS AND RECOMMENDATIONS

The current study investigated the effects of transient heat loads on a multi-microchannel evaporator. Chapter 3 described in detail the test section and two-phase pumped loop used in the experiments. The test section was composed of 142 microchannels with hydraulic diameters of 52 µm, smaller than previous studies. Two types of heat loads were implemented: pulsed and ramped and data was collected to compare results. Chapter 4 discussed the modeling methods. A transient thermal suite (ATTMO), created by PCKA, connected Simulink with MATLAB scripts to perform transient calculations. Software changes were made within the model to replicate the test section, and hardware data from the experiments were imported into ATTMO. Chapter 5 presented the experimental findings and the results of the modeling efforts.

The results showed extreme peak temperatures before the ONB when the test section was exposed to a pulse heat load. After the ONB, a gradual reduction of the test section temperature occurred. The rate at which the test section reached a steady-state temperature was dependent on the magnitude of flow instabilities. Flow visualization showed vapor backflow into the inlet plenum, which was unexpected considering the inlet restriction. The findings of pulsed heat load show potential for device failure or damage. For example, laser diodes can rapidly pulse their optical output. If the frequency of the pulse does not reach the ONB, the test section temperature will not drop, leading to elevated operating temperatures. Furthermore, if the vapor backflow removes all liquid from the channels, burnout would occur. Burnout is detrimental because the diode temperature could rise dramatically, which has the potential to damage the device. Ramped heat loads showed the potential to mitigate the peak temperatures and vapor backflow seen in the pulsed experiments. By gradually warming the test section, peak temperatures 32°C less than the

ramped tests occurred. In addition, less backflow into the inlet plenum occurred, which would help avoid burnout. In actuality, laser events will need to be triggered immediately and rapidly; therefore, ramping the heat load is not a practical solution. However, the addition of a solid-liquid phase change material may act to absorb the initial heat pulse and slowly allow the heat to migrate into the fluid, essentially acting as a ramped heat load.

The experiments showed a need for a new non-computational demanding method to model the transient temperature. The relationship between the heat flux and ONB temperature appears to have a linear fit—as the heat flux is increased, the ONB temperature increases. A logistic curve fit was used to dynamically change the HTC as flow oscillations occur within the channels. The initial results show the modeling method predicts the dynamic temperature drop to within 2.06°C. The growth constant in the curve fit is dependent on the magnitude of flow oscillations and decreased with increased peak temperature. The modeling method can be used in future investigations to rapid model transient heat load at the system or heat sink level.

6.1   Future Recommendations

The current study demonstrated transient effects that potentially could cause catastrophic damage to the device. Only one test section geometry and one set of inlet conditions was investigated. This warrants future studies and continual research which may include the following:

- Mitigation of the peak temperature before the ONB should be investigated. Decreasing the amount of subcooling of the fluid entering the channels may prove a valuable solution. As the fluid conditions approach saturation, the amount of sensible heating will decrease. Additionally, if the test section has an inlet restriction, the decrease in subcooling may cause the fluid to flash as it exits the inlet restriction due to the rapid expansion into the channel. Since the fluid is boiling as it enters the channel, the peak temperature may be eliminated.

However, this would increase the outlet quality of the fluid, for a given heat load and the CHF may be reached at lower heat loads.

- Different test sections need to be evaluated in depth. For example, thicker test floors should be investigated. The additional thermal mass between the heater and the channels may aid in mitigating the peak temperature before ONB. Additionally, larger hydraulic diameters may reduce the amount of vapor backflow seen. As hydraulic diameters decrease, the vapor bubble is more confined, which can cause more vapor backflow. Although, additional thermal mass and large channel may lead to lower ONB temperature and less vapor backflow, an increase in thermal resistance will be seen. The increase in thermal resistance will likely lead to higher steady-state temperatures, which is not desired.

- Future work should investigate obtaining boiling as rapidly as possible, while maintaining lower ONB temperature. Different ramping schemes could potentially lower the ONB temperature and increase the time to max heat load. For example, in Figure 5-9 the ONB temperature as a function of heat flux is seen. At lower heat fluxes boiling can be initated at a lower temperature. A double pulse scheme can be used, meaning the heat is pulsed to a low heat load to initiate ONB (at a lower temperature) and once boiling is initiated pulsed to its higher value. If boiling has commenced, a large peak temperature may not be seen.

- Different system configurations should be also be analyzed. The magnitude of dynamic flow changes is likely system specific. If fluid inventory, pump characteristics, or system pressure drops change, the dynamic behavior might also change. Additionally, different closed loop cycles should be considered. For example, a vapor compression cycle (VCC) could be implemented. Using a VCC the fluid can easily enter the channels as two-phase,

89

limiting peak temperature. Also, without using a pump to circulate the fluid, the dynamic changes in flow rate may be mitigated.

- More studies are needed to investigate the physics behind the decrease in peak temperature by ramping the heat load. The decrease in boundary layer is likely suppressing the ONB, however, this cannot be confirmed. Range of active cavities size may also play a role in the ONB temperature. A more thorough study on this is needed.

- The model was only tested against one set of inlet conditions, one geometry, and a limited range of heat loads. The accuracy of the model at different conditions is unknown and the results may only be valid for the conditions simulated in this study. An inventory of data across a range of operating conditions will need to be collected and compared with the modeling.

- The model developed was program to switched based on a wall temperature threshold from Figure 5-9. However, the program needs to be developed to incorporate the heat flux as well. Due to challenges within the program, a solution was not able to be obtained if the heat flux was incorporated. Future work should focus on developing the model to meet a wall superheat and heat flux threshold requirement.

REFERENCES

[1]   2019, "Laser Diode" [Online]. Available: https://en.wikipedia.org/wiki/Laser_diode#Applications. [Accessed: 11-Apr-2019].

[2]   2019, "Laser Pumping" [Online]. Available: https://en.wikipedia.org/wiki/Laser_pumping. [Accessed: 11-Apr-2019].

[3]   Inc., F., "What Is a Semiconductor Laser Diode" [Online]. Available: https://www.fiberlabs.com/glossary/about-semiconductor-laser-diode/.

[4]   Liu, X., Zhao, W., Xiong, L., and Liu, H., 2015, *Packaging of High Power Semiconductor Lasers*, Springer, New York.

[5]   Treusch, H., and Pandey, R., 2011, "High-Power Diode Laser Arrays."

[6]   Matthias Pospiech, S. L., 2004, "Laser Diodes an Introduction."

[7]   Incropera, F. P., Dewitt, D. P., Bergman, T. L., and Lavine, A. S., 2011, *Fundamentals of Heat and Mass Transfer*, John Wiley & Sons.

[8]   Jin, Q., Wen, J., and Narayanan, S., "Analysis and Active Control of Pressure-Drop Flow Instabilities in Boiling Microchannel Systems."

[9]   Bevis, T., 2016, "High Heat Flux Phase Change Thermal Management of Laser Diode Arrays," Colorado State University.

[10]   "RP Photonic Encyclopedia" [Online]. Available: https://www.rp-photonics.com/modes_of_laser_operation.html. [Accessed: 01-Nov-2018].

[11]   "No Title" [Online]. Available: https://www.spilasers.com/industrial-fiber-lasers/redpower/what-is-a-continuous-wave-cw-laser/.

[12]   Rainbow, P., 2004, "High-Power Pulsed Laser Diodes Take on New Industrial and Commercial Applications," Photonics Spectra.

[13]   Skidmore, J. A., Freitas, B. L., Crawford, J., Satariano, J., Utterback, E., DiMercurio, L., Cutter, K., and Sutton, S., 2000, "Silicon Monolithic Microchannel-Cooled Laser Diode Array," Appl. Phys. Lett., **77**(10), pp. 10–12.

[14]   Mehendale, S. S., Jacob, A. M., and Shah, R., 2000, "Fluid Flow and Heat Transfer at Micro- and Meso-Scales with Application to Heat Exchanger Design," **53**(7).

[15]   Thome, J. R., 2004, "Boiling in Microchannels : A Review of Experiment and Theory," **25**, pp. 128–139.

[16]   Serizawa, A., Feng, Z., and Kawara, Z., 2002, "Two-Phase Flow in Microchannels," **26**, pp. 703–714.

[17]   Li, W., and Wu, Z., 2010, "A General Criterion for Evaporative Heat Transfer in Micro /

Mini-Channels," Int. J. Heat Mass Transf., **53**(9–10), pp. 1967–1976.

[18] Kew, P., and Cornwell, K., 1997, "Correlations for the Prediction of Boiling Heat Transfer in Small Diameter Channels," Appl. Therm. Eng., **17**, pp. 705–715.

[19] Triplett, K. A., Ghiaasiaan, S. M., Sadowski, D. L., and Abdel-Khalik, S., 1999, "Gas-Liquid Two-Phase ‾Ow in Microchannels Part I : Two-Phase ‾Ow Patterns," **25**, pp. 377–394.

[20] Carey, V. P., 1992, *Liquid-Vapor Phase-Change Phenomena*, Hemisphere Publishing corporation.

[21] Kandlikar, S., 2003, "Heat Transfer Mechanisms during Flow Boiling in Microchannels.Pdf," *First Internation Conference on Microchannels and Minichannels*, Rochester.

[22] Cornwell, K., and Kew, P., 1993, "Boiling in Small Parallel Channels," Energy Effic. Process Technol., pp. 624–638.

[23] Mirmanto, M., and Karayiannis, T., 2012, "FLOW PATTERNS AND HEAT TRANSFER MEASUREMENTS FOR FLOW BOILING FLOW PATTERNS AND HEAT TRANSFER MEASUREMENTS FOR FLOW," (June 2015).

[24] Revellin, R., and Thome, J., 2007, "A New Type of Diabatic Flow Pattern Map for Boiling Heat Transfer in Microchannels," J. Micromechanics Meas., **17**, pp. 788–796.

[25] Clark, H. B., Strenge, P. ., and Westwater, J. ., 1959, "Active Sites for Nucleate Boiling," Chem Eng., **55**(29).

[26] Hsu, Y. Y., 1962, "On the Size Range of Active Nucleation Cavities on a Heating Surface," J. Heat Transfer, **84**(3), p. 207.

[27] Bergles, A. E., and Rohsenow, W. ., 1964, "The Detemination of Forced-Convection Surface-Boiling Heat Transfer," **86**(3), pp. 365–372.

[28] Sato, T., and Matsumura, H., 1964, "On the Conditions of Incipient Subcooled-Boiling with Forced Convection," Mech. Eng. J., **7**(26).

[29] Davis, E. J., and Anderson, G. H., 1966, "The Incipience of Nucleate Boiling in Forced Convection Flow," AIChE J., **12**(4), pp. 774–780.

[30] Deng, D., Tang, Y., Liang, D., He, H., and Song, Y., 2014, "Flow Boiling Characteristics in Porous Heat Sink with Reentrant Microchannels," Int. J. Heat Mass Transf., **70**, pp. 463–477.

[31] Kuo, C., and Peles, Y., 2007, "Local Measurement of Flow Boiling in Structured Surface Microchannels," Int. J. Heat Mass Transf., **50**, pp. 4513–4526.

[32] Ammerman, C. ., and You, S. ., 2001, "Enhancing Small-Channel Convective Boiling Performance Using a Microporous Surface," ASME, **123**, pp. 976–983.

[33] Wang, H., and Peterson, R. B., 2010, "Enhanced Boiling Heat Transfer in Parallel Microchannels with Diffusion Brazed Wire Mesh," IEEE Trans. Components Packag. Technol., **33**(4), pp. 784–793.

[34] Basu, S., Werneke, B., Peles, Y., and Jensen, M. K., 2015, "Transient Microscale Flow Boiling Heat Transfer Characteristics of HFE-7000," Int. J. Heat Mass Transf., **90**, pp. 396–405.

[35] Huang, H., Borhani, N., and Thome, J. R., 2018, "Thermal Response of Multi-Microchannel Evaporators During Flow Boiling of Refrigerants Under Transient Heat Loads With Flow Visualization," **138**(September 2016), pp. 1–13.

[36] Prajapati, Y. K., and Bhandari, P., 2017, "Flow Boiling Instabilities in Microchannels and Their Promising Solutions – A Review," Exp. Therm. Fluid Sci., **88**(July), pp. 576–593.

[37] Zhang, T., Tong, T., Chang, J., Peles, Y., Prasher, R., Jensen, M. K., Wen, J. T., and Phelan, P., 2009, "Ledinegg Instability in Microchannels," Int. J. Heat Mass Transf., **52**(25–26), pp. 5661–5674.

[38] Boure, J. ., Bergles, A. ., and Tong, L. S., 1973, "REVIEW OF TWO-PHASE FLOW INSTABILITY," Nucl. Eng. Des., **25**, pp. 165–192.

[39] Qu, W., and Mudawar, I., 2004, "Measurement and Correlation of Critical Heat Flux in Twophase Microchannel Heat Sinks," Int. J. Heat Mass Transf., **47**, pp. 2045–2059.

[40] Bergles, A. E., and Kandlikar, S., 2005, "On the Nature of Critical Heat Flux in Microchannels," **127**, pp. 101–107.

[41] Revellin, R., and Thome, J. R., 2008, "A Theoretical Model for the Prediction of the Critical Heat Flux in Heated Microchannels," Int. J. Heat Mass Transf., **51**, pp. 1216–1225.

[42] Brutin, D., "Flow Boiling Instability."

[43] Kakac, S., and Bon, B., 2008, "A Review of Two Phase Flow Dynamic Instabilities in Tube Boiling Systems," Int. J. Heat Mass Transf., **51**, pp. 399–433.

[44] Brutin, D., Topin, F., and Tadrist, L., 2003, "Experimental Study of Unsteady Convective Boiling in Heated Minichannels," **46**, pp. 2957–2965.

[45] Xu, J., Zhou, J., and Gan, Y., 2005, "Static and Dynamic Flow Instability of a Parallel Microchannel Heat Sink at High Heat Fluxes," Energy Convers. Manag., **46**, pp. 313–334.

[46] Guodong, W., Cheng, P., and Wu, H., 2007, "Unstable and Stable Flow Boiling in Parallel Microchannels and in a Single Microchannel," Int. J. Heat Mass Transf., **50**, pp. 4297–4310.

[47] Kosar, A., Kuo, C.-J., and Peles, Y., 2006, "Suppression of Boiling Flow Oscillations in Parallel Microchannels by Inlet," J. Heat Transfer, **128**(March 2006), pp. 251–260.

[48] Wang, G., Cheng, P., and Bergles, A. E., 2008, "Effects of Inlet / Outlet Configurations on Flow Boiling Instability in Parallel Microchannels," Int. J. Heat Mass Transf., **51**, pp. 2267–2281.

[49] Kuo, C., and Peles, Y., 2009, "Pressure Effects on Flow Boiling Instabilities in Parallel Microchannels," Int. J. Heat Mass Transf., **52**(1–2), pp. 271–280.

[50] Kuo, C., and Peles, Y., 2008, "Flow Boiling Instabilities in Microchannels and Means for Mitigation by Reentrant Cavities," J. Heat Transfer, **130**.

[51] Kim, S., and Mudawar, I., 2013, "Universal Approach to Predicting Saturated Flow Boiling Heat Transfer in Mini / Micro-Channels – Part I . Dryout Incipience Quality," Int. J. Heat Mass Transf., **64**, pp. 1226–1238.

[52] Kim, S., and Mudawar, I., 2013, "Universal Approach to Predicting Saturated Flow Boiling Heat Transfer in Mini / Micro-Channels – Part II . Two-Phase Heat Transfer Coefficient," Int. J. Heat Mass Transf., **64**, pp. 1239–1256.

[53] Bertsch, S. S., Groll, E. A., and Garimella, S. V., 2009, "A Composite Heat Transfer Correlation for Saturated Flow Boiling in Small Channels," Int. J. Heat Mass Transf., **52**, pp. 2110–2118.

[54] Ducoulombier, M., Colasson, S., Bonjour, J., and Haberschill, P., 2001, "Carbon Dioxide Flow Boiling in a Single Microchannel - Part II: Heat Transfer," Exp. Therm. Fluid Sci., **35**, pp. 597–611.

[55] Tran, T. N., Wambsganss, M. W., and France, D. M., 1996, "Small Circular and Rectangular Channel Boiling with Two Refrigerants," Int. J. Multiph. Flow, **22**(3), pp. 485–498.

[56] Lazarek, G. M., and Black, S. H., 1982, "EVAPORATIVE HEAT TRANSFER , PRESSURE DROP AND CRITICAL HEAT FLUX IN A SMALL VERTICAL TUBE WITH R-l 13," Int. J. Heat Mass Transf., **25**(7), pp. 945–960.

[57] Yu, W., France, D. M., Wambsganss, M. ., and Hull, J. ., 2002, "Two-Phase Pressure Drop , Boiling Heat Transfer , and Critical Heat Flux to Water in a Small-Diameter Horizontal Tube," Int. J. Multiph. Flow, **28**, pp. 927–941.

[58] Warrier, G. R., Dhir, V. K., and Momoda, L. A., 2002, "Heat Transfer and Pressure Drop in Narrow Rectangular Channels," Exp. Therm. Fluid Sci., **26**, pp. 53–64.

[59] Agostini, B., and Bontemps, A., 2005, "Vertical Flow Boiling of Refrigerant R134a in Small Channels," Int. J. Heat Mass Transf., **26**, pp. 296–306.

[60] Chen, G., and Cheng, P., 2009, "Nucleate and Film Boiling on a Microheater under Pulse Heating in a Microchannel," Int. Commun. Heat Mass Transf., **36**(391–396).

[61] Lamaison, N., Marcinichen, J. B., Ong, C. L., and Thome, J. R., 2016, "Two-Phase Mini-Thermosyphon Electronics Cooling , Part 3 : Transient Modeling and Experimental Validation," 2016 15th IEEE Intersoc. Conf. Therm. Thermomechanical Phenom. Electron. Syst., pp. 589–598.

[62] Hodson, S., McCarthy, K., McCarthy, P., and Issam, M., 2019, "A Dynamic Two-Phase Component Model Library for High Heat Flux Applications," SAE Int., pp. 1–11.

[63] "Deep Reactive-Ion Etching" [Online]. Available: https://en.m.wikipedia.org/wiki/Deep_reactive-ion_etching.

[64] "DRIE Bosch Process" [Online]. Available: https://en.m.wikipedia.org/wiki/File:DRIE_Bosch_process.png.

[65] Burk, B. E., 2018, "A Computational Examination of Conjugate Heat Transfer During Microchannel Flow Boiling Using Finite Element Analysis," Colorado State University.

[66] Shah, R., and London, A., 1978, *Laminar Flow Forced Convection in Ducts: A Source Book for Compact Heat Exchanger Analytical Data*, Academic Press, New York, NY.

[67] The MathWorks, I., "Choose a Solver" [Online]. Available: https://www.mathworks.com/help/simulink/ug/types-of-solvers.html.

[68] The MathWorks, I., "Solver Reset Method" [Online]. Available: https://www.mathworks.com/help/simulink/gui/solver-reset-method.html.

[69] Kandlikar, S. G., 2006, "Nucleation Characteristics and Stability Considerations during Flow Boiling in Microchannels," **30**, pp. 441–447.

[70] Basu, S., Werneke, B., Peles, Y., and Jensen, M. K., 2015, "Thermal Behavior of a Microdevice under Transient Heat Loads," Int. J. Heat Mass Transf., **91**, pp. 1078–1087.

[71] Kingston, T., Weibel, J., and Garimella, S. V., 2018, "High-Frequency Thermal-Fluidic Characterization of Dynamic Microchannel Flow Boiling Instabilities: Part1– Rapid-Bubble-Growth Instability at the Onset of Boiling," Int. J. Multiph. Flow, **106**, pp. 179–188.

[72] Jo, H., Seon, H., Kang, S., and Hwan, M., 2011, "A Study of Nucleate Boiling Heat Transfer on Hydrophilic , Hydrophobic and Heterogeneous Wetting Surfaces," Int. J. Heat Mass Transf., **54**(25–26), pp. 5643–5652.

[73] Heas, S., Robidou, H., Raynaud, M., and Lallemand, M., 2003, "Onset of Transient Nucleate Boiling from a Thick Flat Sample," Int. J. Heat Mass Transf., **46**, pp. 355–365.

APPENDIX A   EXPERIMENTAL FACILITY

A.1.   Facility Components

This chapter details the experimental facility used in this current study. All fittings and components in the facility are shown in detail. Tables A-1 details the components used in the facility. Figure A-1 is a detailed schematic of the facility.

Table A-1. Parts and instruments list for two-phase pumped loop used in experiments

| Part	Description	Manufacturer	Supplier	Part Number
Gear Pump Head	GA series	MicroPump	Cole-Parmer	GA-T32
Gear Pump Console Drive	50-5000 rpm	MicroPump	Cole-Parmer	wu-75211-10
Accumulator	Air/Water Bladder Cylinder	Accumulators inc		AI-1QT-3KT
Microscopic Camera	Digital microscope	Dino-lite	Dino-lite	AAM7915MZT
IR Camera	thermoImager TIM 160 with 23º lens	Micro- Epsilon		N/A
Chiller	Merlin M150LR	Thermofisher		M150LR-CP55
Heat Exchanger	Compact Plate Heat Exchanger	Koolance		HXP-193
Flow Meter	Coriolis Flow Meter Coriolis flow transmitter	Rheonik		RHM015 RHE07
Power Supply	DC Programmable Power Supply	Agilent	Keysight	N8735A
Shunt Resistor	0.1 ohm < 0.01%	Omega		PX409-100DWUI
Thermocouples	Type K Type T	Omega		TC-K-NPT-UG-72 TC-T-NPT-UG-72
Pressure Transducers	0-50psia 0-100psia 50 psid	Omega		PX409-005AI MMA100C1P3C0T4A6 PX409-100DWUI
Data Acquisition System	4-slot USB Chassis Thermocouple module; 16ch Analog current and voltage Analog voltage	National Instruments		cDAQ-9174 NI 9214 NI 9207 NI 9221
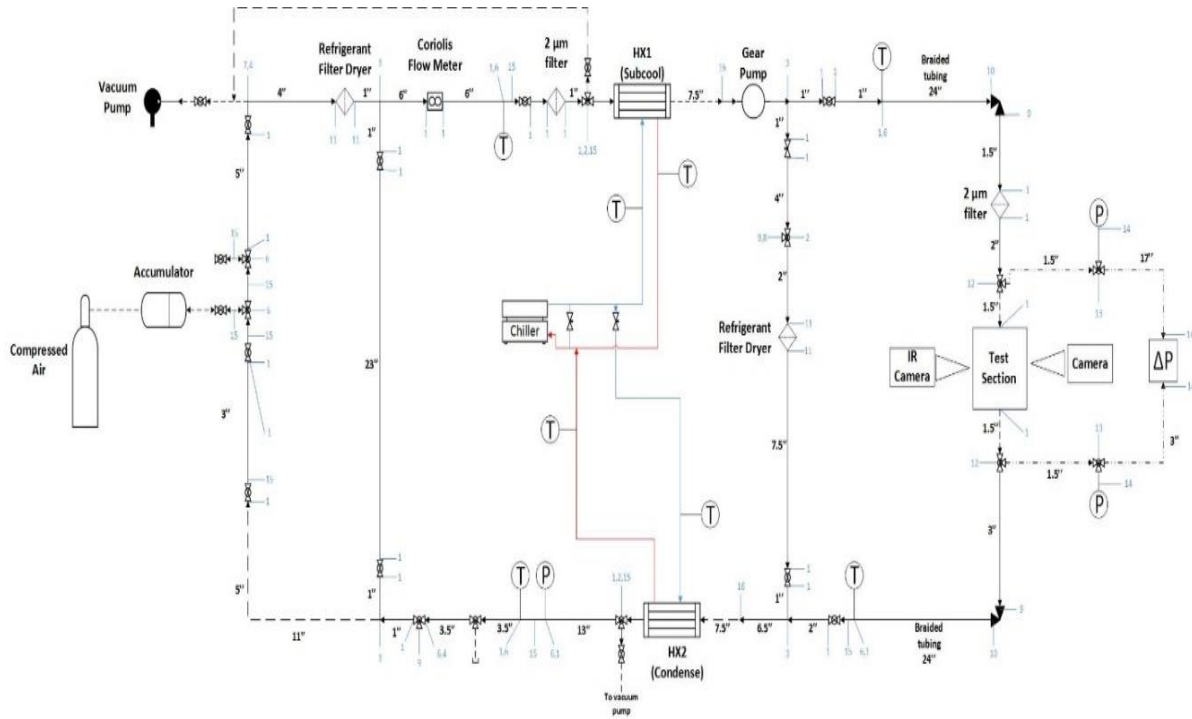
Figure A-1. Detailed schematic of facility

A.2.   Infrared Camera Calibration

To ensure temperature measurements collected by the infrared camera are accurate, in-house calibration is performed. A high emissivity black paint, used in the experiments, was painted
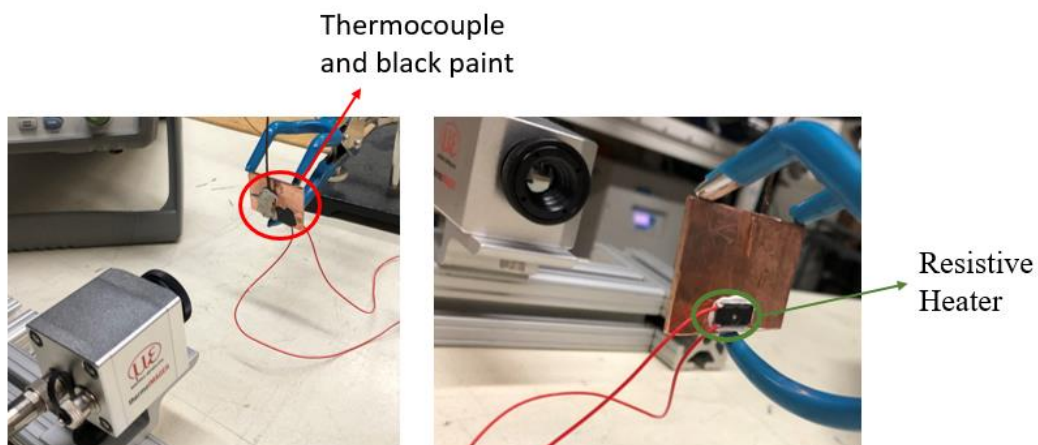

Figure A-2. IR camera calibration setup

onto a surrogate test piece made of copper. A surface thermocouple calibrated using a high accuracy Fluke reference probe (±0.001ºC), is placed next to the high emissivity paint on the copper test piece. The IR camera was positioned at a working distance of 4 inches, similar to the experiments. A resistive heater was placed on the back of the surrogate test piece to increase its temperature, seen in Figure A-2. Two trials were conducted, and over 100 data points were collected over a range of temperature from 22 – 60 ºC for each trial. The average temperature readings by the IR camera over the high emissivity paint and thermocouple were recorded, and the results are seen in Figure A-3. The accuracy of the IR camera from the calibration process increased from the manufacturer specified of ±2ºC to ±0.2ºC.
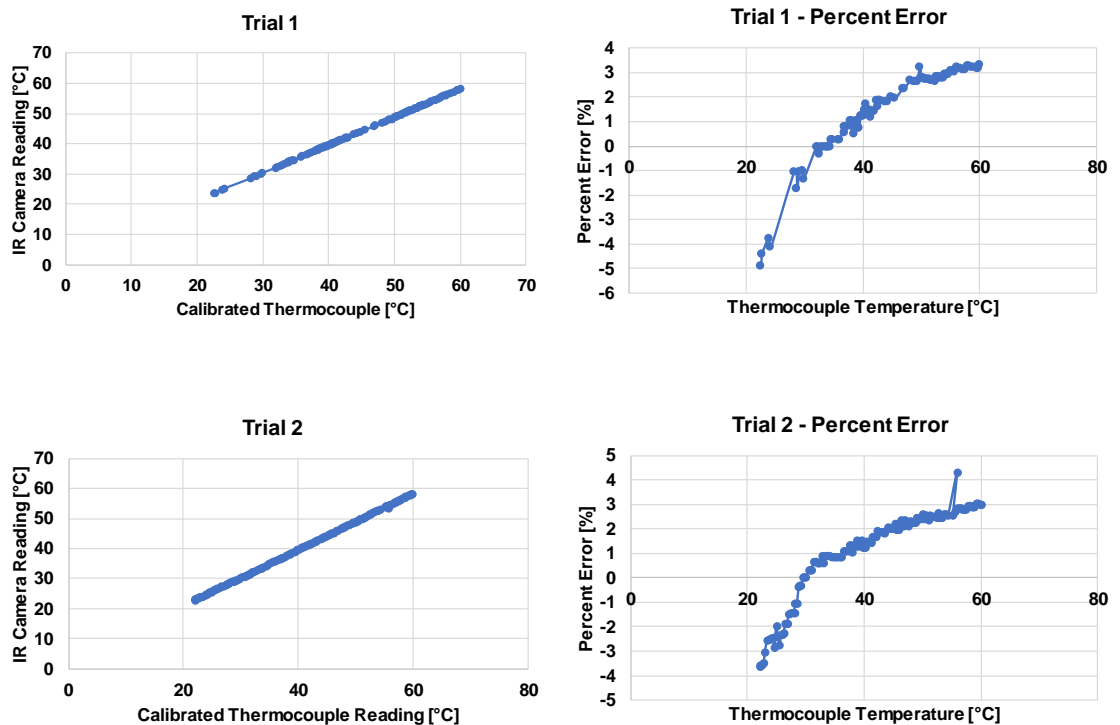
Figure A-3. IR calibration results

APPENDIX B   HAND CALCULATIONS

Heat transfer coefficients were programmed into ATTMO. To ensure these equations were properly performed within ATTMO, hand calculations were completed using Engineering Equation Solver. Equation inputs were taken from ATTMO, and a single node during steady-state was used to compare. Tables B-1 and B-2 shows the results from the calculations.

Table B-1. Bertsch et al. correlation hand calculations

	Bertsch et al.			
Parameter	**Equation**	**ATTMO Value**	**Hand Calculation Value**	**Units**
Inputs	μ_l= 2.0719e-4 kg m^{-1}s^{-1} μ_v= 1.1491e-5 kg m^{-1}s^{-1} ρ_l= 1225.1 kg m^{-3} ρ_v= 28.84 kg m^{-3} σ=0.0087 N m^{-1} k_l= 8325.5e-5 W m^{-2}K^{-1} k_v= 1334.1e-5 W m^{-2}K^{-1} x =0.139 M = 102 kg kmol^{-1} Rp=1 L = 1e-4 m D_h= 5.2174e-5 m q'' =121285.1 W m^{-2} P_r= 0.1412 P_l= 3.4969 P_v =0.8622 g = 9.81 m s^{-2} G=972.2 kg m^{-2} s^{-1}			
Re_v	$$\frac{GD_h x}{\mu_v}$$	613.55	613.6	-
Re_l	$$\frac{GD_h(1-x)}{\mu_v}$$	210.79	210.8	-
Co	$$\frac{1}{D_h}\sqrt{\frac{\sigma}{g(\rho_l-\rho_v)}}$$	16.48	16.5	-
S	$(1-x)$	0.861	0.861	-
F	$1+80(x^2-x^6)e^{-0.6Co}$	1	1	-
ht_{NB}	$55P_r^{0.12-0.2\log_{10}R_P}(-\log_{10}P_r)^{-0.55}M^{-0.5}(q'')^{0.67}$	11992.99	11994	W m^{-2} K^{-1}
$ht_{conv,l}$	$$\left(3.66+\frac{0.668\frac{D_h}{L}\text{Re}_l\,\text{Pr}}{1+0.04\left[\frac{D_h}{L}\text{Re}_l\,\text{Pr}\right]^{\frac{2}{3}}}\right)\frac{k_l}{D_h}$$	18998.88	18999	W m^{-2} K^{-1}
$ht_{conv,v}$	$$\left(3.66+\frac{0.668\frac{D_h}{L}\text{Re}_v\,\text{Pr}}{1+0.04\left[\frac{D_h}{L}\text{Re}_v\,\text{Pr}\right]^{\frac{2}{3}}}\right)\frac{k_l}{D_h}$$	2684.91	2685	W m^{-2} K^{-1}
$ht_{conv,tp}$	$ht_{conv,l}(1-x)+ht_{conv,v}x$	16731.35	16731	W m^{-2} K^{-1}
ht_{tp}	$ht_{NB}S+ht_{conv,tp}F$	27058.7	27058	W m^{-2} K^{-1}

Table B-2. Agostini and Bontemps correlation hand calculations

Agostini and Bontemps					
Parameter	**Equation**	**ATTMO Value**	**Hand Calculation Value**	**Units**
Inputs	$q''= 110900$ W m^{-2} $x= 0.139$ $G=972.2$ kg m^{-2} s^{-1}			
ht_{tp}	$28q''^{\frac{2}{3}} G^{-0.26} x^{-0.1}$	13162.50	13163	W m^{-2} K^{-1}